The fate of compact quiescent galaxies

博士論文

The fate of compact quiescent galaxies
（非星形成高密度銀河の運命）

森下貴弘

平成 29 年

PhD thesis

THE FATE OF COMPACT QUIESCENT GALAXIES

A DISSERTATION SUBMITTED TO
TOHOKU UNIVERSITY
IN PARTIAL FULFILLMENT OF REQUIREMENTS FOR THE DEGREE OF
DOCTOR OF PHILOSOPHY (SCIENCE)

BY
TAKAHIRO MORISHITA

ASTRONOMICAL INSTITUTE,
GRADUATE SCHOOL OF SCIENCE,
TOHOKU UNIVERSITY

JUNE 2017

"Knock 'em dead kiddo! Then drink."

– Louis E. Abramson

ABSTRACT

Observations of high redshift (high-z) galaxies have provided tons of new knowledge about galaxies in the past. By connecting the observational properties of galaxies at different redshifts, astronomers have obtained insight into their formation and evolution. In this thesis, I study evolutionary paths that massive galaxies can take over the last $\sim 12\,$Gyr, having a particular interest in compact galaxies recently found at $z > 1$. The thesis consists of two discussions. In the first part, I study observational properties of high-z galaxies to obtain a global view of their evolution. While these high-z galaxies are faint, and thus observationally challenging, I carefully treat the observational data, assess errors, and derive their properties, such as structural parameters, stellar mass, and colors. The snapshots of galaxies at different epochs are then connected each other, under a physically motivated assumption, to see the evolutionary picture to local galaxies. I obtain the "two-phase evolution scenario", where massive galaxies form bulge in early epoch ($z \sim 2$; as observed as compact galaxies) and in the later epoch they acquire more than half of their final mass through accretions of small satellite galaxies, to have comparable properties as local early-type galaxies (such as size, mass, and color). The obtained global picture, however, still has intrinsic scatters in the consisting galaxy properties. As such, in the second part of this thesis I shift my focus on interpreting the observed evolution, by studying smaller number of galaxies but with more observationally qualified data sets. With more detailed structural properties (i.e. Bulge-to-total ratio), and by looking into their surrounding environments for < 100 galaxies, I quantitatively investigate the possible evolutionary paths of galaxies with massive bulges, as relics of compact galaxies. Their evolution paths are divergent and therefore I conclude that the fate of compact galaxies cannot only be typical local elliptical galaxies by following the two-phase scenario, but also other types of galaxies (S0/later types) through different paths, such as wet mergers. To further constrain the evolution path, much more detailed measurements (e.g., age and metallicity at sub-galactic scale) would be necessary. At the end of this thesis, I summarize these findings and provide some prospects for future observations.

TABLE OF CONTENTS

LIST OF FIGURES

LIST OF TABLES

ACKNOWLEDGMENTS

I am grateful to Professor Takashi Ichikawa, my supervisor, for dedicating his precious time and guiding me to be a professional scientist for more than five years. His attitude toward science really inspired and encouraged me to know more and more about the universe. I am also grateful to professional scientists and staffs at the astronomical institute of Tohoku university. Their broad and deep knowledge, unique personalities, and plentiful kindness made my life at the institution more meaningful and joyful.

A very special gratitude goes out to Professor Tommaso Treu for his generous hospitality and insightful supervision at the University of California Los Angeles (UCLA) for two years. Another special gratitude is given to Dr. Louis Evan Abramson, one of the greatest advisors in my life and, the most important friends, for his insightful/thoughtful guidance for both of science and non academic life during the time in Los Angeles. A lot of experience at UCLA, with very smart and kind colleagues, is already one of the most important parts of my whole life.

Although apart from academia, I would really appreciate my friends in the Tohoku Bluegrass community. I spent with you for more than 9 years from my entering the Tohoku university, and has been always amazed me by your talented musical ability and personality. You are truly talented entertainers, friends, and family in Sendai.

And finally, but by no means least, I would give the best thanks to my parents and family members, for their thoughtful and countless support. You are the model, who are teaching me how to enjoy one's life, and how to care about others. From the bottom of my heart, I would like to thank you for being my family.

Takahiro Morishita
Tohoku University

CHAPTER 1
INTRODUCTION

1.1 Background

Galaxies are complex systems, consisting of gas, stars, and dark matter. Inside the systems, a variety of physical phenomena are occurring — formation of stars from gas, interactions between baryon components, feedback from stars and active galactic nuclei. Interactions between other systems, such as galaxy-galaxy merger, close encounter, and/or ram pressure in dense regions of clusters of galaxies, also affect the whole system to change its properties, for example star formation activity, morphology, and kinematical state. Through experiencing these phenomena internally and externally, galaxies end up exhibiting universal relations among their observed parameters, as we see in the local universe, such as luminosity-velocity dispersion [Faber and Jackson, 1976], Fundamental Plane [Djorgovski and Davis, 1987, Dressler et al., 1987], black hole mass-bulge mass relation [Magorrian et al., 1998], luminosity-color relation [Strateva et al., 2001, Hogg et al., 2003], stellar size-stellar mass relation [Shen et al., 2003, Guo et al., 2009], stellar mass-metallicity [Tremonti et al., 2004, Mannucci et al., 2010].

To disentangle such tight relations, it is required to understand galaxy evolution in more detailed scale. Astronomers have made huge effort to study galaxies in a wide range of redshift and scale by observing, e.g., the Galactic stars, local group/nearby galaxies, and high-redshift (high-z) galaxies.

Among them, high-z galaxies are ideal targets to study galaxies in the past when they are just forming and starting their evolution. Observations of $z \sim 2$ massive ($\log M_*/M_\odot \sim 11$) galaxies, the main interest in this thesis, have been shed light by significant advances in instrumentations in the last two decades. Some of observational properties of such high-z galaxies have been found to significantly differ from those in the local universe. Directly observing galaxies at an early stage of evolution has provided us an advantage to study their evolution, because these systems had not been involved in phenomena which would consequently happen in the following $\sim 10\,\mathrm{Gyr}$.

Historically, massive galaxies are thought to form in an early-time rapid collapse, a.k.a. monolithic collapse [Eggen et al., 1962, Larson, 1975], based on observed color and three dimensional motion of the galactic stars — Eggen et al. [1962] found that metal poor stars, which are though to form from pristine gas, move randomly in elliptical orbits, while metal rich newly formed stars are rather found in an ordered circular orbit. In this scenario, the central stellar components are formed at the same time as the whole system is virialized.

Another interpretation of galaxies formation showed up later — the major merger scenario[1], where early-type galaxies are formed from equal mass galaxy-galaxy merging [Toomre, 1977, Barnes, 1988]. In this scenario, early-type galaxies are thought to form through merging spiral galaxies consisting of both stars and gas. As galaxies collide, gas dissipation triggers intensive

1. Although this often is called "merger scenario", I call major merger scenario to make it apart from minor merger scenario.

star formation in the center of the new system. Dissipation helps the orbiting stars to lose angular momentum, ending up to have a system of early-type morphology. This scenario is also known to reproduce observed properties, such as high velocity dispersion, $\sigma \sim 400\,\mathrm{km\,s^{-1}}$ [e.g., Kormendy and Illingworth, 1983].

However, neither of these scenarios successfully explain newly observed evidences both at low- and high-z universe. One example is that the observed stellar density of the local ellipticals suggest their formation redshift would be $z > 20$ in the monolithic collapse scenario, while we know from the studies of stellar population [Thomas et al., 2005] and the cosmic star formation history [Madau and Dickinson, 2014] that massive galaxies barely exist at $z > 6$. The merger scenario also ends up with too steep inner stellar profile in the remnant galaxies (cusp), while observed giant elliptical galaxies show less cuspy profile [Ferrarese et al., 1994, Rest et al., 2001].

A new evidence that disfavors these scenarios is the discovery of "compact passive galaxies" at high-z galaxies. Compact passive galaxies are characterized to be massive as local ellipticals (stellar mass, $\log M_*/M_\odot \sim 11$) but have very small sizes (effective radius, $r_e \sim 1\,\mathrm{kpc}$), populated at $z > 1.5$ [e.g., Daddi et al., 2005, Trujillo et al., 2007, Damjanov et al., 2009, Onodera et al., 2012], and has very high stellar velocity dispersion [$\sim 300\,\mathrm{kms^{-1}}$; e.g., Kriek et al., 2009, van Dokkum et al., 2009, van de Sande et al., 2013, Belli et al., 2014]. In monolithic collapse scenario, the size of galaxies is expected to keep as these galaxies formed, while this newly found population suggests significant size growth by a factor of $\sim$ 3-5 to the local ellipticals [Shen et al., 2003, Guo et al., 2009]. The small size galaxies are also found to be already passively evolving (i.e. no star formation), while the major merger scenario expects progenitors as star forming galaxies.

These galaxies are dominant population ($> 50\%$) among all passive galaxies at $z > 1.5$ [van Dokkum et al., 2015]. The number density of this population is high at $z > 1.5$ [$> 1 \times 10^{-4}\,\mathrm{Mpc^{-3}}$; van Dokkum et al., 2015] but thereafter becomes significantly lower [$\sim 5 \times 10^{-6}\,\mathrm{Mpc^{-3}}$ at $z \sim 0$; Valentinuzzi et al., 2010].

These facts suggest that compact galaxies would evolve to larger size quiescent population, such as elliptical galaxies and brightest cluster galaxies (BCGs) in the local universe. A question is then, **"how to evolve their sizes by a factor of ~ 5?"**

One of the favorable scenarios for this population is so-called "two-phase scenario" [e.g., Naab et al., 2007, Hopkins et al., 2009a, Johansson et al., 2009, Oser et al., 2010]. This is a scenario which effectively combines the collapse and hierarchical merger (but for this time dissipation-less, or "dry") scenarios — in the early phase at $z \gtrsim 2$ central massive cores of massive galaxies are formed through rapid and significant star formation, followed by a number of dry minor merger[2] to form outer envelope of the cores [e.g., Hopkins et al., 2009a]. One of virtues of this scenario is that it can effectively increase galaxy sizes, without triggering further star formation in passively evolving cores ("inside-out" scheme), which is consistent with previous findings that massive galaxies have experienced no star formation since $z \sim 2$ [e.g., Treu et al., 2005, see also Chapter 5]. However, this scenario is still unclear in a quantitative aspect — how many massive galaxies in the local universe have been through this scenario?

2. Minor merger is typically defined as merging between galaxies with mass ration of $< 1/3$.

One counter argument to the two-phase scenario is that observed compact galaxies are not true progenitors of local massive galaxies — there is another possibility to explain the significant size growth by newly quenched star forming galaxies, which typically have larger sizes [Shen et al., 2003, van der Wel et al., 2014] at later epochs at, e.g., $z < 1$, while passive compact galaxies would remain to be compact without significant structural growth [e.g., Poggianti et al., 2013], so called progenitor bias [e.g., van Dokkum and Franx, 1996, Carollo et al., 2013].

One way to investigate the scenario quantitatively is to study satellite galaxies around high-z massive galaxies [Mármol-Queraltó et al., 2012, Newman et al., 2012]. By counting satellite galaxies around massive compact galaxies at high-z, these authors made an expectation of the future growth by the accretion of satellite galaxies to central galaxies. Although there are several concerns with their method and data which is discussed in Chapter 4, they found that the number is not enough to fully explain the significant size growth of compact galaxies, which implies other mechanism(s) is needed, *or* the idea to grow their sizes is wrong [e.g., Carollo et al., 2013].

1.2 This thesis

As summarized above, compact galaxies are interesting targets to unveil the formation of local massive galaxies and physical phenomena in the early universe. To understand further, the following questions related to these galaxies are to be answered;

Q1. What types of galaxies would they become in the following ~ 10 Gyr?

Q2. What is the dominant mechanism to bring them to the local relations?

Q3. How did they accumulate mass in (only) few Gyr after the Big Bang, and stop star formation?

The first two questions are well studied in the last decade. In Chapters 2 and 3, I make some additional effort to synthesize these previous interpretations, by making use of newly obtained *HST* data. For a large number of sample galaxies over a wide redshift range, I carefully analyze their structural parameters (Chapter 2), and study progenitor galaxies at each redshift which are thought to evolve into massive galaxies in the local universe by reconstructing radial mass/color profiles (Chapter 3).

The third question has been pursued with much interest in succession of star formation, or "quenching." This is frequently argued for galaxies at higher redshift, the peak of the cosmic star formation activity [e.g., Madau and Dickinson, 2014], where many galaxies are forming stars at a significant rate, a factor of > 10 higher than equal-mass galaxies today [e.g., Elbaz et al., 2011, Wuyts et al., 2011, Whitaker et al., 2012, Kashino et al., 2013] and acquiring their structures [e.g., Bunker, 1999, Abraham and van den Bergh, 2001, Kajisawa and Yamada, 2001]. The concept of quenching is often discussed with transition of galaxy structure — completion of structural formation, for example bulge formation, is expected to cease the ongoing star formation from both observational [Franx et al., 2008, Bell et al., 2012, Genzel et al., 2014] and theoretical studies

Figure 1.1: Summary of sample galaxies in the thesis

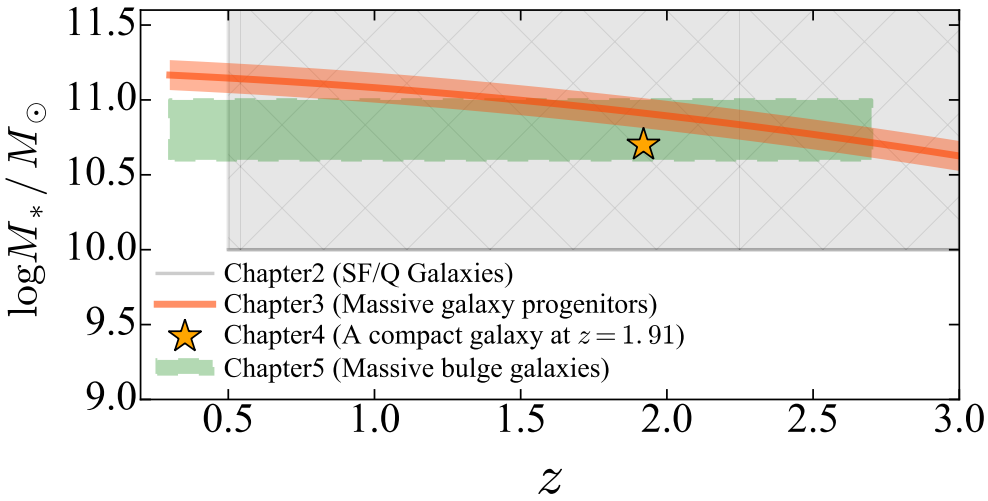

Summary plot of sample galaxies in this Thesis. In Chapter 2, I study all galaxies with $\log M_*/M_\odot > 10$ at $0.5 < z < 3.0$ by grouping galaxies into starforming (SF) and quiescent (Q) galaxies to infer their structural properties. In Chapter 3, I select galaxies at a constant cumulative number density ($n \sim 1.4 \times 10^{-4}\,\mathrm{Mpc}^{-3}$) to study the structural evolution of massive progenitor galaxies, which are expected to be $\log M_*/M_\odot \sim 11.2$ at $z \sim 0$. In Chapter 4, I focus on a compact galaxy and its satellite galaxies found at $z \sim 1.91$, to consider the possible evolution paths, in the context of the two-phase evolution scenario. In Chapter 5, I study galaxies with massive bulges ($10.6 < \log M_{*,\mathrm{bulge}}/M_\odot < 11$), as relics of compact galaxies, to see if the two-phase scenario is the most favorable one for compact galaxies at $z \sim 2$.

[Martig et al., 2009], because the gravitational potential become deep and the system would be more stabilized, preventing further instability i.e. star formation. I pursue this question by studying structural parameters obtained for galaxies at $z < 3$, and the relation between bulge formation and galaxy star formation activity (Chapter 3). The derived evolutionary scenario, two-phase scenario, is then studied in Chapters 4 and 5, to quantitatively estimate its impact on galaxy evolution.

Although it is beyond the present study, the third question has also been pursued in conjunction with higher redshift star forming progenitors, such as sub-millimeter (submm) galaxies and quasars [e.g., Toft et al., 2014]. The direct comparison with higher redshift progenitors is still observationally difficult, but rather need the next generation instruments such as *JWST*, though a number of works have studied the starforming counterparts at the similar redshift range of compact galaxies [Barro et al., 2014, 2015, van Dokkum et al., 2015]. The prospect for future studies will be discussed in Chapters 5 and 6.

The sample mass and redshift range of galaxies used in each Chapter is summarized in Figure 1.1. Throughout the thesis, I assume $\Omega_m = 0.3$, $\Omega_\Lambda = 0.7$ and $H_0 = 70\ \mathrm{kms}^{-1}\mathrm{Mpc}^{-1}$ for cosmological parameters. Magnitude is in AB magnitude system [Oke and Gunn, 1983, Fukugita et al., 1996].

CHAPTER 2
[PART 1] ON THE STRUCTURE OF HIGH REDSHIFT GALAXIES

Brief summary[1]

A number of high-z massive galaxies studies have started to witness their properties and insight into their formation and evolution to local universe galaxies. Since the cosmic star formation rate density is known to peak at $z \sim$ 1-2 [e.g., Dickinson et al., 2003, Heavens et al., 2004, Hopkins et al., 2006, Madau and Dickinson, 2014], galaxy structures and morphologies are also believed to change dramatically during the epoch.

Interestingly, a number of studies have found that high-z passively evolving galaxies are by a factor of $\sim$ 2-5 smaller than local galaxies at a given stellar mass [e.g., Daddi et al., 2005, Trujillo et al., 2007]. Considering that these galaxies have already stopped forming stars and acquired huge amount of stellar mass, these galaxies are believed to be the local early-type galaxies (ETGs), with radii of by a factor of $\sim$ 5 larger. To increase the size to the local ETGs, significant size evolution would be needed, while sizes of high-z galaxies also could be underestimated, because of low signal-to-noise ratio (S/N), in particular those taken through ground-based near-infrared imaging observations.

To conquer the concern, in this first chapter I analyze newly released *HST*/WFC3-IR images in the GOODS-N region to study structures of massive galaxies at $z > 1$. The newly obtained, space-based NIR imaging data, allow to study $z > 1$ galaxies, which was not accessible with enough sensitivity and spatial resolution from ground-based facilities in previous studies. Therefore, the main purpose of this chapter is to focus on measuring galaxy structure (especially at high-z) and to show how to conquer the related concerns. The detailed processes are summarized in Section 2.1, so that future studies can follow the same manner with updated data.

After examining the reliability by using mock galaxies, real data is then used — one-dimensional radial profiles (Sérsic profile) of 299 passively evolving and 1083 starforming galaxies at $z \sim$ 0.5-3.0 are obtained in Sections 2.2 and 2.3. I find that observed r_e and n of massive ($\log M_*/M_\odot \geq$ 10.5) passive galaxies increase by a factor of $\sim$ 2.2 from $z \sim$ 2.5 to $\sim$ 0.5, while weaker changes are observed in all star-forming and less massive passive galaxies, which is consistent with previous findings with smaller sample sizes. While previous studies only measured radii of galaxies and conclude the evolution scenario of passive galaxies, in this chapter I also study the evolution of Sérsic index, n, to obtain a further insight into the structural evolution of galaxies. Sérsic indices of massive QGs are found to significantly evolve as $n \propto (1+z)^{-\alpha_n}$ with $\alpha_n = 0.74 \pm 0.23$ ($n \sim 1$ at $z \sim 2.5$ to $n \sim 4$ at $z \sim 0.5$), while those of the other populations are found to barely change ($n \sim 1$) over the redshift range.

Although the intensive discussion is limited by roughly defined "massive" galaxies, by combining these observed evidence of size evolution, I discuss the possible evolutionary path of the passive galaxies in Section 2.4. Considering the fact that major merger is too rare to explain *all*

1. This study is based on Morishita et al. [2014].

massive galaxies found by numerical simulations, I suggest that gas-poor (dry) minor merger is the most favored scenario for them to be local massive galaxies. Further observational effort will be made in the following chapters, to discuss their evolutionary path to the local counterpart and to study the mechanism in detail.

2.1 Mock Analysis on Galaxy Structure

Galaxy structures in this study are measured based on 2D surface brightness profile of Sersic [1968], which is written as

$$I(r) = I_e \exp\left[-b(n)\left(\left(\frac{r}{r_e}\right)^{1/n} - 1\right)\right], \tag{2.1}$$

where n is Sérsic index, r_e effective radius and I_e surface brightness at r_e. $b(n)$ is defined as a function of n. I use `GALFIT` [Peng et al., 2002] to fit galaxies with Sérsic profile, which simultaneously takes care of the effect of PSF, background, and neighboring objects. `GALFIT` is a 2D surface brightness fitting code which calculates χ^2 for model galaxies and finds parameter sets with minimum χ^2. By providing appropriate information for image PSF and object coordinates, `GALFIT` is designed to take account for these observational concerns and return intrinsic structural properties of target galaxies. On the other hand, `GALFIT` can also return biased results when used without much care of, e.g., sky subtraction, initial guess, and error maps [Häußler et al., 2007]. To examine the fitting method in this study, as well as to see possible bias/uncertainties, I apply `GALFIT` to mock galaxies in Section 2.1.2. I use the newest version of `GALFIT` 3.0.5, which is improved in calculating weight images. The revision makes results more reliable for faint objects (Chien Y. Peng, private communication).

2.1.1 Input Parameters

To perform morphological fitting with `GALFIT`, it is required to provide an appropriate set of initial structural parameters. This would help `GALFIT` to find the best fitting parameters and save CPU cost. The procedures before running `GALFIT` is as follow. I first use `SExtractor` version 2.5.0 [Bertin and Arnouts, 1996] to estimate galaxy properties such as position, magnitude, radius, axis ratio, and position angle. Total magnitude, MAG_AUTO ($m_{\rm AUTO}$), and half-light radius, FLUX_RADIUS 50 (r_{50}), which encircles half the light emitted from galaxies, are set as an initial parameter for magnitude and effective radius, respectively.

An initial guess for n is not obtained by `SExtractor`. I therefore set the parameter to 0.5 to 8 by step of 0.5, and iterate `GALFIT` 16 times for each galaxy to see how much the results would change, as is employed by Bruce et al. [2012]. I found that the results are hardly affected, and decide to reduce the initial parameter sets to those with $n = 1, 2.5, 4$. After getting results from three different initial guesses, I adopt the best-fit parameter sets with minimum reduced chi square,

Table 2.1: Structural Parameters for Mock Galaxies

m	$r_{\rm e}$	n	q	PA
19–28	2–30	0.5–10	0.1–1.0	0–180

χ^2/ν, where ν is the number of degrees of freedom for fitting, while I discard the results with unrealistic parameters (see Section 2.1.2 for the details).

2.1.2 Mock Fitting Test

In this subsection, I scrutinize the reliability GALFIT with mock galaxies before applying to the real galaxies. Mocks are prepared by GALFIT with random sets of r_e, n, total magnitude (m), axis ratio q and position angle (PA) (see Table 2.1). Throughout this study, r_e is circularized as $r_e = a_e\sqrt{q}$, where a_e is the effective radius along the semi-major axis derived by GALFIT. The images are convolved with a Moffat-profile PSF of FWHM $\sim 0''.16$ and β = 2.5, as simulated to those found in the real WFC3 images. I note that fitting test on mock galaxies made by IRAF packages, gallist and mkobjects, with the same parameter sets returns almost identical results. The only difference in both mock galaxies are the ways to convolve PSFs.[2]

By following the procedure in Section 2.1.1, I first fit mock galaxies without noise. For this test, GALFIT precisely returns the original parameters. To test the realistic situation with noise, I bury the same mock galaxies in the WFC3 images at random positions. Although WFC3 images are sky-subtracted through the drizzle tasks, I repeat the sky subtraction at each position to remove the local sky evaluated with IRAF/*imstat*. In order for GALFIT to estimate the background, it is required to have postage stamps with enough empty space, compared to areas dominated by galaxies. For each galaxy I cut a square image from the mosaic image with a side of $r_{\rm fit}$ in pixel,

$$r_{\rm fit} = 2(3a \times r_{\rm Kron} + 20), \tag{2.2}$$

where a is the SExtractor output A_IMAGE and $r_{\rm Kron}$ is KRON_RADIUS. $r_{\rm fit}$ is large enough for applying GALFIT to the present samples ($r_{\rm fit} \leq 500$ pixels).

Neighboring galaxies also easily affects the results of target galaxies, as studied in Häußler et al. [2007], and therefore need to be treated appropriately. The neighboring objects around the target galaxies are masked out with SEGMENTATION_IMAGE obtained by SExtractor, while other studies [Häußler et al., 2007, 2013] fit all of them simultaneously. Although the latter method can treat very faint envelope of galaxies which is not detected by SExtractor, the computational costs would be huge. As I will see in the following, the former, with less computational cost, way

2. Further details are discussed at http://users.obs.carnegiescience.edu/peng/work/galfit/TFAQ.htmlhttp://users.obs.carnegiescience.edu/peng/work/galfit/TFAQ.html.

Figure 2.1: Distribution of mock galaxies

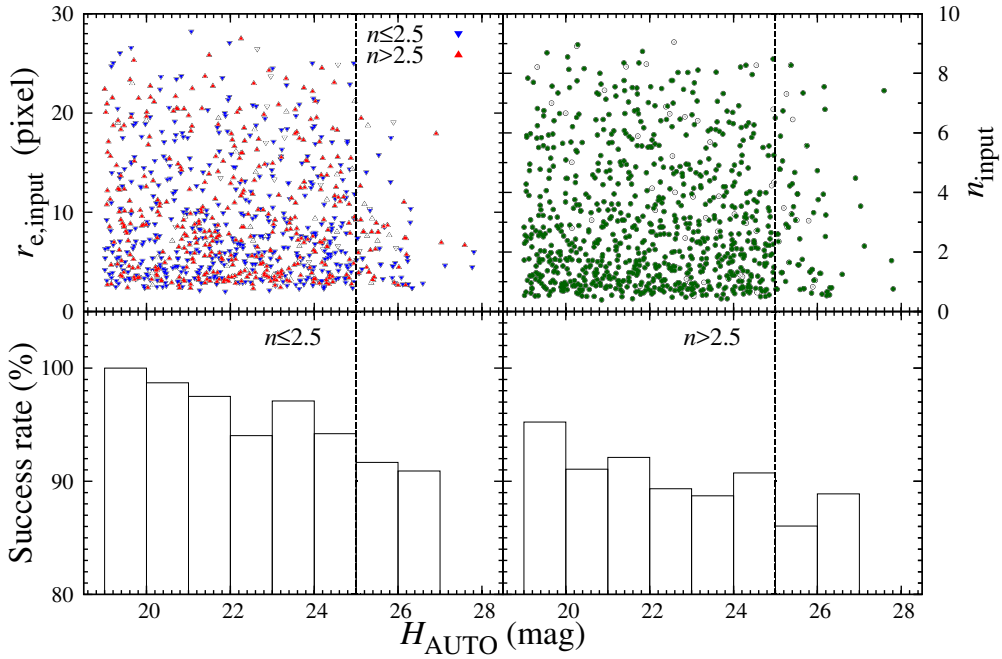

Top: Original distribution of mock galaxies in magnitude-radius (left) and magnitude-Sérsic index (right) spaces. *Bottom:* Success rate of galaxy structural fit, as defined in the main text, for $n < 2.5$ (left) and $n > 2.5$ (right) galaxies. The limiting magnitude is set at $H_{\rm AUTO} = 25$ mag, where the success rate decreases $\lesssim 90\%$.

works enough for our purpose.

The results that `GALFIT` does not converge during fit or with inconsistent magnitudes between `GALFIT` and `SExtractor`, $|\Delta m| \equiv |m_{\rm GALFIT} - m_{\rm AUTO}| > 1.0$, are discarded as failure. If neighboring objects are detected within 10 pixels from the target galaxy, I also discard the target from the final result. This is hardly thought to bias the results, because the close projection of galaxies happens randomly in the FoV. I refer to the rate of galaxies where `GALFIT` converges and with which fulfills the above criteria as success rate.

In Figure 2.1, I show the original distribution of mock galaxies in magnitude-radius-Sérsic index space. The success rate for the mock galaxies is shown as a function of galaxy magnitude in the bottom panel of Figure 2.1. Galaxies are grouped at $n = 2.5$, which is a frequently used indicator for disk ($n < 2.5$)/spheroidal ($n > 2.5$) galaxies. The success rate decreases from $> 95\%$ at $H_{AUTO} = 20$ mag to $\sim 90\%$ at 25 mag, where I cut the sample galaxies. At the same time, I find that galaxies with $n > 2.5$ have lower success rate than those with $n < 2.5$. This is also expected because galaxies with higher n have more extended profiles at the outer radius i.e. lower surface brightness and harder to find the best fit parameters.

In Figure 2.2, I show the differences of the result parameters and the original ones. The original parameters are appropriately reproduced up to $H_{\rm AUTO} \sim 25$ mag, while biases are observed there-

Figure 2.2: Mock results of GALFIT

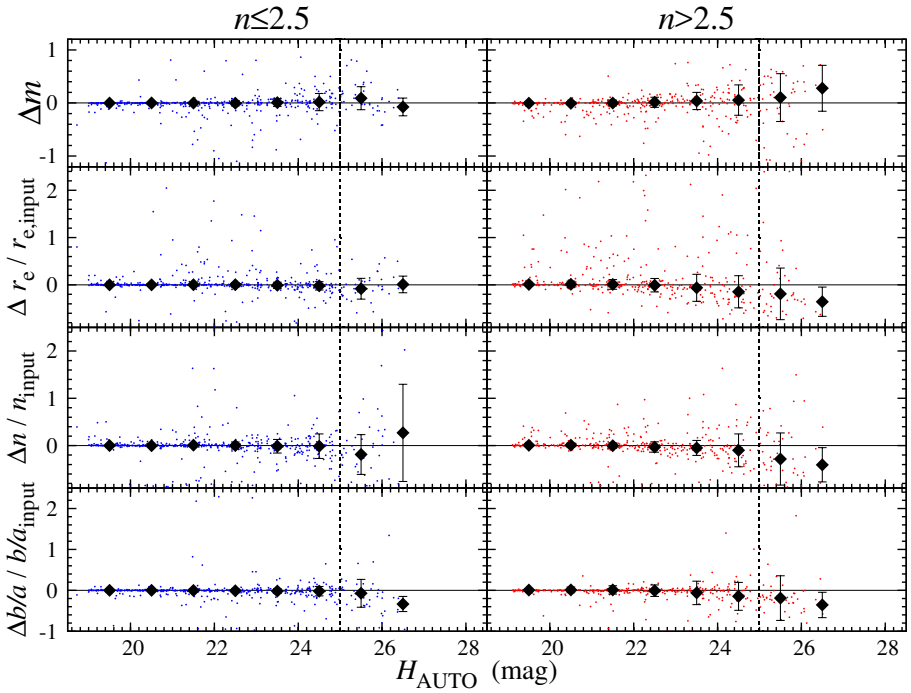

Results of GALFIT for mock galaxies buried in the WFC3 H160 images. The abscissa is the H-band MAG_AUTO ($H_{\rm AUTO}$) of SExtractor. The ordinates are differences between input and output parameters — $\Delta m = m_{\rm output} - m_{\rm input}$, $\Delta r_e/r_{\rm e,input} = (r_{\rm e,output} - r_{\rm e,input})/r_{\rm e,input}$, $\Delta n/n_{\rm input} = (n_{\rm output} - n_{\rm input})/n_{\rm input}$, and $\Delta(b/a)/(b/a)_{\rm input} = (b/a_{\rm output} - b/a_{\rm input})/(b/a)_{\rm input}$. The median values for each magnitude bin are depicted with filled circles with their median absolute dispersions (MADs).

after. I therefore set $H_{\rm AUTO} = 25$ mag as the limiting magnitude for the present analysis of real galaxies. It is noted that if mocks are buried in a clean postage stamp without any bright neighbors, rather than at random places, GALFIT returns higher success rates and less biased results even at fainter magnitudes [see Häußler et al., 2007, for the further detail].

2.2 Real Data

2.2.1 MODS Catalog

I select sample galaxies from the $K_{\rm S}$-band detected catalog of the MODS in the GOODS-N region [Kajisawa et al., 2009, 2011b]. MODS is based on the imaging observations of J-, H- and $K_{\rm S}$-bands with MOIRCS [Ichikawa et al., 2006, Suzuki et al., 2008], installed on the Subaru telescope, where limiting magnitudes are $Ks \sim 24.85$ mag and 25.85 mag for shallow and deep regions, respectively. The stellar mass (M_*) of MODS samples was estimated in Kajisawa et al. [2009] by SED fitting of multi-band photometry ($UBVizJHK_{\rm S}, 3.6\,\mu$m, $4.5\,\mu$m and $5.8\,\mu$m), with GALAXEV templates [Bruzual and Charlot, 2003], assuming Salpeter [1955] initial mass function (IMF), Calzetti et al. [2000] dust extinction law, and the solar metallicity. 2,093 of 9,937 galaxies have spectroscopic redshifts in the catalog, while the rest have photometric redshifts. The derived photometric redshift showed an excellent agreement with the spectroscopic redshift $\delta z/(1+z) = -0.011 \pm 0.078$ up to $z \sim 4$.

In the present study, I select galaxies brighter than the detection limit, $H_{160} = 25$ mag, which corresponds to $\log M_*/M_\odot \sim 10$ at $0.5 < z < 3.0$, much brighter than the detection limit of MODS catalog. The lower limit of redshift is set because of small survey volume. The selected sample galaxies are shown in Figure 2.3.

In MODS sample I also separate galaxies into two group, quiescent galaxies (QGs) and star-forming galaxies (SFGs), based on rest frame UVJ colors (see Section 2.3.4). Since the completeness for these two galaxy populations are different, I set different redshift limits; $\log M_*/M_\odot > 10$ for QGs (SFGs) at $0.5 \leq z \leq 1.5$ ($0.5 \leq z \leq 2.5$) and $\log M_*/M_\odot > 10.5$ at $1.5 \leq z \leq 2.5$ ($2.5 \leq z \leq 3.0$). The whole sample galaxies of QGs and SFGs are separately shown in Figure 2.2, where I see that over 90% of the MODS galaxies are included in the present sample.

2.2.2 HST/WFC3IR Imaging Data

To estimate the structural parameters of galaxies, I use the NIR data taken with *HST*/WFC3IR in the CANDELS survey [Grogin et al., 2011, Koekemoer et al., 2011]. The survey targeted in total $\sim 120\,{\rm arcmin}^2$ during ~ 170 orbits, giving imaging depth of $J_{125} \sim 25.9$ mag and $H_{160} \sim 26.1$ mag ($5\,\sigma$) in the GOODS-N region. I use the full data of the observations available in the Mikulski Archive for Space Telescopes (MAST). J_{125} and H_{160} correspond to the rest-frame V-band images at $z \sim$1.0–1.8 and 1.8–3.0, respectively. The images are reduced through PyRAF package [*DrizzlePac*; Gonzaga and Mack, 2011], where all standard calibrations, such as flat, sky background subtraction, distortion correction, cosmic ray rejection, are included. The images are

Figure 2.3: Redshift-stellar mass distribution of MODS galaxies

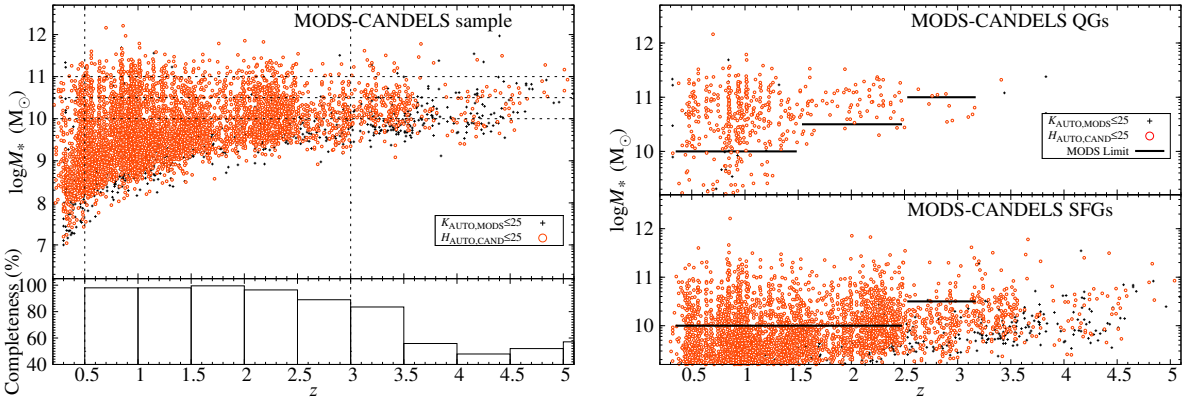

Left: Redshift-stellar mass diagram for the present sample with $H_{\rm AUTO} < 25$ mag (top). $H_{\rm AUTO}$ obtained by `SExtractor` in the WFC3/H_{160} image are depicted as red open circles. Black crosses represent MODS samples with $K_{\rm AUTO} < 25$ mag, which are not detected with $H_{\rm AUTO} < 25$. The vertical and the horizontal dashed lines show the redshift and stellar mass limits for the present study, respectively. The completeness for the present sample with $\log M_*/M_\odot > 10$ is also shown (bottom), where the ordinate represents the completeness in percentage of the galaxies with $H_{\rm AUTO} < 25$ mag to those with $K_{\rm AUTO} < 25$ mag and $\log M_*/M_\odot > 10$. *Right:* Redshift-stellar mass distribution of QGs (top) and SFGs (bottom) with $H_{\rm AUTO} < 25$ mag. The horizontal dashed lines show the stellar mass limits for each population at each redshift bin.

drizzled to a pixel size of $0''.06$ using pixel fraction value of 0.8 to be consistent with published GOODS-S images [Koekemoer et al., 2011]. The full width at half-maximums (FWHMs) of the PSF are $\sim 0''.15$ and $0''.18$ for J_{125} and H_{160} images, respectively. The FWHM of PSFs for H_{160} image is consistent with that of the GOODS-S images, though that of J_{125} is slightly larger. Since the PSF provided to `GALFIT` is one of the most important factors for the structural analysis, I investigate it carefully in Section 2.3.1.

2.3 Detailed Analyses of MODS Galaxies

2.3.1 Effect of Different PSFs

A PSF provided to `GALFIT` is one of the most influential parameters. Small changes in PSF profiles could lead to wrong estimates of structural parameters, and therefore an appropriate selection of PSF is required. In this subsection I show the results obtained with different PSFs, and conclude that the stacked stars would be more ideal than a simulated PSF for the purpose.

Conventionally, two types of PSFs are used — real star in the observed field and artificial star. Using real stars in the observed field would be ideal, because the observed condition is identical for objects in the same image. However, it is usually suffered from a fact that there is a small number of bright (but unsaturated) stars in an observed FoV, in particular for *HST*. Noise

and blending with other objects would affect the results as well. Artificial stars, which are made by simulating the observation, on the other hand, are free from such concerns. One example is TinyTim PSF, provided by Krist [1995]. The only concern of this is, that this is not a real star and cannot reproduce the observed PSF perfectly.

In Figure 2.4, I show the comparison of both PSFs. To reduce the noise, I stack unsaturated stars in the FoV to reproduce the intrinsic PSF — the sky background of each star is subtracted, and the flux is normalized before stacking. The stacked star has a FWHM $\sim 0''.18$, which is consistent with those in other fields of CANDELS [e.g., Skelton et al., 2014].

Tiny Tim PSF needs to be reduced in the same manner for the science images, since it is not designed for the drizzled image. By running the *HST* pipeline, I obtain the drizzled PSF, as done in previous studies [see also van der Wel et al., 2012]. The difference between original and drizzled TinyTim PSFs is clearly seen in the figure — drizzled one has a sharper inner profile, which is close to the observed real stars. In fact, the FWHM of the drizzled TinyTim PSF is $\sim 0''.18$, which is in good agreement with those of stacked stars. By comparing with real stars, I find that drizzled TinyTim PSF has 1. still sharper inner profile, and 2. a more extended wind at the outer radius. While the latter is caused by noise of real stars, the former is not straightforward, though it is beyonds the scope in this study, because this might be caused by a drizzle pipeline or TinyTim software. However, the difference caused by this would affect only faint objects ($m > 24$ mag), while my interest here is massive compact galaxies, which are typically bright even at $z \sim 2$ ($m \sim$ 22-24 mag). For more details, I refer the readers to Morishita et al. [2014].

Although I cannot conclude either of TinyTim and real PSF is better than the other, I adopt the median stacked stars (FWHM $\sim 0''.19$) for the following analysis, because this prove the self-consistency among results with different stars. It is noted that the variance of FWHMs of stars is independent of their position in the mosaic images. This is reasonable because the observation stacked images at different orbits with slightly shifted and rotated each other, which mimic the instrumental aberrations.

2.3.2 Galaxy Sizes at Different Rest Frame Colors

Throughout this chapter, I measure structural parameters of galaxies in F160W-band for all redshifts. However, the observed wavelength corresponds to different rest-frame wavelengths at different redshifts — $\lambda_{\rm RF} \sim 1\,\mu$m for galaxies at $z \sim 0.5$ and $\lambda_{\rm RF} \sim 0.5\,\mu$m at $z \sim 2.5$.

To examine the effect on r_e, I compare sizes of galaxies obtained in two different bands, J_{125} and H_{160}. I measure the size of 1646 MODS galaxies with $\log M_*/M_\odot > 10$ at $0.5 < z < 3.0$ in J_{125} and H_{160} bands in a same manner. The difference in r_e for 1071 galaxies is very small ($< 10\%$) for whole galaxy sample, except for small galaxies where PSF difference is thought to affect the size difference.

I also see differences in QGs and SFGs separately, because wavelength dependence of size depends on galaxy SEDs. It is reasonable that the difference is smaller for QGs compared to SFGs, since the former typically has a flat spectral feature while the latter can have strong emission lines in either band, which makes the size difference more significant. To minimized the wavelength

Figure 2.4: Radial profiles of PSFs

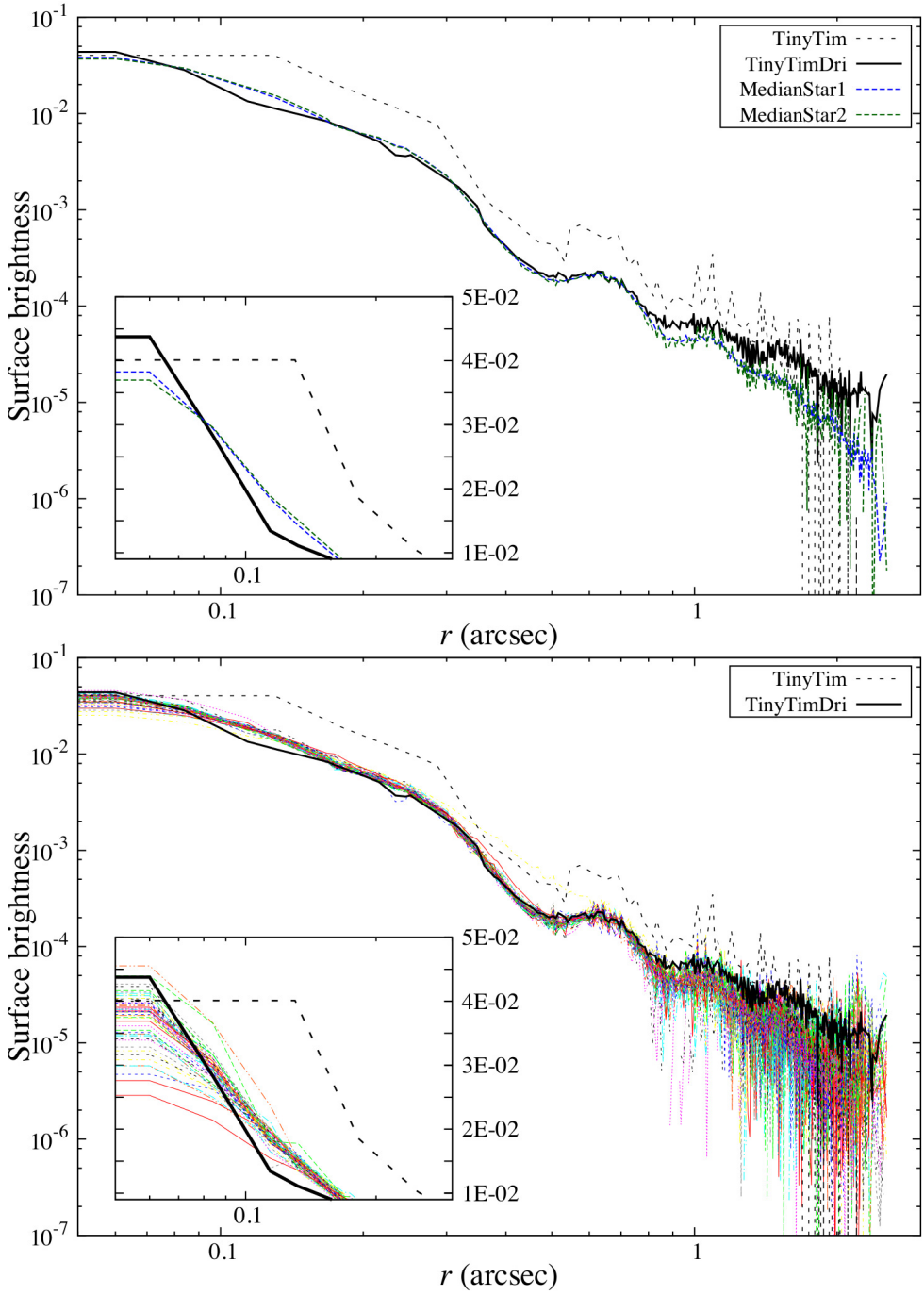

Top: radial profiles of four PSFs used in this study — original TinyTim (black dotted line), drizzled TinyTim (black solid line), and median stacked stars (blue and green dashed lines). The profiles are scaled so as to have same total magnitude. It is noted that the original TinyTim PSF is resampled into the same pixel scale as the other PSF. Inset shows the inner part of the profiles with linear ordinate scale. *Bottom:* Radial profiles of individual stars used for making median PSFs.

dependence of size, I need to take account of, for example, spatially resolved mass-to-light ratio, which beyonds the present study (see Chapter 3). Since mean difference is small and the focus in this study is more on QGs, in what follows I adopt the H_{160} image for all the sample galaxies.

2.3.3 Stellar Mass Correction

To fairly investigate a relation between galaxy stellar mass and size, I correct the stellar mass from MODS catalog, which is a non-parametric measurement, to be consistent with the measurement of r_e based on parametric fitting [see also Mosleh et al., 2013]. Stellar masses of the MODS galaxies were derived through non-parametric magnitude of $K_{\rm s}$-band image measured by `SExtractor` ($K_{\rm AUTO}$). The correction is made by following

$$M_*^{\rm cor} = 10^{-0.4(H_{\rm GALFIT}-H_{\rm AUTO})} M_*, \tag{2.3}$$

where $H_{\rm GALFIT}$ is the parametric magnitude obtained with `GALFIT`, and $H_{\rm AUTO}$ is derived by `SExtractor` for the H_{160} image. The correction is slightly larger for bright galaxies (< 21 mag), for which the non-parametric method miss a part of extended light ($\sim 10\%$). In the following sections I base on $M_*^{\rm cor}$, though the sample selection is made based on M_*.

2.3.4 Updating the UVJ Color Diagram

To group galaxies into QGs and SFGs, I follow the method in Williams et al. [2009], who used rest-frame $U-V$ and $V-J$ colors to select QGs;

$$\begin{aligned} U-V &> 0.88\times(V-J)+c \\ U-V &> 1.30 \\ V-J &< 1.60, \end{aligned} \tag{2.4}$$

where $U-V$ and $V-J$ in the rest frame were obtained with the SED-model fit to galaxies [Kajisawa et al., 2009]. The offset, c, is 0.59 and 0.49 for $0.5 < z < 1.0$ and $1.0 < z < 2.0$, respectively. For $z > 2.0$ galaxies, Williams et al. [2009] concluded that there was no visible two sequence and applied the offset for $1.0 < z < 2.0$.

To extend the criterion to higher redshift, I use specific star-formation rate (sSFR) in MODS catalog, which is estimated from UV and IR-luminosity by following Kennicutt [1998]. In Figure 2.5, I show histograms of both SFGs and QGs as a function of sSFR, where I see clear bimodality even at $z > 2.0$. I update the criteria for QGs at this redshift range so that the overlap of two population on $sSFR$ would become minimum by

$$\begin{aligned} U-V &> 0.88\times(V-J)+0.54 \\ U-V &> 1.35 \\ V-J &< 1.50. \end{aligned} \tag{2.5}$$

Figure 2.5: UVJ-diagram of MODS galaxies

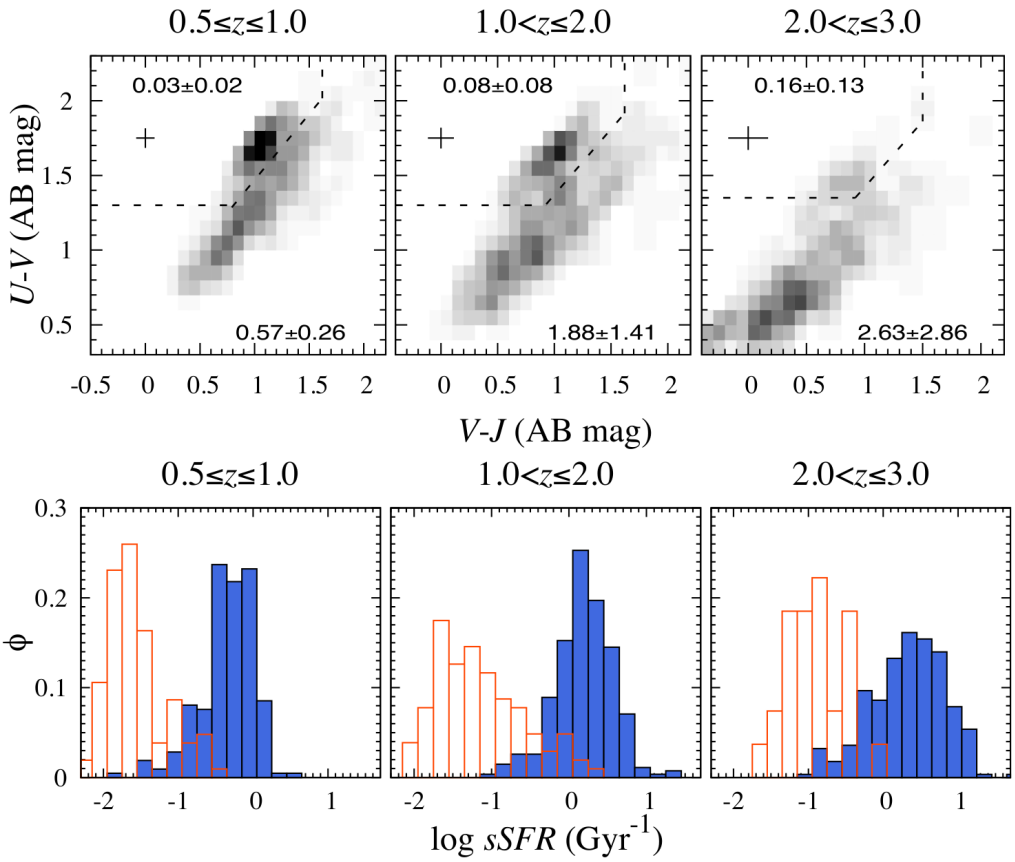

Top: color selections for QGs and SFGs in the UVJ diagram [Williams et al., 2009]. Cross symbol represents 1σ error in $U-V$ and $V-J$ for each redshift bin. Median sSFRs with MADs for QGs and SFGs are written at left top and right bottom, respectively, in each panel. *Bottom:* sSFR histograms of QGs (red open) and SFGs (blue filled). The ordinates for QGs and SFGs are normalized by the total number of each population in the redshift bins, respectively.

It is noted that the average values of sSFR raise as redshift increases [Daddi et al., 2007, Peng et al., 2010], and adopting fixed sSFR to select QGs is not appropriate.

2.4 Results and Discussion

Since the purpose of this Chapter is to show the reliability of derived structural measurements of high-z galaxies, I briefly show and discuss the results obtained for MODS galaxies. For the full discussion, I refer the readers to Chapter 3 and Morishita et al. [2014].

2.4.1 Stellar Mass-Size Relation for MODS Galaxies

From the original MODS galaxies, 1646 galaxies with $\log M_*/M_\odot > 10$ at $0.5 < z < 3.0$ are analyzed for structural parameters. From them, 1382 galaxies (with reliable structural parameters, without X-ray detection by Chandra Deep Field North survey Alexander et al. 2003) are selected. Based on the color selection in Section 2.3.4, 299 are classified as QGs and 1083 as SFGs. It is noted that 24 QGs detected at 24 μm by *Spitzer*/MIPS are transferred to SFGs, since these galaxies are thought to be heavily dust-obscured SFGs.

The size-stellar mass relations are plotted in Figure 2.6 for QGs and SFGs. It is seen that the sizes of QGs and massive SFGs at high redshift are smaller than those of the galaxies in the local universe [Shen et al., 2003, Guo et al., 2009] at a given mass. Massive galaxies ($\log M_*/M_\odot \sim 11$) with small radii ($r_e \sim 1$ kpc) are also found at $z > 1$ for QGs and at $z > 2$ for SFGs. Disappearance of small size SFGs at lower redshift ($1 < z < 2$) implies that these compact SFGs transfer to QGs [e.g., Barro et al., 2013].

To quantitatively estimate the relation, I fit with a following linear regression,

$$\log r_e = a_{\rm M} \log(M_*^{\rm cor}/M_c) + b_{\rm M}, \tag{2.6}$$

where $M_{\rm c}$ is a characteristic mass for massive galaxies, here set to $\log M_c/M_\odot = 10.5$. To see the dependence on the stellar mass, I divide the sample into massive and less massive groups. The best fit slopes, $a_{\rm M}$, and offsets, $b_{\rm M}$, at different redshifts are shown in Figure 2.7.

The slope, $a_{\rm M}$, of SFGs remains constant over the redshifts, ~ 0.15. For QGs, $a_{\rm M}$ rises slightly higher at $z < 1$, when the number of compact galaxies reduces and large size galaxies dominate at the same mass range.

The offset of slope, $b_{\rm M}$, shows clear difference between QG and SFG populations — while the offset for SFGs hardly changes over the redshift range ($\Delta b_{\rm M} < 0.2$), one for QGs increases significantly ($\Delta b_{\rm M} > 0.5$), which are equivalent to $\sim 60\%$ and $\sim 220\%$ increases in their sizes at a pivot point (M_c), respectively. This increase, i.e. size evolution, is investigated in the following section.

Figure 2.6: Size-mass distribution

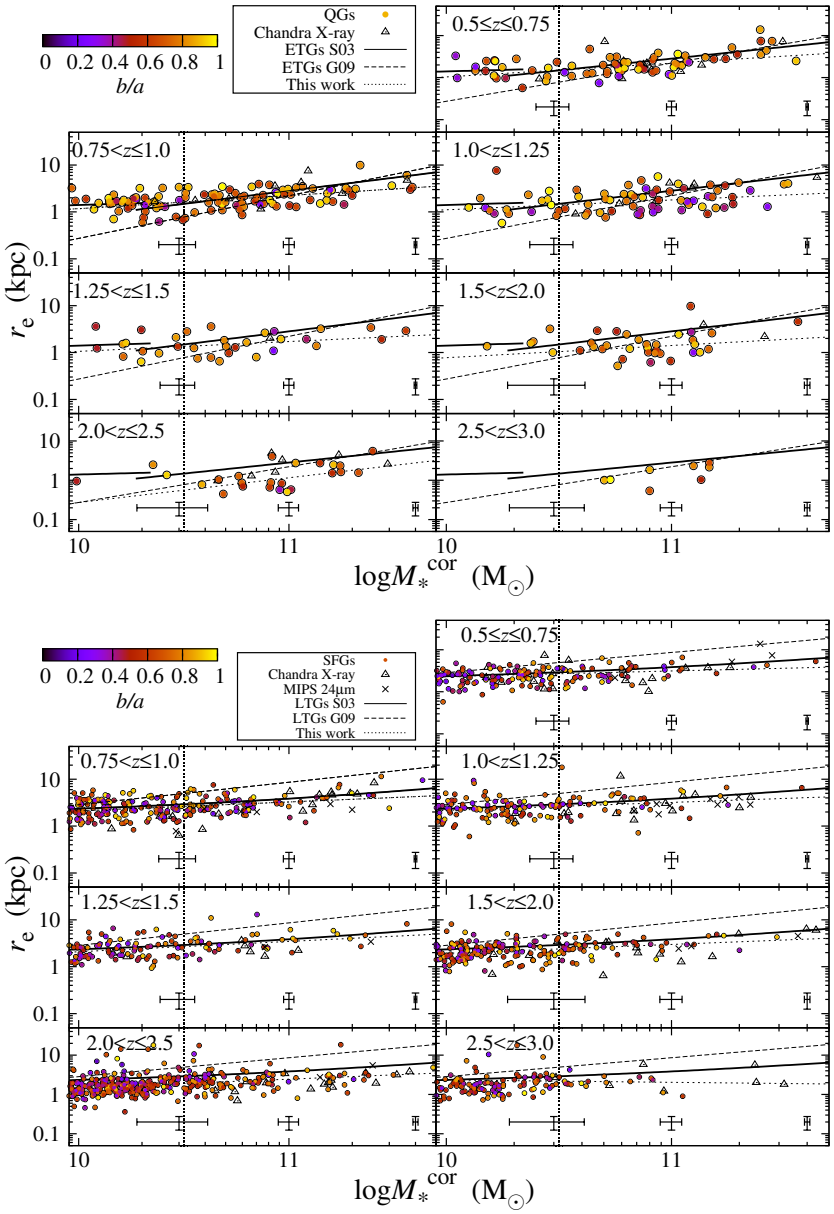

Top: size-stellar mass relations for effective radius, r_e, of QGs (filled circles), color-coded by observed b/a (q) value. The local size-stellar mass relations for early-type galaxies of S03 (solid line) and G09 (dashed line) are depicted. The relation for the present samples in each redshift bin is also shown (dotted line). X-ray detected sources by Chandra (open triangles) are not included in the fits. Error bars near the bottom of each redshift panel show typical errors of the stellar mass and r_e for each redshift bin. It is noted that the MAD for size represents the maximum error derived by GALFIT analysis with $n > 2.5$ at $24 < H_{\rm AUTO}/\,{\rm mag} < 25$ in Figure 2.2. The vertical dotted line for each redshift bin is the boundary of $\log M^{\rm cor}/M_\odot = 10.5$. *Bottom:* same as the left panel but for SFGs. QGs detected by Spitzer/MIPS 24 μm are represented by crosses. The local size-stellar mass relations for late-type galaxies of S03 (solid) and G09 (dashed) are depicted.

Figure 2.7: Best fit slopes and offsets

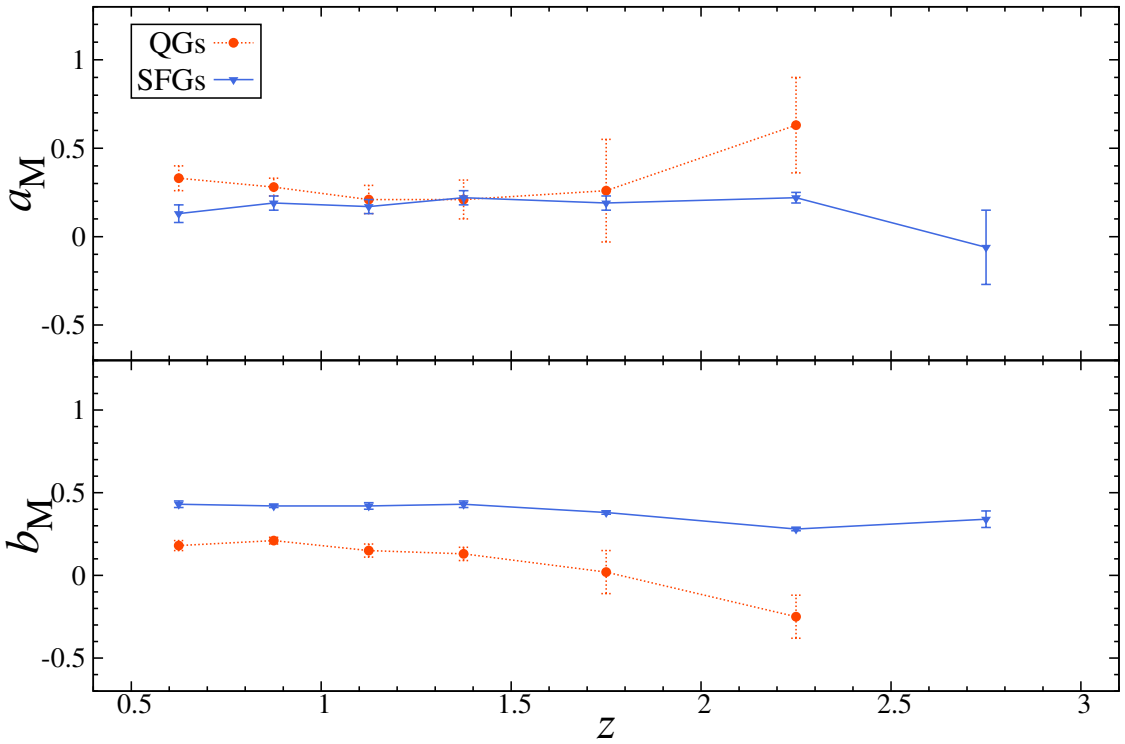

Best-fit slopes (a_M; top) and offsets (b_M; bottom) for the sizestellar mass relations as a function of redshift for QGs (red solid lines) and SFGs (blue dotted lines).

Figure 2.8: Redshift evolution of galaxy size

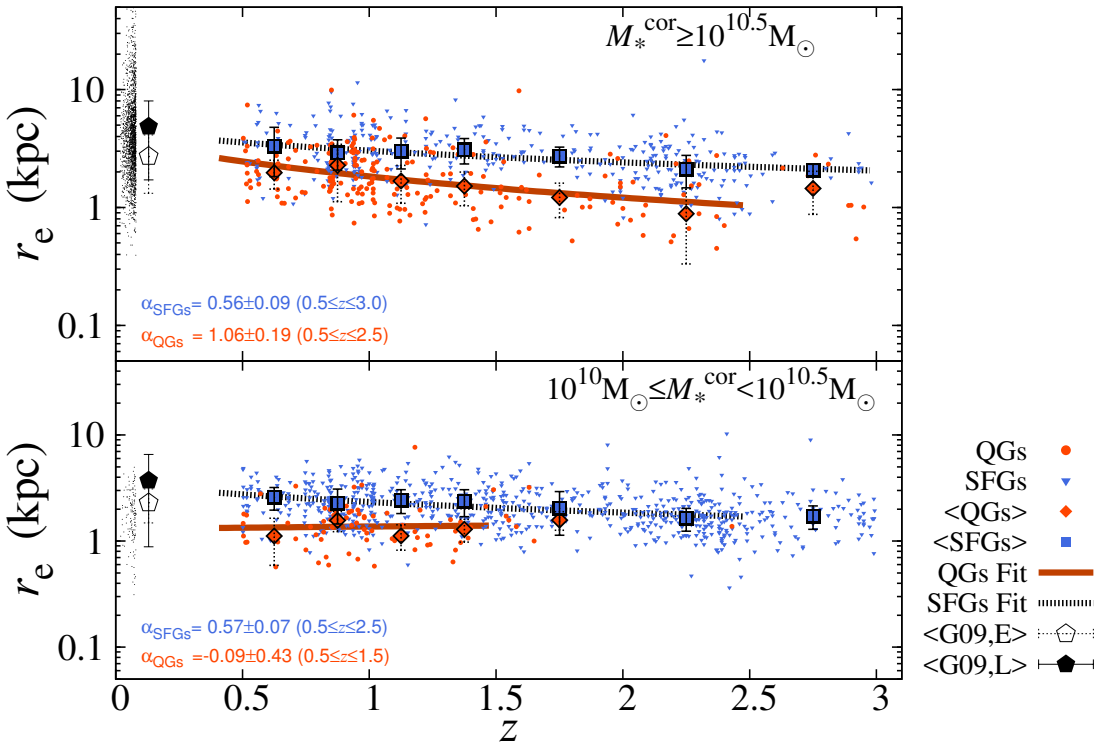

Evolution of r_e as a function of redshift for massive ($\log M_*/M_\odot > 10.5$; top) and less massive ($\log M_*/M_\odot < 10.5$; bottom) galaxies. QGs (red circles) and SFGs (blue triangles) are shown separately. The median sizes with MADs for QGs (red filled diamonds with dotted bars) and SFGs (blue filled squares with solid bars) are also shown. The local galaxies of CEN samples are also plotted (black dots) with the median sizes for early-type ($n > 2.5$, black filled pentagons) and late-type ($n < 2.5$, black open pentagons) galaxies. The thick solid lines and break lines represent the regression for QGs and SFGs, respectively. It is noted that the samples in the incomplete redshift bins are not included in the regression.

2.4.2 Evolution of Galaxy Size

I derive a regression for sizes of galaxies with $r_e \propto (1+z)^{-\alpha_{re}}$ to see their evolution as a function of redshift. To see in detail, I group galaxies into massive ($\log M_*/M_\odot > 10.5$) and less massive ($\log M_*/M_\odot < 10.5$) galaxies.

For massive QGs, I obtain $\alpha_{r_e} = 1.06 \pm 0.19$ at $0.5 \leq z \leq 2.5$, by a factor of ~ 2.5 increase, and for massive SFGs $\alpha_{r_e} = 0.56 \pm 0.09$, by a factor of ~ 1.7 increase at $0.5 \leq z \leq 3.0$. As is consistent with the estimate in Section 2.4.1, the significant size evolution is observed in QGs and mild for SFGs. In fact, the size evolution of SFGs follows the evolution of halo size as a function of redshift, $r_h(z) \propto H(z)^{-0.7}$, where $H(z)$ is the Hubble parameter at z. This implies that the size of SFGs, mostly dominated by late type galaxies, are scaled with the halo size. It is noted that SFGs show no mass dependence of the offset. In both mass bins, weaker evolution, $\alpha_{r_e} \sim 0.6$, is observed.

For less massive QGs, on the other hand, I obtain $\alpha_{r_e} = -0.09 \pm 0.43$ — the size hardly changes at $0.5 < z < 1.5$ within error, and the size increase is ~ 2. Although the number of galaxies is small and intensive study is not conduct here, it is possible that these less massive QGs are relatively younger than massive ones, and therefore some newly quenched SFGs, whose sizes are typically larger, are stochastically included at any redshift. The larger scatter from the best fit slope for this population (Figure 2.6) also supports this interpretation. For the intensive discussion about this, I refer the reader to Morishita et al. [2017], which extended the mass limit down to $\log M_*/M_\odot \sim 8$, and found that 1. low mass QGs are younger than more massive ones and 2. larger size QGs are younger than smaller ones.

2.4.3 Evolution of Sérsic Index

As well as galaxy size evolution, I study the evolution of Sérsic index over the observed redshift range. Sérsic index is an important structural parameter, because 1. this quantity is strongly correlated with r_e and can affect the size evolution, 2. this is a good indicator of the concentration of galaxy light, and 3. early- and late-type galaxies have distinct values [$n \sim 1$ for disk and $n \sim 4$ for ellipticals: e.g., Shen et al., 2003].

In Figure 2.9, I show the distribution of n for the present sample. SFGs have constant n (~ 1) over the redshifts, irrespective of their stellar masses, while QGs have typically larger values and mass dependence. Interestingly, the mass dependence of n for QGs, and its redshift evolution (i.e. significant evolution in n of massive QGs but no evolution in less massive ones), is observed, as has been in their sizes as well.

The regression of n is obtained with $n \propto (1+z)^{-\alpha_n}$, and shown in Figure 2.10. n for SFGs shows no redshift evolution ($\alpha_n \sim 0.04$–0.1) over $z \sim 0.5$-2.5, while that of massive QGs significantly increases ($\alpha_n \sim 0.74$). This implies that massive QGs are more likely to be disky profiles, rather than highly concentrated de Vaucouleurs' profile observed in the local universe. van der Wel et al. [2012] found that the average axis ratio is smaller at higher redshift, which is another strong evidence that the population was more disky profile at high-z.

Figure 2.9: Distribution of Sérsic index

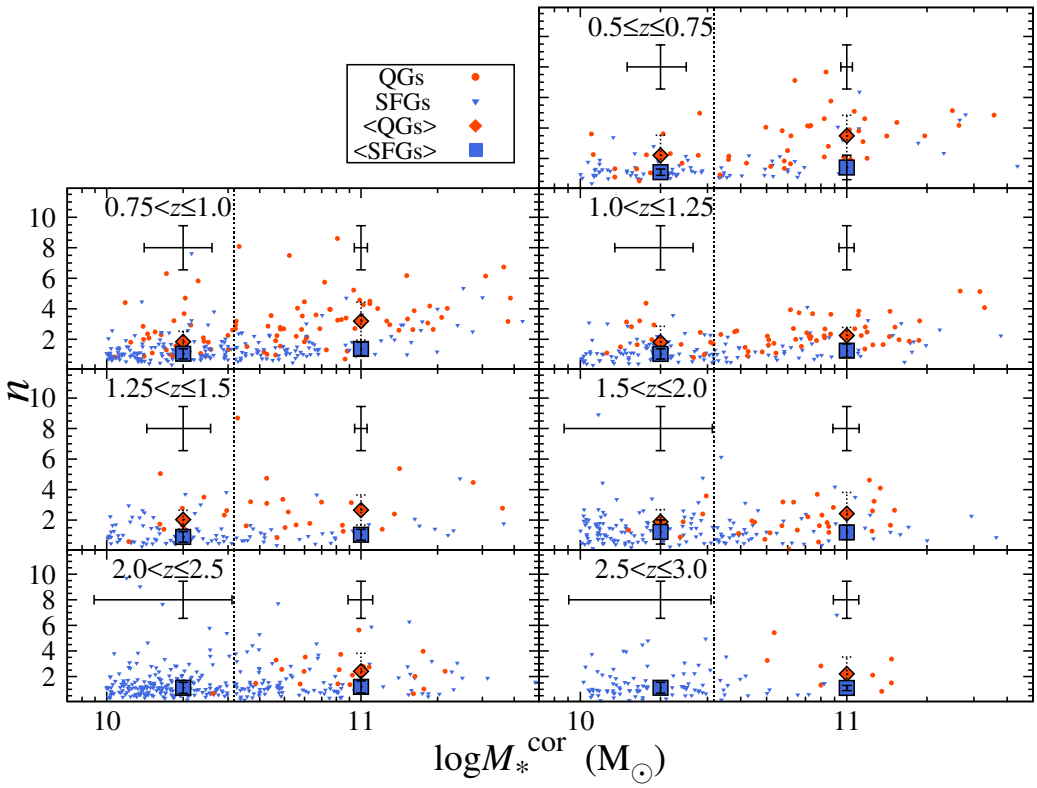

Distribution of Sérsic index, n, with stellar mass for the QGs (red filled circles) and SFGs (blue filled triangles). The median values with MADs in each redshift bin are shown for QGs (red filled diamonds with dotted lines) and SFGs (blue filled squares with solid lines) with $\log M^{\rm cor} > 10.5$ and $\log M^{\rm cor} < 10.5$, respectively. The vertical dotted line for each redshift bin is the boundary of $\log M^{\rm cor} = 10.5$.

Figure 2.10: Redshift evolution of Sérsic index

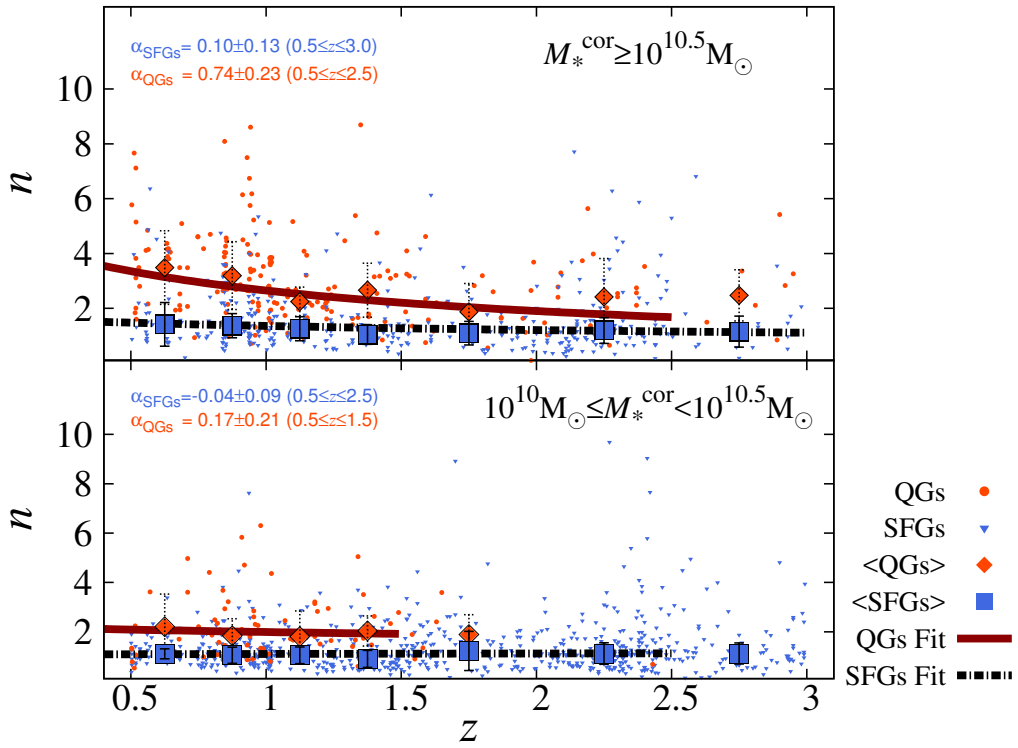

Same as Figure 2.8, but for n. While redshift evolution in n is observed for massive quiescent galaxies ($\alpha_{\rm QGs} = 0.74$), much weaker or no evolution are observed for other groups.

In the minor merger scenario of massive early type galaxies (which is discussed in the following chapters), galaxies acquire stellar mass at the outer part by stellar accretion for $\sim 70\%$ of their final mass. These newly obtained stellar envelope would grow a galaxy profile from low-n to high-n [see Figure 4 in Naab et al., 2009, for example].

2.4.4 Evolution of Galaxy Structure

With a careful test of `GALFIT` analysis, I obtained reliable structural parameters for the MODS samples. By dividing the sample into 4 group (massive/less-massive, SFG/QG) and observing their redshift transition, I discuss the transition of galaxy structures.

The size of massive QGs is represented as $r_e \propto (1+z)^{-\alpha_{re}}$ with $\alpha_{r_e} \sim 1.06$ from $z \sim 2.5$ to ~ 0.5 (a factor of ~ 2.5 increase at a given stellar mass), while less massive QGs show weaker evolution. SFGs, on the other hand, have much weaker evolution ($\alpha_{r_e} \sim 0.5$), irrespective of their stellar mass bins, which implies a very simple/optimistic scenario where QGs are taken from SFGs at a same stellar mass (at any redshifts) does not explain the observed result.

The size evolution of quiescent population has been discussed theoretically [Fan et al., 2008, Hopkins et al., 2009b, Naab et al., 2009, Oser et al., 2012]. One powerful argument is the minor merger scenario, where satellite galaxies (much less massive than host galaxies) accrete to the outer part of host galaxies and efficiently increase their sizes. By assuming the virial theorem, Naab et al. [2009] shows $\sim 4 (\sim 2)$ minor merger events with 1:10 (3:10) mass ratio successfully reproduce the observed size evolution by a factor of ~ 3, while major merger is not efficient compared to this process (see Chapter 4).

This interpretation is also supported by the observed transition in Sérsic index. I found that n of massive QGs is similar to SFGs ($n \sim 1$) only at high redshift, but then becomes larger (~ 4) as redshift decrease. The accretion of satellite galaxies would make galaxy profiles to $n = 4$, as is numerically calculated by Naab et al. [2009].

For less massive QGs, the evolution scenario seems different. The redshift evolution of both r_e and n is much weaker than those of massive QGs, but rather similar to SFGs. This implies that these galaxies are taken from blue population with similar stellar mass, without significant structural evolution [see Morishita et al., 2017]. The observed mass dependence of QGs' evolution can be attributed to a fact that less massive galaxies tend to reside in less dense environment than massive ones and have less chances to have satellite galaxies.

One concern in the present study is that I did not take account of the mass evolution over the redshift range. To mitigate the concern, I show the normalized size of galaxies in Figure 2.11. The normalization of r_e is derived as $r_{\rm e,norm} = r_{\rm e}/(M_*^{\rm cor}/M_c)^{\alpha_{\rm M}}$, where $\alpha_{\rm M}$ is the linear slope of the size-stellar mass relation for each redshift bin (Section 2.4.1). I still see the size evolution with $\alpha_{r_e} = 1.07 \pm 0.15$ for QGs (and $\alpha_{r_e} = 0.59 \pm 0.05$ for SFGs), which is consistent with the results of previous analysis.

Figure 2.11: Mass-normalized size distribution

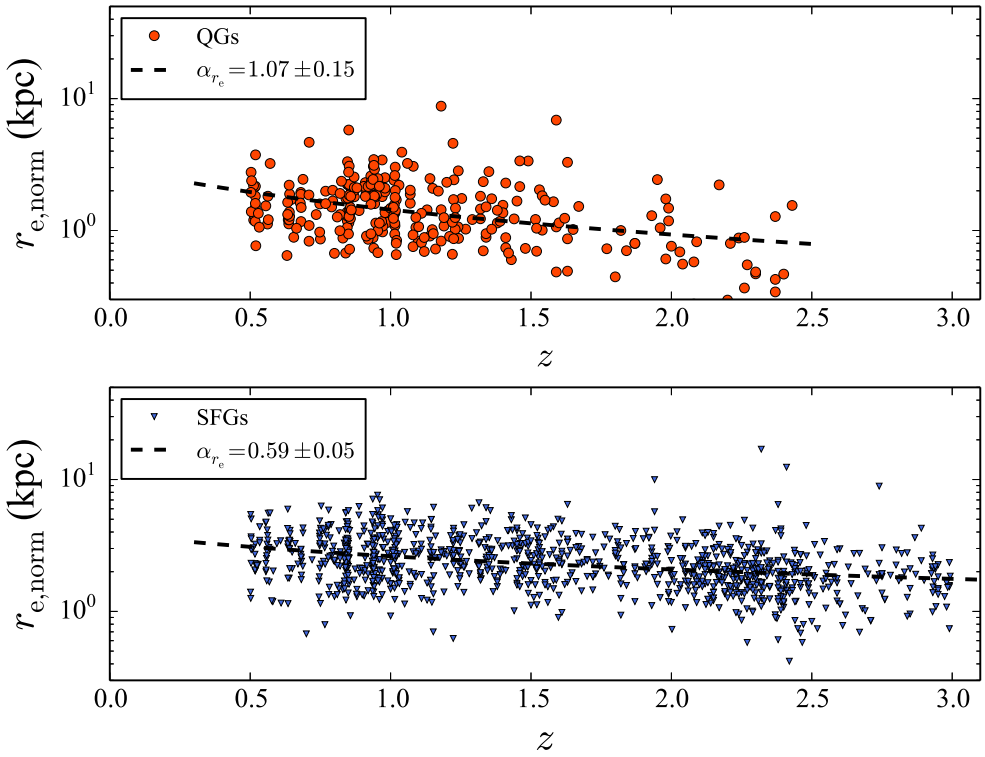

Mass-normalized size ($r_{\rm e,norm} = r_{\rm e}/(M_*^{\rm cor}/M_c)^{\alpha_{\rm M}}$) evolution for QGs (top) and SFGs (bottom). Black dotted lines represent the regressions of $r_{\rm e,norm} \propto (1+z)^{-\alpha_{re}}$.

Figure 2.12: Redshift evolution of structural parameters of five most massive galaxies

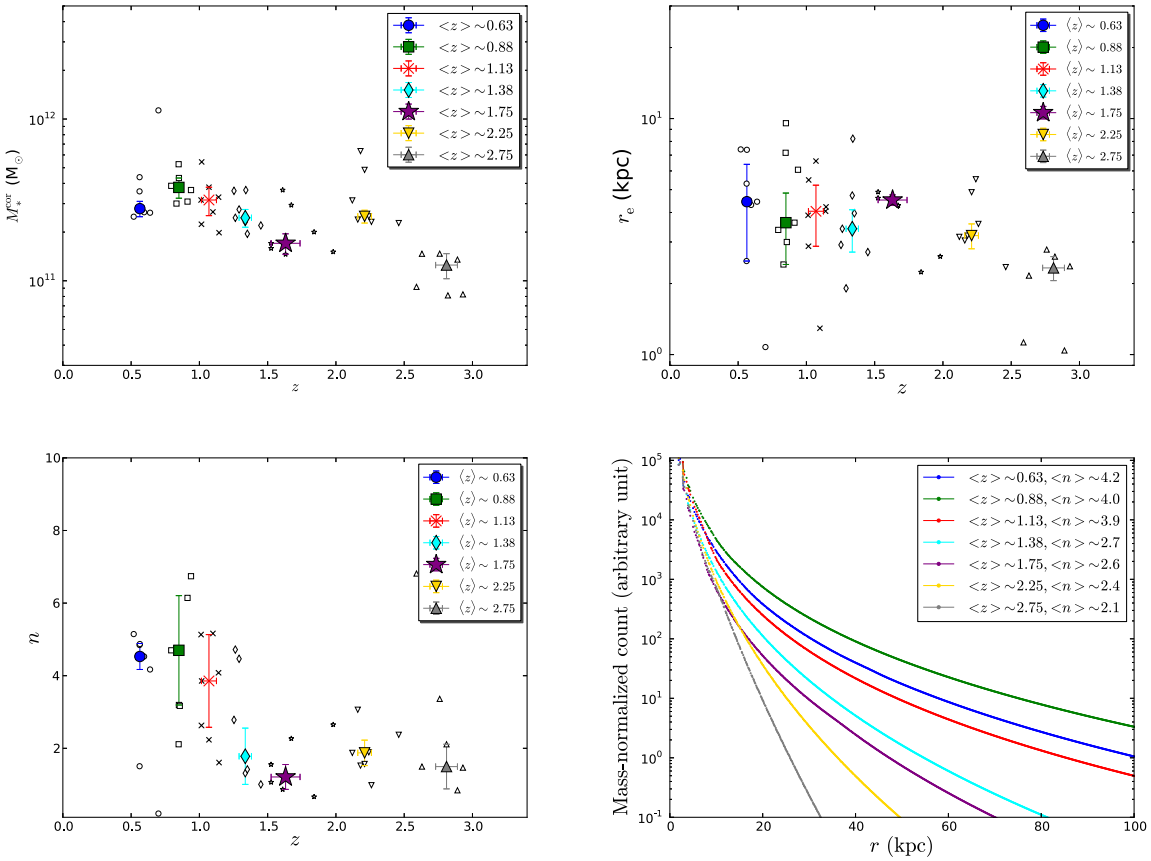

Redshift evolution of physical parameters of the seven most massive galaxies in each redshift bin studied in Section 2.4.5 — stellar mass (left top), r_e (right top), and m (left bottom). The best fit radial profiles for these galaxies are also shown (right bottom). As speculated by the evolution of r_e and n, the galaxy profile of these massive galaxies evolve inside-out way, where massive cores have already formed at $z > 2$ and most of stellar accumulation occurs at the outer radius thereafter.

2.4.5 Evolution of the Most Massive Galaxies

I also show the evolution stellar mass, radial profile, and structural parameters of the seven most massive QGs taken from each redshift bin in Figure 2.12. At a first order, the most massive galaxy at one epoch is supposed to be the most massive galaxy at the next epoch, except that a major merger event of two less massive galaxies would produce more massive galaxy [3]. The selected sample consists of both SFGs and QGs, which is reasonable for the galaxy evolution. The observed trend is almost same as for the massive QGs, though the evolution in size is slightly weak here. The radial profile shows the evolution in inside-out way, where massive cores have already formed at $z > 2$ and most of stellar accumulation occurs at the outer radius thereafter. To investigate the structural evolution consistently with their mass evolution, further detailed analyses will be conducted in Chapter 3.

3. The volume of each redshift bin should also be similar with each other, so that massive galaxies can be connected at over the wide redshift. The small survey volume prevents this, while more detailed analysis is conducted in Chapter 3.

CHAPTER 3
[PART 1] CONNECTING MASSIVE GALAXIES AT DIFFERENT REDSHIFTS

Brief summary[1]

In the previous chapter, I measured and summarized the observed structural properties of galaxies at $0.5 < z < 3.0$. Comparing high- and low-z galaxies, however, would only provide limited evolutionary pictures. To conquer the situation, our mission is to figure out a tag which is 1. universal for galaxies, 2. observable, and 3. physically reasonable to trace a population of galaxies with, so that their progenitor and descendant are correctly matched [Ichikawa et al., 2007, Conroy and Wechsler, 2009, Guo et al., 2010, Tojeiro and Percival, 2010, Behroozi et al., 2013]. These tags can be, for example, halo mass, stellar age, velocity dispersion, and chemical abundance, though these quantities are usually hard to obtain for a large number of galaxies.

In this chapter I base an analysis on a constant cumulative number density, where I rank galaxies by stellar mass in each redshift bin. Then I choose galaxies with a given stellar mass in each redshift bin whose number density is constant over the whole redshift range.

Stellar mass of galaxies is obtained much more easily for a large number of galaxies, compared to the other quantities, thanks to recent multi-band imaging deep surveys. By using the *HST*/WFC3 and ACS multi-band imaging data taken in CANDELS [Grogin et al., 2011, Koekemoer et al., 2011] and 3D-HST [van Dokkum et al., 2013a, Momcheva et al., 2016], I study structural properties of massive galaxy (MGs; $\sim$ Andromeda galaxy mass) and Milky Way-mass galaxies (MWs) at $0.5 < z < 3.0$. Selection of these progenitors are conducted by assuming that galaxies evolve at a constant cumulative number density.

Observed properties of MGs at $z \sim 2$ is, interestingly, similar to what we are seeing as compact galaxies at the redshift — massive stellar component ($\log M_*/M_\odot \sim 10.7$) has already formed in $r < 2.5\,\mathrm{kpc}$ and passively evolving. The population then obtains a stellar component at outer ($> 2.5\,\mathrm{kpc}$) radius, so-called inside-out way, as suggested in previous studies. This is in contrast what we see for MWs, where stellar mass growth happens at all the radii and the effective radius would only evolve by a factor of < 2 ("self-similar way").

Further investigation is compensated with the derived rest-frame colors, which supplement star formation properties and population age at each radial distance. The observed color gradient is qualitatively consistent with what have been found in the local early type population [e.g., Tamura and Ohta, 2003, 2004], as is expected by the two-phase scenario. A sudden reddening of bulge at $z \sim 1.6$ and $z \sim 2.4$ for MWs and MGs, respectively, suggests the formation of bulge and would give a clue to the different gas accretion histories and quenching for these different populations.

A new approach to evaluate the morphological diversity by using the average surface density profile and its dispersion is discussed in the last section. This "variety" of the radial mass profile of MGs peaks at higher redshift ($z > 2.8$), and then rapidly converges to lower values (more uniform

1. This study is based on Morishita et al. [2015].

shape) at $z < 1.5$, while that for MWs remains in the outer region over the observe redshift, implying stochastic star formation activity at the outer radii is undergoing. These observed transition of massive galaxy progenitors gives us a clue to the fate of compact galaxies observed at $z \sim 2$, which will be investigated in the following chapters.

This chapter is organized as follows. In Section 3.1 I describe the data and catalog, as well as the selection method for the progenitors. The details of the resolved SED fitting and relevant reduction methods are followed in Section 3.2. The results and discussion are given in Sections 3.3 and 3.4. The chapter is summarized in Section 3.5.

3.1 Data

3.1.1 Sample Selection from the 3D-HST Catalog

I take sample galaxies from the Cosmic Assembly Near-IR Deep Extragalactic Legacy Survey [CANDELS; Grogin et al., 2011, Koekemoer et al., 2011] and 3D-HST [van Dokkum et al., 2013a]. The surveys provide multi-band optical to near-infrared imaging data of 2-10 orbits per pointing with the *HST* for 5 well-known fields (GOODS-North and South, AEGIS, COSMOS and UDS; the total survey area reaches $\sim$900 arcmin^2). I make use of a publicly available galaxy catalog by 3D-HST team [v.4.1; Skelton et al., 2014]; the photometric redshift was obtained with EAZY code [Brammer et al., 2008], which showed good consistency with previously obtained spectroscopic redshifts, $\Delta z/(1+z) = 0.003-0.005$, for galaxies with $H \leq 23$. The stellar mass was obtained with FAST code [Kriek et al., 2009], assuming Chabrier [2003] IMF. The best-fit SED was obtained with the *HST* imaging data, Spitzer/IRAC mid-infrared data, and ground-based imaging data at the wavelengths from ultraviolet U-band to near-infrared K-band. The star formation rate (SFR) was derived from the rest-frame UV flux of the best-fit SED template and mid/far-infrared data by Spitzer/MIPS. In addition, for some regions, medium-band imaging data are available, which increases the reliability of SED fitting.

From the 3D-HST catalog, I select the sample based on the spectroscopic redshift if available and photometric redshift for others, and stellar mass (M_*). For reliable photometry, selection criteria are set with $star\_flag$=0 and $use\_phot = 1$, which limit the sample to the galaxies with $H \leq 25$ mag in F160W-band.

3.1.2 Selection of Massive Galaxy Progenitors

Many previous studies select galaxies at a given mass, and see the transition of derived average properties, such as size and colors. More realistic/appropriate evolutionary pictures of high-z galaxies is figured out by correctly matching their descendants. While there are a number of novel matching schemes to select progenitor galaxies [Ichikawa et al., 2007, Conroy and Wechsler, 2009, Guo et al., 2010, Tojeiro and Percival, 2010, Behroozi et al., 2013], one useful example is based on a constant cumulative number density, which ranks galaxies by *observable* quantities, such as

Figure 3.1: Massive galaxy and Milky Way mass progenitors

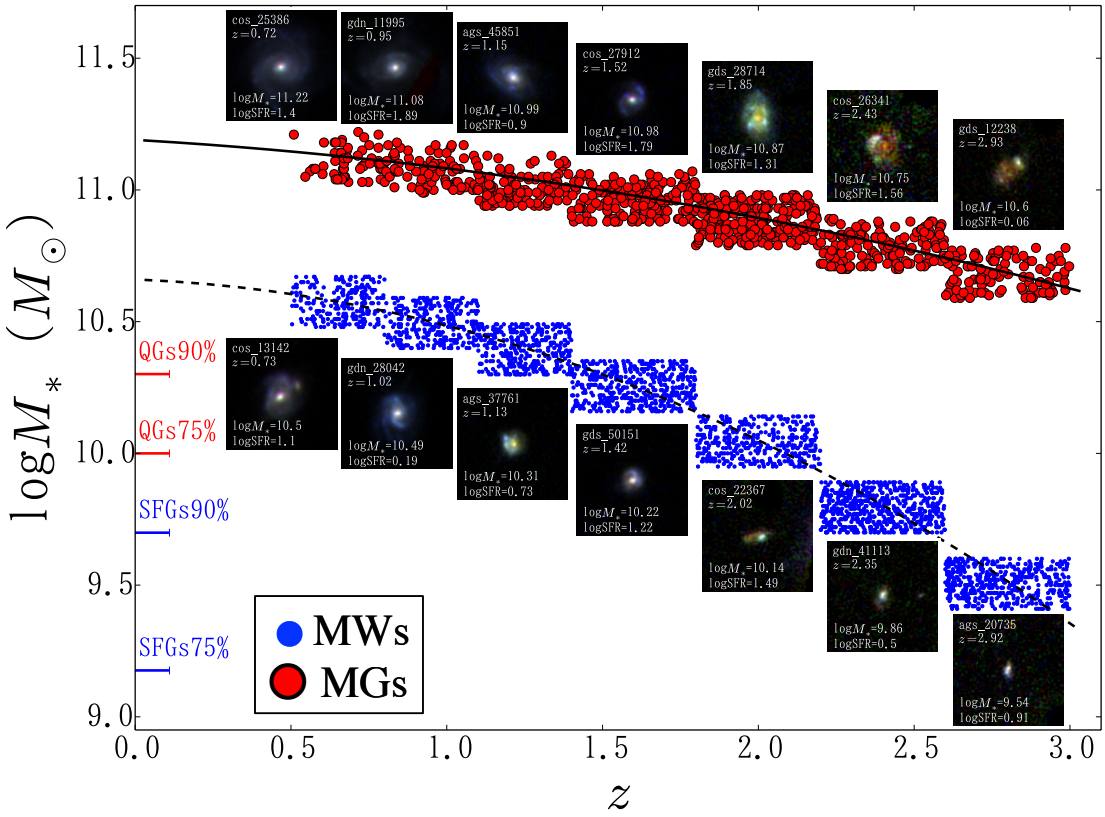

Massive galaxy progenitors (MGs; red circles) and Milky-Way mass progenitors (MWs; blue points) selected in this study. Typical example of galaxy at each redshift-mass bin is shown. The mass completeness for quiescent (QGs) and starforming galaxies (SFs) are indicated at the left of the plot.

Table 3.1: Number of Massive Galaxy and Milky-Way Mass Progenitors

CLASS	BAND	$0.50 \leq z < 0.80$	$0.80 \leq z < 1.10$	$1.10 \leq z < 1.40$	$1.40 \leq z < 1.80$	$1.80 \leq z < 2.20$	$2.20 \leq z < 2.60$	$2.60 \leq z < 3.00$
MW	F435W	83	102	95	97	85	192	131
	F606W	230	276	302	355	314	548	428
	F775W	88	115	126	138	92	201	149
	F814W	193	201	251	356	272	457	372
	F850LP	88	114	126	141	93	200	148
	F125W	261	313	357	496	374	597	470
	F140W	169	217	231	324	234	373	263
	F160W	260	313	358	494	379	603	488
MG	F435W	19	25	23	20	30	29	10
	F606W	50	77	90	128	140	90	50
	F775W	19	26	34	30	46	42	21
	F814W	41	59	79	128	146	84	52
	F850LP	19	26	35	29	50	40	19
	F125W	56	81	102	166	221	147	83
	F140W	39	62	72	103	145	102	45
	F160W	55	81	101	166	222	150	110

Number of galaxies in each redshift bin, each population, and each *HST* filter band. These galaxies are stacked in each bin and filter.

stellar mass. To select galaxies that are expected to be massive ($\log M_*/M_\odot \sim 11.2$) and MW-mass ($\log M_*/M_\odot \sim 10.7$) galaxies at $z \sim 0$, in this study I follow the constant cumulative number density criterion derived by Patel et al. [2013]. By selecting galaxies at a constant number density at each redshift, Patel et al. derived the stellar mass-growth equation as a function of redshift for MGs ($n \sim 1.4 \times 10^{-4}$ Mpc^{-3}),

$$\log M_*/M_\odot = 11.19 - 0.068z - 0.04z^2. \tag{3.1}$$

To compare the observed properties of MGs with less massive galaxies, I also select MW progenitors by using the number density ($n \sim 1.1 \times 10^{-3}$ Mpc^{-3}) derived by van Dokkum et al. [2013b],

$$\log M_*/M_\odot = 10.66 - 0.045z - 0.13z^2. \tag{3.2}$$

I convert the stellar mass with Kroupa [2001] IMF ($M_{*,\mathrm{K}}$) into one with Chabrier IMF ($M_{*,\mathrm{C}}$) through $\log M_{*,\mathrm{C}}/M_\odot = \log M_{*,\mathrm{K}}/M_\odot - 0.04$ [Cimatti et al., 2008]. Extracted stellar masses are $\log M_*/M_\odot \sim$ 10.68, 10.79, 10.89, 10.96, 11.00, 11.07 and 11.10 for MGs and $\log M_*/M_\odot \sim$ 9.51, 9.79, 10.04, 10.25, 10.40, 10.49 and 10.57 for MWs, respectively, at $\langle z \rangle \sim$ 2.8, 2.4, 2.0, 1.6, 1.2, 1.0 and 0.7.[2] All bins include > 10 for MGs and > 80 for MWs, which is stacked to gain higher S/N per pixel. The numbers of galaxies used for the stacking are summarized in Table 3.1.

Since galaxies could change their ranks by, e.g., major merging and quenching, I cut the sample with a range of ± 0.1 dex in the stellar mass. The sample in this study is selected with box in z-M_* space (Figure 3.1), as well as Patel et al. [2013] and van Dokkum et al. [2013b], rather than in a curved box where stellar mass criteria evolve continuously with redshift. The median values for

2. All the galaxies used for stacking are exhibited at `http://www.astr.tohoku.ac.jp/~mtakahiro/mori15apj/mori_15_rgb.pdf`

Table 3.2: Average Properties of Massive Galaxy and Milky-Way Mass Progenitors

CLASS	BAND	$0.50 \le z < 0.80$	$0.80 \le z < 1.10$	$1.10 \le z < 1.40$	$1.40 \le z < 1.80$	$1.80 \le z < 2.20$	$2.20 \le z < 2.60$	$2.60 \le z < 3.00$
MG	$\langle z \rangle$	0.69	0.95	1.23	1.61	1.99	2.39	2.78
	$\langle \log M_*/M_\odot \rangle$	11.11	11.08	11.01	10.96	10.89	10.79	10.68
	$\langle \log \mathrm{SFR}/M_\odot\,\mathrm{yr}^{-1} \rangle$	0.56	0.84	0.83	0.90	1.29	1.22	1.39
MW	$\langle z \rangle$	0.67	0.96	1.25	1.60	2.00	2.39	2.78
	$\langle \log M_*/M_\odot \rangle$	10.57	10.49	10.40	10.25	10.04	9.79	9.51
	$\langle \log \mathrm{SFR}/M_\odot\,\mathrm{yr}^{-1} \rangle$	0.61	0.75	0.85	0.83	0.95	0.74	0.79

Average properties of MGs and MWs.

M_*, z and SFR are summarized in Table 3.2.

3.2 Methodology

In the previous studies, discussion on galaxy radial profiles and their evolution are based on the light profiles. However, stellar mass-to-light ratio (M/L) is known to change along galaxy radius, as studied with spectroscopic information in the local universe [e.g., Kuntschner et al., 2010], and inferred by color variation at high-z [e.g., Szomoru et al., 2013], and the result was light-weighted, rather than mass-weighted. To mimic the effect both in redshift space and sub-galactic scale, it is necessary to estimate the M/L for each pixel by modeling the spectral energy distribution (SED). Here, I follow the method of "radially resolved" SED fit (hereafter radial SED), to derive the stellar mass and rest-frame colors for each pixel of galaxy radial profiles, which is introduced in Morishita et al. [2015]. Visual summary of the method is shown in Figure 3.2, and for the further details I refer the readers to the paper.

3.2.1 Conversion of 2-Dimensional Image to 1-Dimensional Radial Profile

Prior to stacking galaxies in redshift bins, I convert two-dimensional (2D) imaging data into one-dimensional (1D) radial profiles (hereafter, 1D-conversion) to obtain the average radial profile for each galaxy. The science images are convolved with PSF to the FWHM of F160W ($\sim 0.''18$), while the error maps are convolved in quadrature. The convolution kernels are generated by the "CLEAN" algorithm [Högbom, 1974], by providing PSF images provided by 3D-HST team (median stacked stars).

It is also important to correct the inclination of each galaxy before stack — otherwise, the stacked profile would result in morphologically biased (more centrally concentrated). I first extract the 2D image of 500×500 pixel ($\sim 250 \times 250$ kpc at $z \sim 2$) to subtract the local sky background. The local sky is estimated by masking all objects detected with `SExtractor` [Bertin and Arnouts, 1996], and calculate median of unmasked pixels.

In the 1D conversion I correct the effect of galaxy inclination. I obtain the projected axis ratio and apply the following equation to convert 2D imaging data into the inclination corrected 1D

Figure 3.2: Visual summary of the methodology

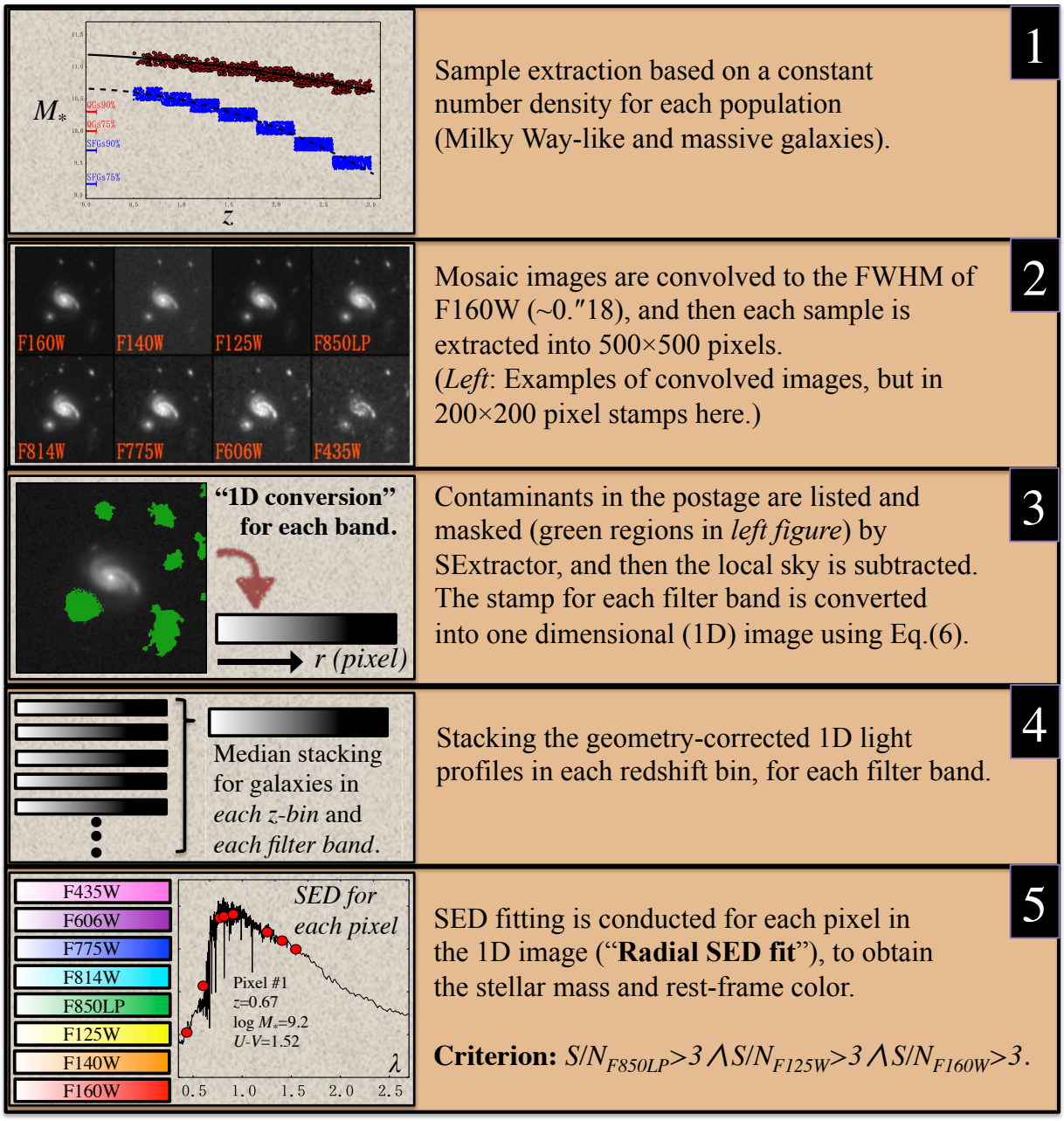

Visual summary of the methodology in Section 3.2, taken from Morishita et al. [2015]. [1] Sample selection (Section 3.1.2). [2] PSF matching (Section 3.2.1). [3] Sky subtraction and 1D conversion (Section 3.2.1). [4] Median stacking the 1D profiles in each redshift bin for each filter band (Section 3.2.1). [5] Radial SED fit for each pixel (Section 3.2.2).

profile,

$$\begin{aligned} r^2(\theta,q) = (\cos^2\theta + \sin^2\theta/q^2)(x-x_0)^2 \\ +(\sin^2\theta + \cos^2\theta/q^2)(y-y_0)^2 \\ +2\cos\theta(1-1/q^2)(x-x_0)(y-y_0), \end{aligned} \tag{3.3}$$

where θ and q are position angle and axis ratio obtained with `SExtractor`.

While the inner radius (< 2 kpc) seems more similar because the inclination effect is smaller at rounder inner region, this correction for inclination would compensate $\sim 30\%$ of light at the outer radius, which would also increase S/Ns [Morishita et al., 2015].

After transforming to 1D radial light profile for each galaxy in Section 3.2.1, I stack these 1D profiles in each redshift bin to obtain the composite radial profiles for each filter band. This procedure gives sufficient S/Ns for *each pixel* out to ~ 10 kpc of high-z galaxies. The stacking of galaxies is conducted for each filter band.

One concern of stacking analysis is the luminosity bias due to redshifts and stellar masses in each redshift-mass bin. To avoid the effect, I correct the luminosity for each galaxy by multiplying the following constant (i.e. K-correction+mass normalization),

$$K(\langle z\rangle, \langle M_*\rangle) = \frac{(1+z_{\rm obs})^3}{(1+\langle z\rangle)^3}\frac{\langle M_*\rangle}{M_{*,\rm obs}}, \tag{3.4}$$

where "obs" represents the observed quantity and brackets are the medians of each redshift bin, as shown in Table 3.2. The stacking allows MGs and MWs to have $\mathrm{S/N} > 3$ at > 10 pixel ($\gtrsim 5$ kpc at $z \sim 2$) from the galaxy center in the highest redshift bin.

3.2.2 Radially Resolved SED Fitting

I calculate radially resolved SEDs for the stacked radial profiles using FAST [Kriek et al., 2009], by adopting `GALAXEV` stellar population model [Bruzual and Charlot, 2003], assuming the solar metallicity and Chabrier [2003] IMF. The Milky Way dust attenuation of Cardelli et al. [1989] is adopted in range of $0 \leq A_{\rm V} \leq 4.0$ mag by step of 0.1. Age is set to range from 0.1 to either smaller of 10 Gyr or the age of the universe at the redshift of galaxies. Redshifts are set to the median values of the sample bins. The star formation history is assumed to be an exponentially-declining model, SFR $\propto \exp(-t/\tau)$, where t is the time since its star formation starts and τ is the e-folding timescale of SFR. It is noted that the exponential model is first proposed for local elliptical galaxies, and recent studies have shown that the delayed and truncated models would be consistent with observations of high-z star forming galaxies [Maraston et al., 2010, Barro et al., 2013]. However, I adopt the exponential model in this study because it is not possible with only the photometric data to discriminate any of these star formation histories [see also Abramson et al., 2016, Dressler et al., 2016]. Instead, I adopt an offset of the best-fit stellar masses derived with the three star formation histories (exponential, delayed, truncated models) as errors of the derived

parameters (stellar mass and star formation rate) of the exponential model. The error (~ 0.1 dex) is larger than those due to random photometric error calculated in Section 3.2.1.

3.3 Results

3.3.1 Radially Resolved SEDs

The surface stellar mass density profiles are shown in Figure 3.3. The stellar surface density is obtained down to $\log \Sigma_* / M_\odot \,\mathrm{kpc}^{-2} \sim 6$. The error for the stellar mass is estimated from the differences between the star formation histories, as described in Section 3.2.2. The error from the photometric uncertainties is comparatively small ($\Delta \log \Sigma_* / M_\odot \,\mathrm{kpc}^{-2} \sim 5$). It is noted that the radial SED fitting is conducted only for pixels where fluxes of F850LP, F125W and F160W have $\mathrm{S/N} > 3$ in order for the robust SED fitting, as these bands are sensitive to the Balmer break at $z > 1.5$.

The effect of a PSF convolution is corrected in Figure 3.3, by the method of Szomoru et al. [2010]; The best-fit 1D Sérsic profile with `GALFIT` [Peng et al., 2010], which takes account for the convolution effect, is derived firstly. Then, the residual between the observed and the best-fit profiles is added to the best-fit model, which is not *convolved*. Although the residual still remains convolution effect, I verify the method works well, by convolving the final "deconvolved" image with the original PSF kernel for F160W (the total offset from the original image is $< 1\%$). This reasonably reproduces the observed image, only except for outermost parts, which hardly affect the final conclusion. Direct convolution would usually introduce unexpected noise, especially for small size imaging data, and therefore I do not adopt in this study.

Figure 3.4 then shows the mass growth of each population separated at 2.5 kpc. The stellar mass of MGs is accumulated in the "inside-out" scheme, where central stellar component forms first and then mass growth mainly occurs at the outer part. For MGs in this study, I see the inner < 2.5 kpc region ($r < 2.5$ kpc, hereafter bulge) has already obtained a huge amount of stellar mass ($\log M_* / M_\odot \sim 10.6$) at $z \sim 2$, while this does not change significantly later. On the other hand, the outer part (> 2.5 kpc) monotonically increase the mass from $z \sim 3$ to $z \sim 1$, from $\log M_* / M_\odot \sim 9.7$ to $\log M_* / M_\odot \sim 11$, consistent with the inside-out scheme. I refer to the inner region as "bulge", because the bulge is expected to dominate the region, though for more specified definition I need additional analyses, such as the bulge-disk decomposition (see Chapter 5).

The stellar mass of MWs is accumulated at all radii in a similar way, also called as "self-similar" scheme, from $z \sim 2.8$ to 1.0, with slight surplus increases at the outer part at $z < 1$. The stellar masses in both parts grow from $\log M_* / M_\odot \sim 9.5$ to ~ 10.3 by a factor of ~ 7 over the observed redshift range.

I also show cumulative stellar mass profiles in Figure 3.5 with non-parametric half-mass radii. The half-mass radius of MGs evolves from ~ 1.9 kpc at $z > 2$ to ~ 4.8 kpc at $z < 1$, by a factor of ~ 2.5. The average size of high-z progenitors is consistent with those for compact galaxies observed at the similar redshift. Given their mass profile of MGs (and star forming properties, see Section 3.3.2), these galaxies trace the average evolution of compact galaxies.

Figure 3.3: Radial mass profiles

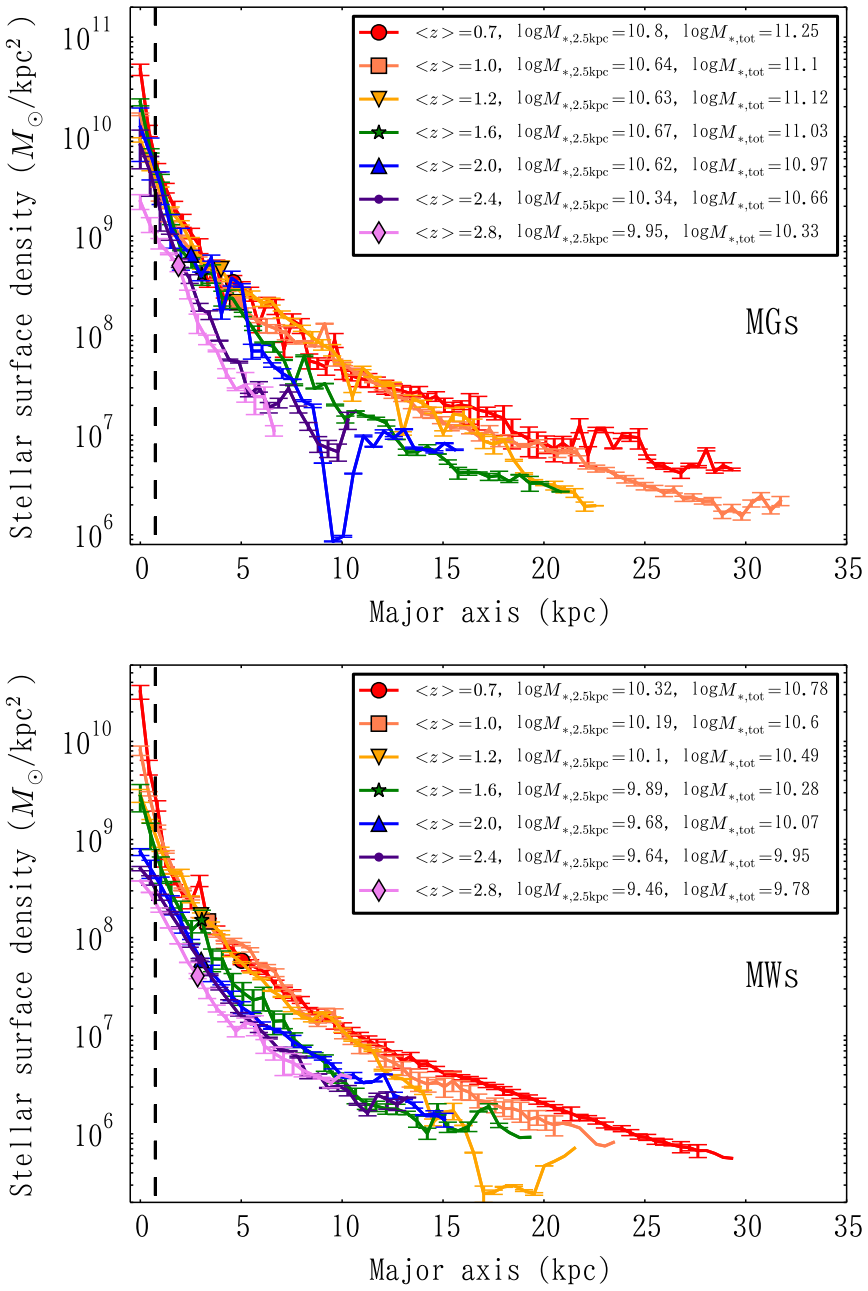

Radial stellar mass profiles of MGs (top) and MWs (bottom). The position of each symbol represents the half-mass radius, whose value is shown in the caption. The vertical dashed lines represent the radius that corresponds to the maximum PSF FWHM/2 for the full sample, although the PSF convolution effects are corrected (see the text). The bar represents the typical error for each radius, which is calculated based on the difference among the three different star-formation histories. Stellar mass within 2.5 kpc from the center ($M_{*,2.5\mathrm{kpc}}$) and total stellar mass ($M_{*,\mathrm{tot}}$) for each redshift bin are shown in the caption.

Figure 3.4: Stellar mass growth at $r < 2.5$ kpc and $r > 2.5$ kpc

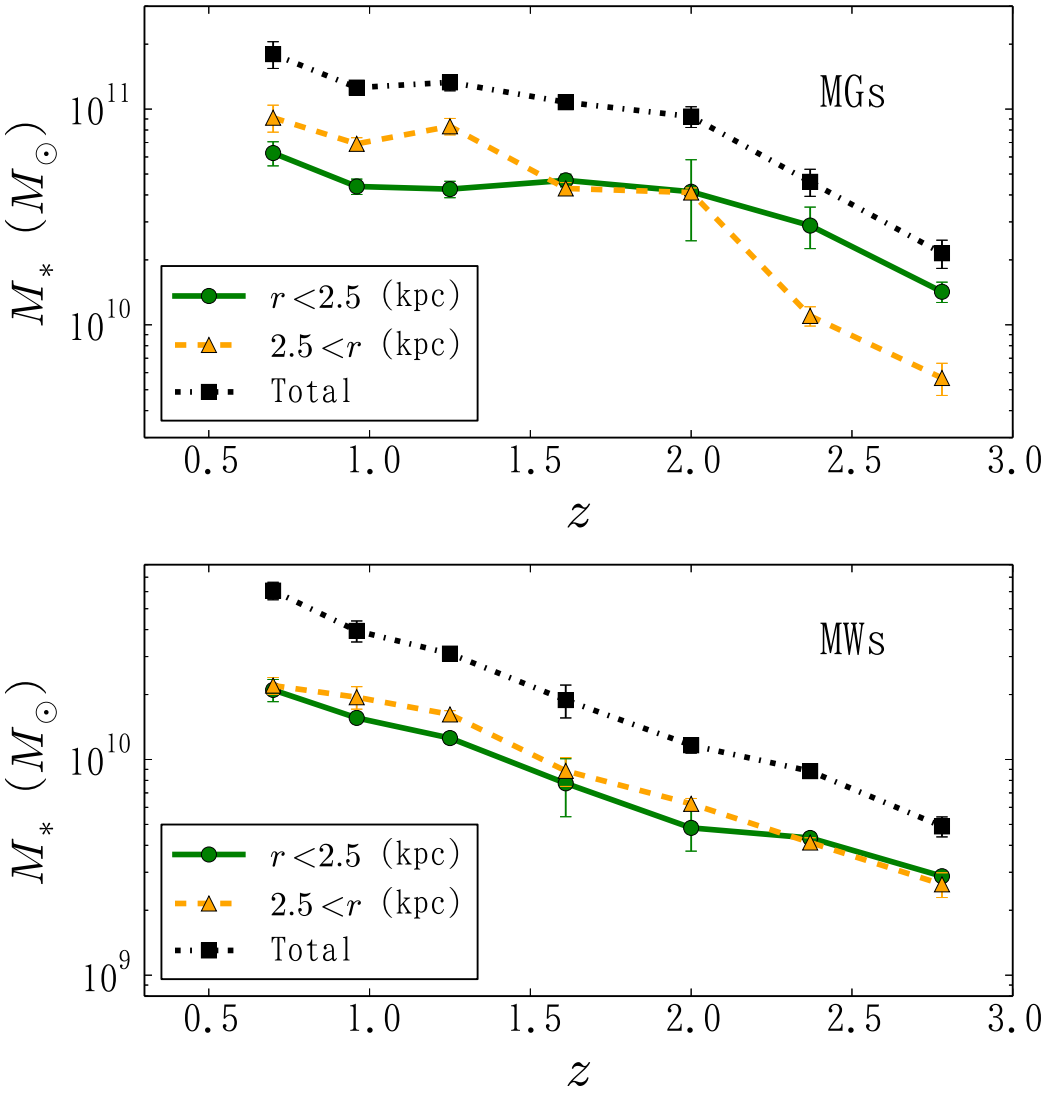

Stellar mass evolution in the inner (< 2.5 kpc) and outer (> 2.5 kpc) regions for MGs (top) and MWs (bottom). MGs complete the inner stellar mass growth at $z \sim 2$, and mostly increase at the outer radius ($r > 2.5$ kpc) thereafter ("inside-out"). MWs continuously increase mass at both inner and outer radii.

Figure 3.5: Cumulative radial mass profiles

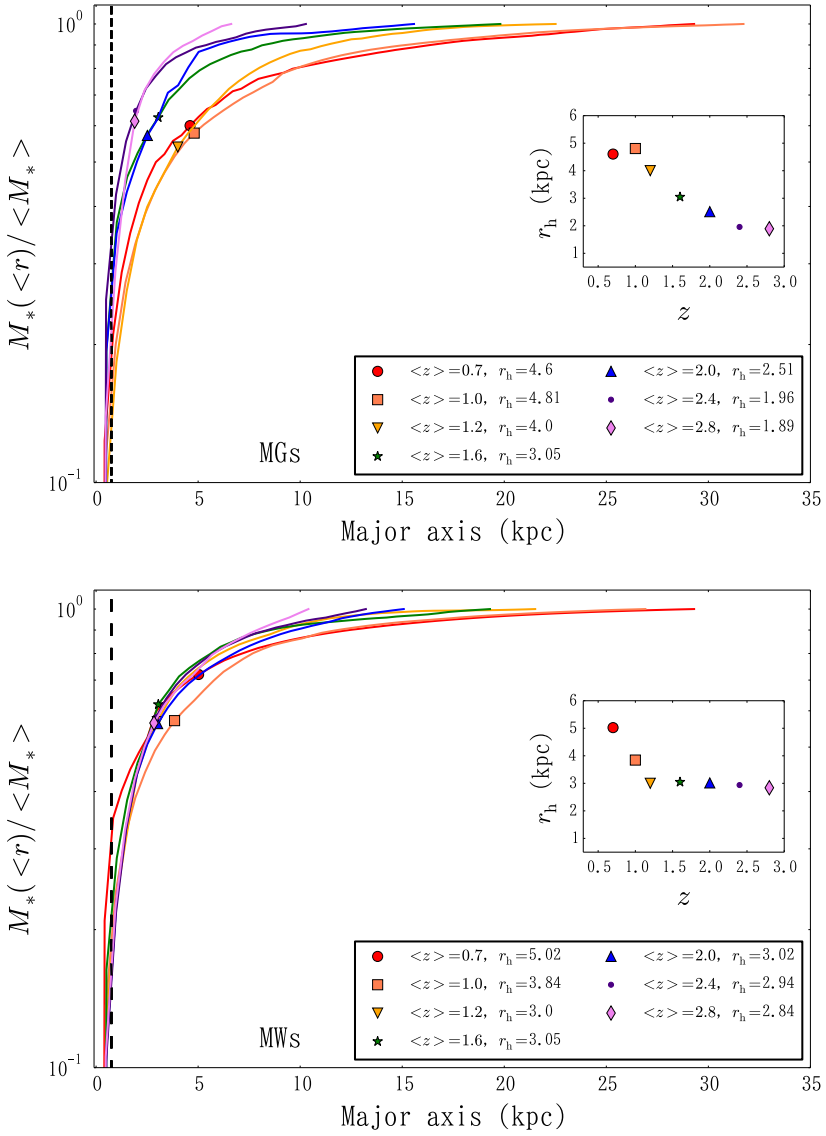

Cumulative stellar mass profiles of MGs (top) and MWs (bottom). Each profile is normalized to the total stellar mass. The vertical lines and symbols are the same as Figure 3.3. The evolution of the half-mass radius is in the inset. While the mass profiles of MWs show the self-similar evolution, those of MGs show inside-out evolution, where the accumulation of stellar mass continues at the outer part of galaxies.

For MWs, no change in size is observed at $1 < z$ ($r_{\rm h} \sim 2.8$), which is consistent with the self-similar evolution, while at $z < 1$ size mildly increases by a factor of ~ 2. The secession of star formation in the inner region (or *completion of bulge formation*) with ongoing star formation at the outer radius can consistently explain this (see also 3.3.2).

It is noted that the measured sizes for MGs are slightly smaller than those in Patel et al. [2013], who adopted the same selection criterion and derive the effective *light* radius $r_e \sim 6\,$kpc at $z \sim 0.5$. The offset could be originated by the effect of color gradients i.e. M/L is larger at the central part [e.g., Cappellari et al., 2006, Szomoru et al., 2013], which would make a radial stellar mass profile to be more centrally concentrated. The radial variations of stellar mass to H-band light ratio for both populations are shown in Figure 3.6. The slope of M/L varies over the redshift range, suggesting that the mass profile is not correctly reproduced only with the light profile, especially for MGs. Szomoru et al. [2013] also found that half-mass radii are $\sim 25\%$ smaller than half-light radii for the galaxies at $0.5 < z < 2.5$.

3.3.2 Radial Profile of Rest-Frame Colors

The UVJ colors derived from the best fit SED templates are used to diagnose galaxy star forming properties [Williams et al., 2009, Whitaker et al., 2012]. The UVJ diagrams of the stacked radial profiles are shown in Figure 3.7. The criteria for passive and star forming galaxies were originally defined in Williams et al. [2009] for galaxies at $z < 2$, and updated for $2 < z < 3$ galaxies in Morishita et al. [2014] (Chapter 2).

The symbols are distinguished according to the distance from the galactic center to see the inner ($< 2.5\,$kpc, or bulge) and outer ($2.5 < r/\,{\rm kpc} < 10$) colors separately, inspired by the previous section and recent findings of the relation between quiescence and compactness of high-z galaxies [Franx et al., 2008, Cheung et al., 2012, Woo et al., 2014]. In all redshift bins, the inner pixels locate in the reddest region, which is in agreement with the idea of down-sizing (i.e. the inner part of galaxies evolve faster than outer part), as found in [Vila-Costas and Edmunds, 1992, Wuyts et al., 2012, Szomoru et al., 2013]. It is noted that although dust attenuation could make galaxy colors red, it is trivial in this case. Dust attenuation would affect the colors to shift along the quiescent criteria, and would not change the galaxy property between quiescence and starforming.

The $U-V$ color (the vertical axis in Figure 3.7) traces the redshift evolution of the strength of 4000 Å and Balmer breaks, which can be used to conjecture when and how the quenching starts for each part of the populations. For MGs, quenching in the inner part starts at early epoch, $z \sim 2.0$. The outer part is following with slight delay, and the color reaches the passive criterion at $z \sim 1.0$. For MWs, on the other hand, the bulge color starts to deviate at $z \sim 2$ from the outer region. After that, the bulge color reaches the passive criterion at $z \sim 1.0$, while star formation is still ongoing at the outer part — the "coexistence" of quenched bulge and star forming disk. I discuss these findings in the following section along with the result of the radial stellar mass profiles in Section 3.4.

Figure 3.6: Radial distribution of Mass-to-Light ratio

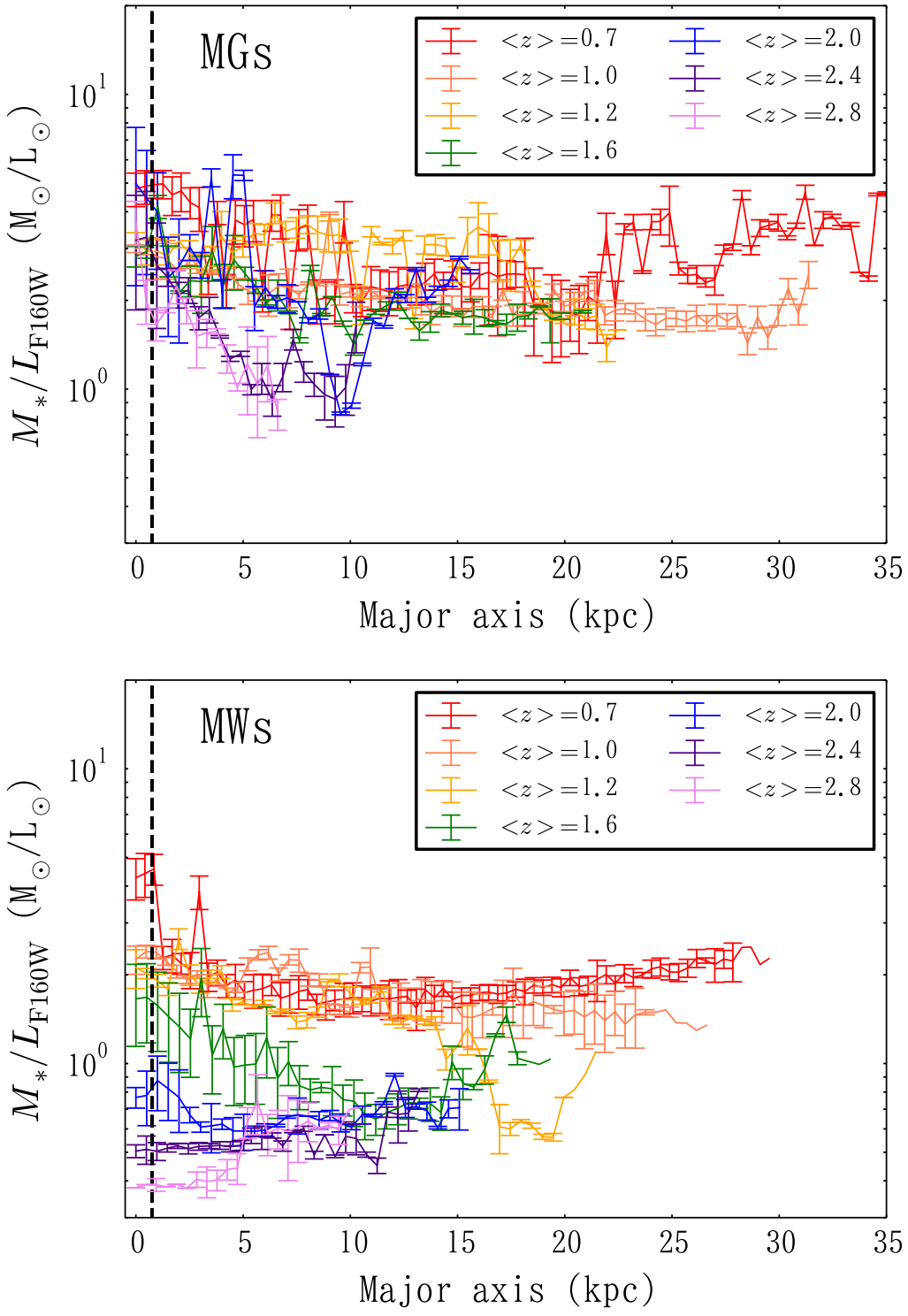

Radial variation of mass-to-F160W light ration of MGs (top) and MWs (bottom). Negative gradients are observed for MGs at all redshifts, and for MWs at $z < 1.6$, which make mass profiles more centrally-concentrated than light profiles.

Figure 3.7: Rest frame UVJ-diagram

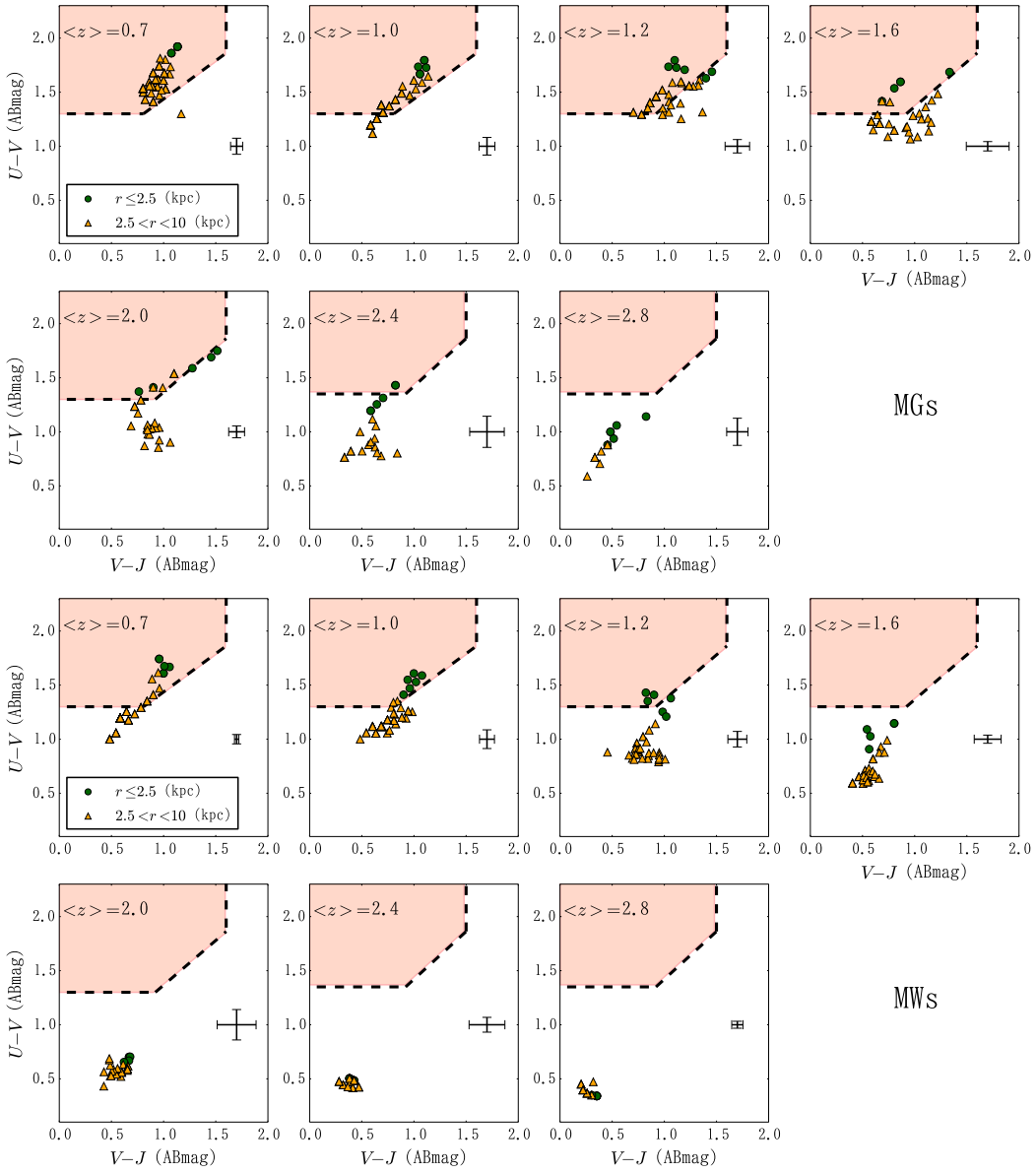

Rest-frame UVJ diagrams for MGs (top) and MWs (bottom). The symbol represents each pixel, and is distinguished using the distance from the galactic center (green circles for $r < 2.5$ kpc and yellow triangles for $r > 2.5$ kpc). The dotted lines are the boundary for quiescence (hatched region) defined in Williams et al. [2009] at $z < 2$ and Morishita et al. [2015] at $z > 2$. The error bars represent the typical error in the colors. The colors evolve from the inner to outer regions, a common trend for both populations.

3.4 Discussion

3.4.1 Inside-out Mass Growth of Massive Galaxies

As shown in Section 3.3.2, the stellar mass profiles of MGs and MWs evolve in different ways. The former evolves in *inside-out* way, while the latter in *self-similar* way.

Inside-out scenario claimed that massive bulges appeared at $z \sim 2$, or even earlier [e.g., Nelson et al., 2014, Marsan et al., 2015], and then it gains the rest of mass at the outer part by the accretion of less massive satellite galaxies, without dissipation process [e.g., Naab et al., 2009, Hopkins et al., 2009a, Oser et al., 2010]. It is clear in the top panel of Figure 3.4 that the massive bulge of MGs ($\log M_{*,2.5\mathrm{kpc}} > 10.5$) has already formed at $z \sim 2$, and the mass growth mostly occurs at the outer part thereafter ($> 2.5\,\mathrm{kpc}$).

One virtue of inside-out evolution scenario is that it can consistently explain the observed size growth of r_h by a factor of $\sim$ 2-5, as is also observed for *light* profiles [van Dokkum et al., 2010, Patel et al., 2013]. This size growth is expected to be driven by the mass growth at the outer part of galaxies since $z \sim 2$ — more than $\sim 75\%$ of the total stellar mass has been accumulated [Oser et al., 2010].

The formation of bulges at $z > 2$ with $\log M_{*,2.5\mathrm{kpc}} \sim 10.3$, on the other hand, is related to violent dynamical mechanisms at higher redshifts, such as major merger and clump migration [e.g., Dekel and Burkert, 2014, Barro et al., 2014], which is beyond the present scope (see Chapter 5).

3.4.2 Self-similar Mass Growth of Milky-Way Mass Galaxies

In contrast to MGs, the mass profile of MWs is found to evolve in *self-similar* way, where the mass accumulation at inner and outer parts are comparable, as shown in the bottom panel of Figure 3.4. This similarity is a consequence of the continuous bulge growth at $z > 1.0$, while MGs shows much less or no bulge evolution after $z \sim 2$. At $z < 1$, after the star formation in bulge region stops (Section 3.3.2), the mass growth become less uniform but more growth in the outer part i.e. disk. In the local universe, and our Galaxy, the typical Milky-Way mass galaxies have prominent bulges without forming stars. By considering these evidence, the observed evolution of MWs in this study (self-similar scheme) happen at $z \gtrsim 1$, and then follow a similar scheme as MGs, inside-out. In this sense, MWs' evolution can be interpreted as delayed compared to more massive galaxies, MGs, i.e. the down-sizing of galaxy evolution. While the bulge star formation has already stopped for the observed MGs, MWs have the evidence of bulge formation in the observed redshift range, which is a sweat spot to study the mechanism, such as bulge formation and quenching.

3.4.3 Diagnosing the Quenching

In this subsection I investigate the shutdown of star formation activities, or *quenching*, by using the rest-frame color profiles. Radially resolved $(U-V)$ colors provide us how the starforming region turns to be quiescent i.e. "how the quenching proceeds" for the present galaxies. As is seen in the

Figure 3.8: Redshift evolution of $U-V$ color

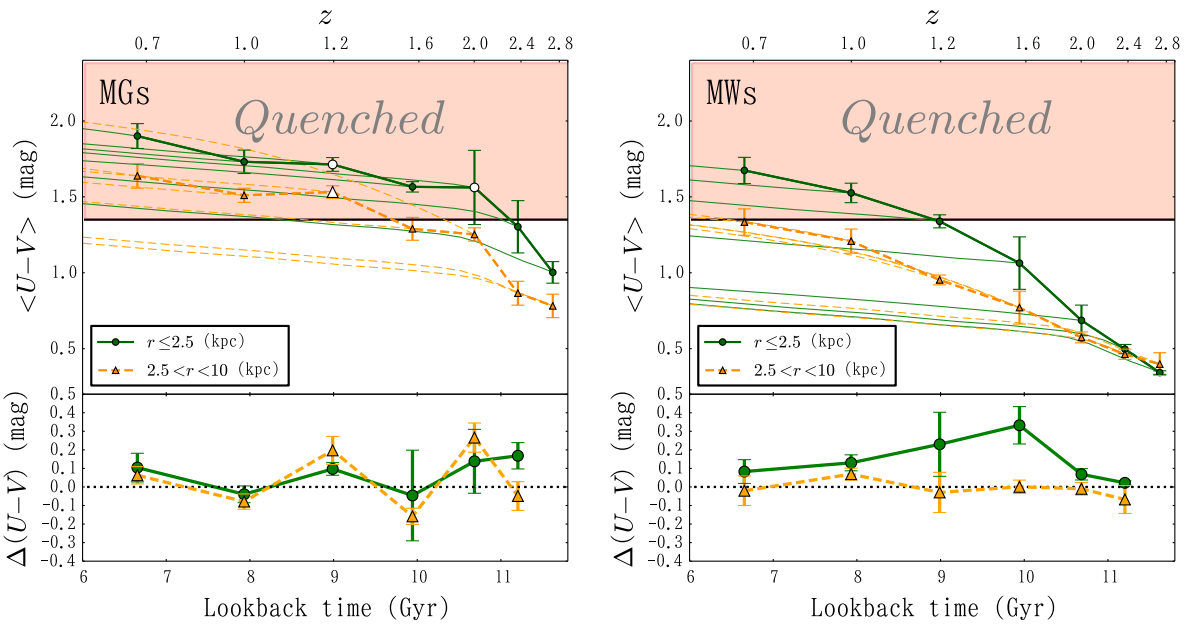

Top: evolution of the rest-frame $U-V$ colors of the inner ($r < 2.5$ kpc; green circles) and outer ($2.5 < r < 10$ kpc; yellow triangles) regions of MGs (left) and MWs (right). The error bar represents the typical error for $U-V$ at each redshift. The hatched quenched region is set with $(U-V) > 1.35$ mag. The data points located out of the quiescent hatched region within the error, whereas $(U-V) > 1.35$ mag are shown with open symbols to distinguish them from the quenched sample. The model predictions of the $U-V$ color (thin lines) are depicted with the best-fit SED profiles at each redshift and the population synthesis model of `GALAXEV` to see when each region becomes "unusually red or quenched. *Bottom:* comparison of the observed and model $U-V$ colors at each redshift, where I define $\Delta(U-V) \equiv (U-V)_{\rm obs} - (U-V)_{\rm model}$. The excess of $(U-V)_{\rm obs}$ in the inner regions ($r < 2.5$ kpc) at $z \sim 2.4$ and $z \sim 1.6$ for MGs and MWs, respectively is observed, while no excess are seen in the outer regions for either populations.

previous section, the inner regions keep reddest at any redshift bins. This trend is common for both populations, and can be interpreted as the down-sizing scheme.

For further investigation of the quenching, I compare the observed color evolution of bulges and outer regions of MGs and MWs in Figure 3.8 with the evolution derived by stellar population models. To do this, I calculate for each epoch the expected color at the next epoch by using the best-fit SED template and population synthesis model, and then compare it with the actually observed color at the next epoch. The SED model is prepared with the best-fit parameters derived in the same manner in the previous section, and its evolution is calculated with GALAXEV by following the derived SED parameters (star formation rate, τ and age) at each redshift to the next redshift, i.e. I obtain the model $U-V$ color, $(U-V)_{model}$, at the ith redshift, z_i, by using the one expected from the $(i-1)$th redshift to compare with the observed $U-V$ color, $(U-V)_{obs}$, at z_i. Shown in the top panel of Figure 3.8 with thin line is the model evolutions of $U-V$ color for each redshift. I set "Quenched" region (hatched) as $(U-V) > 1.35$.

Since GALAXEV model here take account of mildly declining star formation history, the model and observed quantities should be matched unless rapid termination of star formation happens. The comparisons of the colors for both populations are depicted in the bottom panels of Figure 3.8, with $\Delta(U-V) \equiv (U-V)_{\rm obs} - (U-V)_{\rm model}$. I see that the bulges of MWs and MGs show color excess (to redder) at $z \sim 1.6$ and $z \sim 2.4$ (over a time scale of $\sim 1\,$Gyr), respectively, while the outer parts of both populations show a good consistency with the model. Therefore, I conclude that the deviation in the RF color is caused by the shutdown of star formation activities in the inner regions (I hereafter refer to as "bulge quenching"), while the outer parts evolved just as expected by the best-fit SED models. Interestingly, the quenched redshift is similar with the redshift where bulge mass growth stops for each population (Section 3.3). To explain the observed bulge quenching, I discuss few possible mechanisms suggested by recent theoretical and observational studies.

The first one is the termination of cold gas supply into the central part by virial shock at the halo radius. The halo masses, $M_{\rm h}$, of MWs and MGs at the quenching epoch are $M_{\rm h} \sim 10^{12} M_\odot$ at $z \sim 1.6$ and $M_{\rm h} \sim 3 \times 10^{12}\ M_\odot$ at $z \sim 2.4$, respectively, based on the halo mass-stellar mass matching by Behroozi et al. [2013]. The quenched halo masses of both populations are not identical for both populations. This can be explained cold flow at higher redshift [e.g., Dekel and Birnboim, 2006], where cold gas continues to flow by the central part of massive halo at higher redshift ($M_{\rm h} > 10^{12} M_\odot$ at $z \sim 2$). At lower redshift, on the other hand, all of it is shock-heated even in the system of lower halo mass ($M_{\rm h} \sim 7 \times 10^{11} M_\odot$). The termination of gas flow into the central region is also explained by the fact that gas with smaller angular momentum preferentially falls into the central region while one with larger momentum, which accrete at later epoch, can not fall and remains at the outer radius.

Another mechanism is the one called "morphological quenching" [Martig et al., 2009], where the formation of bulge stabilizes the gas kinematics and prevents the system forming stars. Recent observations with IFUs have found that the bulges of high-z massive galaxies are indeed stabilized with high Toomre Q-parameter [e.g., Genzel et al., 2014]. Beside the finding in this study, the correlation between the quiescence and morphological compactness also supports this scenario [Franx et al., 2008, Cheung et al., 2012, Woo et al., 2014].

Figure 3.9: Radial variation of individual light profile

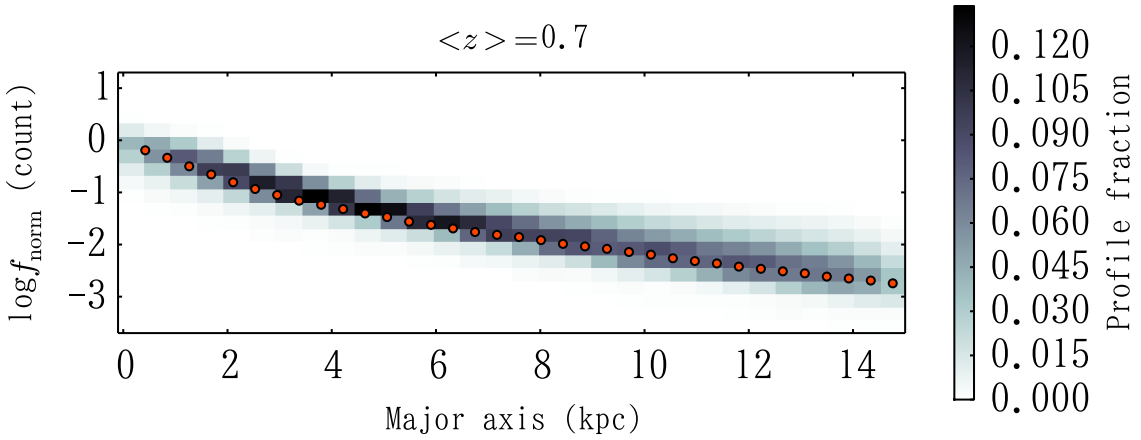

Examples of the radial light profile for MWs at $z \sim 0.7$. Grayscale represents the fraction of radial light (F160W) profiles of the galaxies used for stacking. The median profile is shown as red circles. Each flux is normalized at the center of the median profiles.

It is noted the bulge of MWs keep evolution even after its quenching epoch at $z \sim 1.0$, though weaker than found at $z > 1$. This suggests that there should be a mechanism that transports some amount of stars ($\sim 5 \times 10^9 M_\odot$) into the bulge region, from the outer disk, such as stellar migration [e.g., Sellwood and Binney, 2002].

3.4.4 Morphological Variation from the Average

Previously, galaxy morphology and structural variance is assessed either qualitatively [visual investigation; e.g., Kajisawa and Yamada, 2001] or quantitatively with a set of morphological parameters [e.g., Lotz et al., 2004]. In this section I introduce a new method to quantify the galaxy morphology by using obtained galaxy profiles.

Figure 3.9 shows an example of this exercise — radial luminosity profile density of all galaxies in $z \sim 0.7$ bin is compared with the median radial profile. The median and individual profiles here are the luminosity in F160W-band, since the stellar mass profile for each sample is not obtained in this study. The individual 1D light profiles are reduced and converted in the same manner for the radial SED, including mask for background galaxies and redshift/stellar mass correction of Equation 3.4.

I define the variety of galaxy profile by evaluating the distribution of residuals as,

$$\Delta_{\mathrm{norm},x} \equiv \frac{1}{S_x} \sum_i^x \left| \frac{f_{i,\mathrm{median}} - f_{i,\mathrm{obs}}}{f_{i,\mathrm{median}}} \right|, \tag{3.5}$$

where I set $x < 2.5\,\mathrm{kpc}$ and $2.5 < x/\,\mathrm{kpc} < 10$ in the following to see the radial dependence of the variety. S_x is the total pixel within the range of x. In Figure 3.10 I show the distribution of $\Delta_{\mathrm{norm},x}$

Figure 3.10: Histogram for radial variation

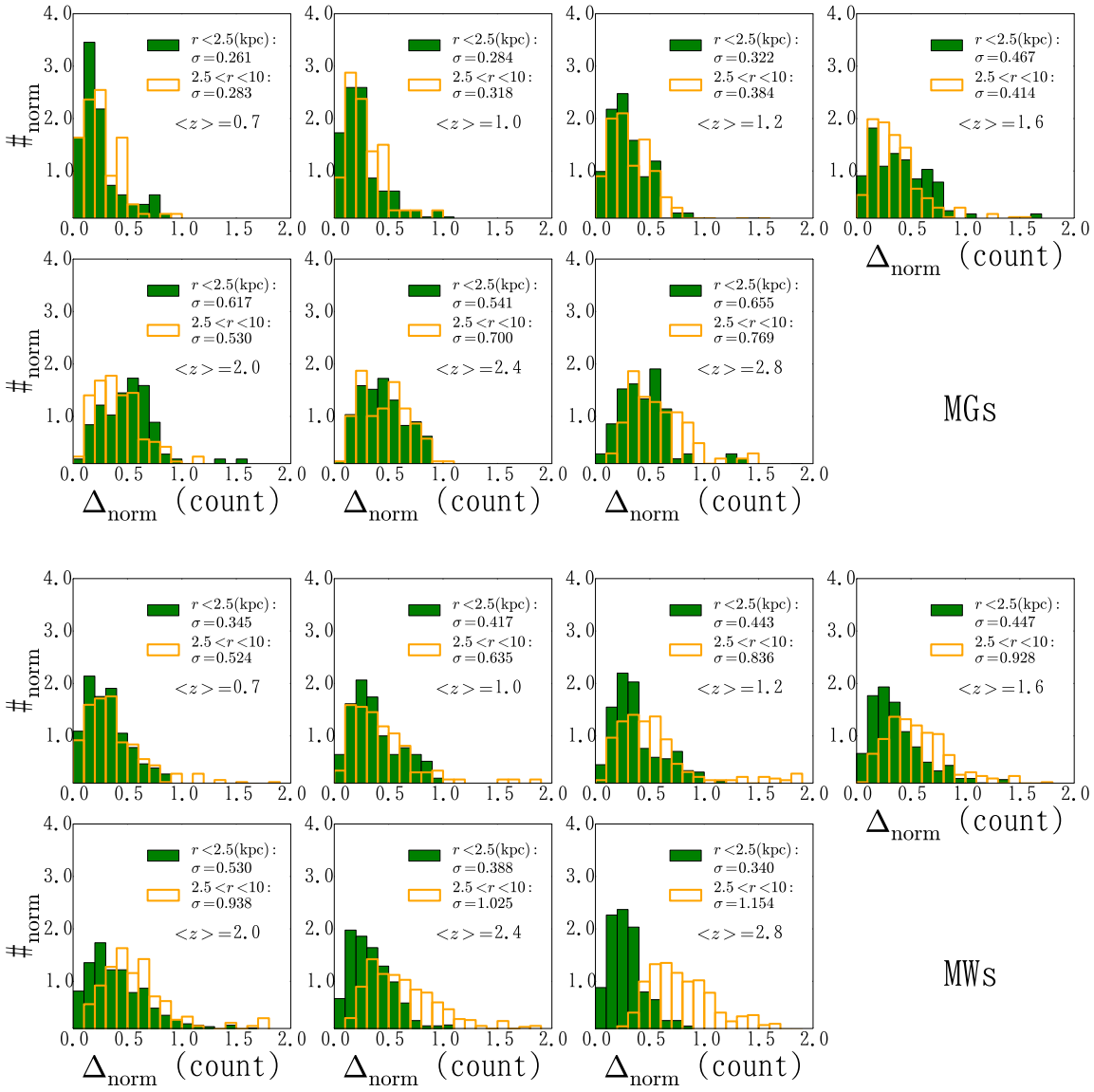

Histograms of the radial variations, $\Delta_{\rm norm}$ (see the main text for the definition), for MGs (top) and MWs (bottom) of $r < 2.5\,$kpc (filled green histograms) and $2.5 < r < 10\,$kpc (unfilled yellow) for each redshift panel. The dispersion (σ) of distribution, which represents the variety of galaxy morphology from the average, is shown in each panel.

for each redshift bin. Then I evaluate the dispersion, σ, around the mean of the distribution, which is given in each panel. Since the scatter of background noise for each light profile could affect the quantity, I calculate the error for σ by assuming the maximum deviation from the best fit value. The results do not change in other filter bands, as long as the rest-frame V- or longer wavelength bands are used. The radial variety shows increase at shorter wavelength, part of which is caused by stochastic and strong emission line in the optical/UV light.

The evolution of σ over the redshift range is then shown in Figure 3.11. Both populations are characterized with different features. MGs have the peak at $z \sim 2.8$ (or possibly higher redshift), and the morphological variety rapidly converges down to ~ 0.2 at $z \sim 0.7$. The finding suggests very quick transition into morphological similarity, in entirety, after the formation of bulge at $z \sim 2$. For MWs, on the other hand, σ of the bulge peaks around $z \sim 2$, and moderately decreases toward the lower redshift, whereas at the outer part σ remains large (~ 0.6). This is consistent with the derived picture in Section 3.3 that the formation of bulge at $z \sim 1$, while star formation at the outer part has continued rather randomly over the entire redshift. This provides further insight into understanding of the self-similar evolution, where the bulge mass grows by a factor of ~ 7 from $z > 2$ to $z \sim 0.7$, as discussed in Section 3.3.2.

The results above are well explained in the physical context by comparing the evolution of average SFRs with those of σ in Figure 3.11. The median SFRs are estimated from the SED fitting for each sample in the 3D-HST catalog, and summarized in Table 3.2. The SFRs for MWs and MGs peak at $z \sim 2.0$ and $z \sim 2.8$, respectively, which are both consistent with the result of the variety peaks. It is reasonably explained by the fact that the galaxy morphology begins to have variety when the star formation activity becomes high at, e.g., clumpy regions. Although the present study is based on the stellar mass, it would be natural to speculate that the peak redshift also depends on the halo mass of the host galaxy; the star formation rate of galaxy in massive halo peaks at higher redshift and rapidly decline, whereas in smaller ones it peaks at lower redshift and slowly declines [Behroozi et al., 2013, Moster et al., 2013, McDermid et al., 2015].

The evolution of the morphological variation is consistent with the results of the quenching diagnosed by the UVJ colors in Sections 3.3.2 and 3.4.2. The star formation in disk-like (younger) galaxies randomly occurs in both inner and outer regions, mainly driven by gas accretion. The galaxy merger also increases the morphological variety. Although determining the main mechanism causing morphological variety at each epoch is beyond the present study, both mechanisms would be possible to make the galaxy morphology amorphous according to visual inspection of each galaxy image.

After quenching, given no gas accretion which induces significant star formation, the system would be dynamically relaxed ($t \sim 2$ **Gyr**) and converge to a similar morphology. The quenching of galaxies happens at the corresponding redshift of the appearance of morphologically well-featured galaxies at $z \sim 1$ [Dickinson, 2000, Labbé et al., 2003, Conselice et al., 2005, Ravindranath et al., 2006].

Figure 3.11: Redshift transition of morphological variety

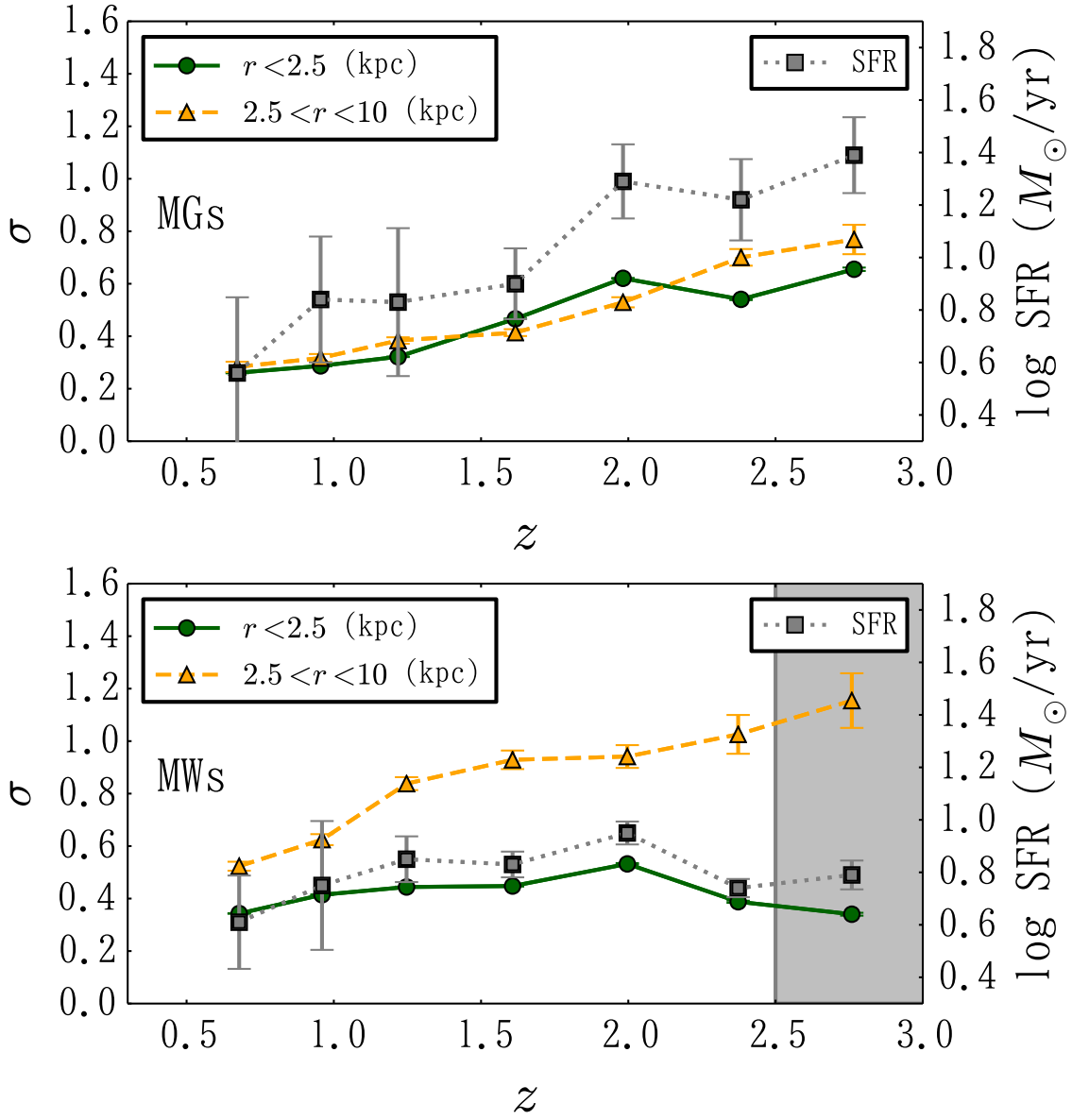

Redshift transitions of the morphological variety, σ, of $r < 2.5$ kpc (green solid line with circles) and $2.5 < r < 10$ kpc (yellow dashed line with triangles) regions as a function of redshift for MGs (top) and MWs (bottom). The sample in the highest redshift range (shaded region; $2.5 < z < 3.0$) of the bottom panel has weaker completeness (though still $> 75\%$) and might be biased toward more luminous galaxies (and higher σ). Average star-formation rates (gray squares with dotted lines) are derived from the 3D-HST catalog. The error bar for the SFR represents the dispersion at each redshift bin.

3.5 Summary

This chapter is summarized as follow;

1. MGs accumulate the stellar mass in the inside-out way, obtaining more than 75% of the total stellar mass at the outer part (> 2.5 kpc) after the rapid formation phase of the massive bulge ($M_* \sim 4 \times 10^{10} M_\odot$) at $z > 2$ (Figures 3.3, 3.4 and 3.5).

2. MWs accumulate the stellar mass in the self-similar way in bulge and disk. After its quenching at $z \sim 1$, the bulge still grows by $\sim 5 \times 10^9 M_\odot$ by $z \sim 0.5$.

3. Quenching in galaxies was observed and was found to occur strongly depending on the stellar masses of galaxies and bulges. The finding suggests the evidence of bulge-related quenching mechanisms, such as morphological quenching (Figures 3.7 and 3.8).

4. By comparing the median and individual light profiles, I evaluated the evolution of the varieties of galaxy 1D radial profile for the first time. The varieties are relevant to the observed star formation activities (SFRs and rest-frame colors) and the appearance of morphologically well-featured galaxies (Figures 3.9, 3.10, and 3.11).

In this study, I investigated the evolution of "average" properties, by assuming galaxies would evolve at a constant number density. Two populations with different masses have different epochs of bulge quenching, inside-out and self-similar growth of the stellar mass, more or less explained by down-sizing effect, similarity and variety of the morphology, manifestation of two main structure (bulge and disk) while undermining star formation. However, as seen in the last section, there is still diversity within each population, which reminds that galaxy evolution cannot be explained in any single scenario, but even the interpretation could be biased. For example, the mixture of bulge dominated galaxies and disk dominated ones with similar stellar masses at the similar redshifts (which are really observed) in a single z-M_* could bias the results, because the analysis here did not intend to solve the problem. To further investigate the evolutionary picture implied from the average analysis here, there needs to see individual galaxies and what is actually happening to them, *as will be studied in the second part of this thesis.*

CHAPTER 4
[PART 2] CASE STUDY: MASSIVE COMPACT GALAXY AT $z \sim 1.9$

Brief summary[1]

In the previous chapters, I have discussed the evolution scenario of massive galaxies, based on observed structural properties and colors. In particular, the observed properties of the massive progenitors at $z \sim 2$ are alike what we are observing at the same redshift, i.e. massive compact galaxies. This convinces that compact galaxies are likely to evolve in the inside-out scheme, as inferred by a number of observational and theoretical studies. In the scenario, a number of gas-poor minor merger to massive galaxies can grow the outer profile and result in the significant size-evolution by a factor of $\sim$ 2-5.

However, as I have already claimed, the derived *average* picture can be a mixture of different populations, because, for example, bulge dominated and disk dominated galaxies were not analyzed separately in the previous studies. The accretion phase of the two-phase scenario has not convinced directly yet.

In fact, there is an observational claim that the number of dry merger event, as expected by counting satellite galaxies around massive galaxies, is not enough to explain the expected size/mass evolution [Mármol-Queraltó et al., 2012, Bluck et al., 2012, Newman et al., 2012]. Detecting less massive satellites ($\log M_*/M_\odot < 10$) around massive galaxies, however, might be missed with the moderate imaging depth in the previous studies.

In this chapter, as a case example, I search accreting satellites around a massive compact galaxy ($\log M_*/M_\odot \sim 10.6$) found at $z_{\rm spec}= 1.9213$. Very deep *HST* imaging data in the eXtreme Deep Field [XDF; Illingworth et al., 2013], with 5σ-limiting magnitude of $m_{\rm ACS} \sim 30.6$ ABmag, which corresponds to $\log M_*/M_\odot \sim 7.2$ at the redshift, enables to find lower mass satellites than previous studies. The photometric redshift measured with 12 *HST* multi-band images confirms 34 satellites out of the candidates.

Interestingly, I find most of the satellites have the rest-frame colors consistent with star forming galaxies, contrary to an expectation of dry minor merger scenario. Although uncertainties in the obtained star formation rates and photometric redshifts of the satellites is not negligible, I conjecture three possible scenarios for the compact galaxy to a local galaxy — 1 dry merger, 2 in-situ star formation in the satellites and then dry merger, and 3 wet merger. While accretion of the existing total stellar mass in the satellites (1) is *not enough* to achieve the mass growth predicted by simulations designed for the two-phase scenario, the contribution by the in-situ star formation in the satellites (2) would compensate the deficit. The scenario requires satellites to keep the observed in-situ star formation and then to consume most of the starforming gas before accreting to the central massive galaxy; otherwise, the satellites would induce additional star-formation in the center of the massive galaxy, which then reduce the galaxy size [e.g., Covington et al., 2008].

1. This section is based on Morishita and Ichikawa [2016].

Since the central galaxy is expected to be in a massive halo ($\log M_h/M_\odot \sim 12$), gas stripping can be a possible mechanism responsible for the satellite quenching.

To further study the fate of compact galaxies, a large sample of massive bulge galaxies at the later epoch (as the relic of compact galaxies) is needed (see Chapter 5).

4.1 Data

4.1.1 XDF and UVUDF Imaging

I make use of the multi-band imaging data from XDF project [Illingworth et al., 2013], which compiled and stacked all the data taken with 9 filter bands of *HST*/ACS and WFC3-IR in the HUDF field for 10.8 and 4.7 arcmin^2 for ACS, respectively. The limiting magnitude for each band reaches 29.1-30.3 mag with $0\farcs35$ aperture, much deeper than CANDELS' deep observation of ~ 28 mag or any other ground-based observations. In addition, I utilize the deep UV imaging data from the Ultraviolet Hubble Ultra Deep Field [UVUDF; Teplitz et al., 2013], which is taken with WFC3-UVIS for F225W, F275W and F336W bands, where 5σ limiting magnitude is 27.8, 27.7 28.3 mag for $0\farcs2$ aperture, respectively.

4.1.2 Host Compact Galaxy: XDF463

The compact galaxy, XDF463, is originally found in Szomoru et al. [2012], out of 21 passive massive galaxies at $1.5 < z < 2.5$ in the GOODS-South field. XDF436 is the only galaxy in the XDF field with a spectroscopic redshift, $z_{\rm spec.} = 1.9213$ [van Dokkum et al., 2013b]. The location of XDF463 and its virial radius (extrapolated from a simulation; see the following section) are shown in a pseudo color image in Figure 4.1. Fortunately, XDF463 resides in the central part of the XDF, where I can search its satellite galaxies impartially.

The structural parameters of XDF463 is derived with `GALFIT`, assuming a single Sérsic profile, $r_e = 0.55$ kpc and $n = 3.13$. The stellar mass and star formation rate (SFR) of XDF463 are estimated with `FAST` code, where I set the stellar population model of `GALAXEV`, and fix to the solar metallicity and Chabrier [2003] IMF. The Calzetti et al. [2000] dust law is adopted in the range of $0 \leq A_{\rm V} \leq 3.0$ mag by step of 0.1, and age is set to the range from 0.1 Gyr to the age of the universe at the galaxy redshift. Two star formation histories, exponentially-declining SFR(t) $\propto \exp(-t/\tau)$ and delayed SFR(t) $\propto t \times \exp(-t/\tau)$, are applied independently, as discussed in Chapter 3 [see also Wuyts et al., 2012]. As such, I use the average SFR of those derived with both histories and refer to the difference as the systematic error. The rest-frame UVJ colors are derived by using the the best-fit SED template, convolved with the corresponding filters.

4.1.3 Theoretical Expectation

From the derived stellar mass of XDF463, $M_* \sim 3.9 \times 10^{10} M_\odot$, I extrapolate the virial radius ($r_{\rm vir} \sim 300$ kpc) and halo mass ($M_h \sim 1.6 \times 10^{12} M_\odot$) by matching the stellar mass to the simulated

Figure 4.1: Spatial distribution of XDF463 and its satellite galaxies

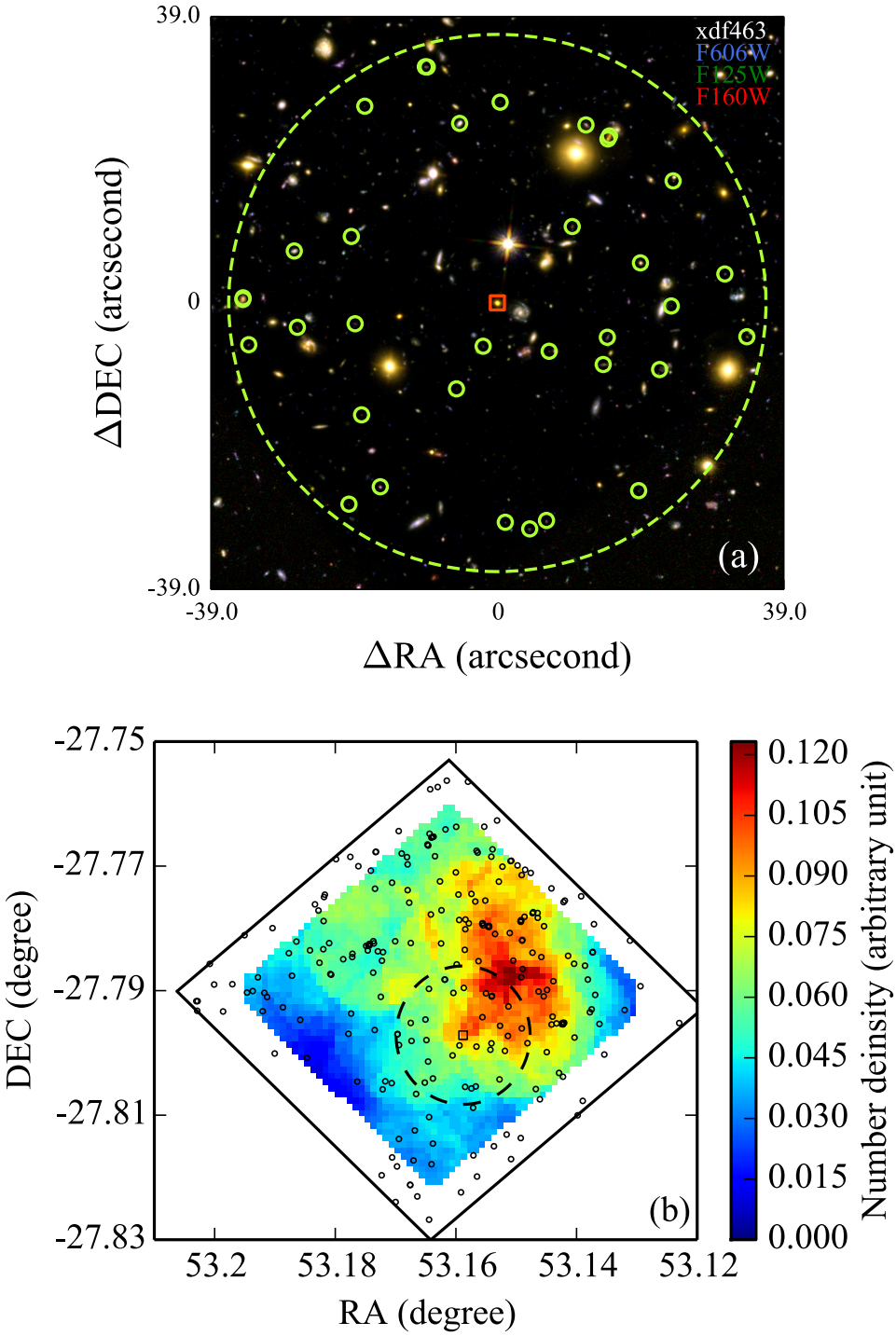

(a) RGB composite image (*HST*/F606W blue, F125W green, and F160W red) of XDF463 (a red square) and 34 satellite galaxies (green circles) within the virial radius, $r_{\rm vir} \sim 300$ kpc (large dashed circle). (b) Contour map of the number density of galaxies at the same redshift (black circles) as XDF463 ($z \sim 1.923$; black square) in the XDF field (large rectangle). The number density is calculated for galaxies within 300 kpc at each point.

mass in a numerical simulation conducted by Oser et al. [2010]. One of their massive galaxies in Oser et al. [2010], M0209 in their Table 1, has comparable stellar mass at $z \sim 2$ with XDF463, and therefore I refer it to the simulated galaxy as a model sample in the following discussion.

To check the consistency, I compare the stellar mass growth of M209 with an abundance matching model derived in Behroozi et al. [2013]. The number density of the galaxies with similar mass of XDF463 is estimated to be $\sim 8.9 \times 10^{-4}\,\mathrm{Mpc}^{-3}$ at $z \sim 2$ in Figure 3 of Behroozi et al. [2013]. The number density of the population at $z \sim 0$ would be $\sim 6.2^{+0.2}_{-0.3} \times 10^{-4}\,\mathrm{Mpc}^{-3}$, which corresponds to the population with $M_* \sim 1.8^{+0.2}_{-0.6} \times 10^{11} M_\odot$ at $z \sim 0$. I also note that the number density is slightly higher that what we see in Chapter 3 ($n_{\rm MG} \sim 1.6 \times 10^{-4}\,\mathrm{Mpc}^{-3}$), while the expected stellar mass is comparable ($M_{*,\rm MG} \sim 1.6 \times 10^{11} M_\odot$).

4.1.4 Candidate Galaxies around XDF463

To identify the candidates for the satellite galaxies, I first run `SExtractor` in the ACS-all-combined image with a higher spatial resolution than WFC3-IR image. The high spatial resolution of the ACS (pixel scale 30 mas, FWHM $\sim 0.''11$), twice that of WFC3-IR (60 mas, $\sim 0.''18$), is helpful to deblend small objects — $\sim 6\%$ of the detected sources are blended in WFC3-IR images. The total number of the sources found within $r_{\rm vir}$ is 1369, while 324 of them are not detected in WFC3-IR image. On the contrary, 65 candidates in the WFC3-IR are not found in the ACS image. However, none of them is confirmed as the satellite of XDF463 with the criterion for satellite galaxies (see below).

By making use of the detection map by `SExtractor`, I conduct photometry on the 12-band images. Each image used here is convolved to match F160W-band by the XDF team. Since `SExtractor` is known to overestimate the sky level, due to undetected faint galaxy outskirts, I do not use the count estimated with `SExtractor`. Rather, I convolve the detection map with gaussian, and estimate the sky background with unmasked pixels.

With 12 multi-band photometry, I estimate the photometric redshift ($z_{\rm phot}$) with `EAzY`. Since galaxies with spectroscopic redshifts are biased to bright objects, I examine the redshift accuracy as follows. First, I derive the photometric redshift of each galaxy using 3D-HST imaging data, which is shallower than XDF data. The estimated accuracy of redshift is $\delta z_{\rm crit} = \langle (z_{\rm phot} - z_{\rm spec})/(1 + z_{\rm spec}) \rangle = 0.051$ for the galaxies at $1.5 < z < 2.0$ with $9.5 < \log M_*/M_\odot < 10$. The range of the stellar mass is selected in order to see the galaxies at the limiting magnitude of the 3D-HST catalog [$H_{\rm F160W} \sim 24.5$ or $\log M_* \sim 9.5$ at $z \sim 2$; van der Wel et al., 2014]. The fraction of the catastrophic redshift [$\delta z > 0.5$; as defined in Kajisawa et al., 2011a] is $\sim 14\%$.

By scaling the limiting magnitude of the 3D-HST catalog to that of the XDF data (F160W$\sim$ 29.8), I reach to the limiting stellar mass, $\log M_*/M_\odot = 7.2$. Since the redshift accuracy is supposed to be comparable at each limiting magnitude for the 3D-HST and XDF data, I set $\delta z_{\rm crit} = 0.051$ as the photometric accuracy for galaxies with $\log M_*/M_\odot > 7.2$.

It is noted that there would be some systematic errors in the photometric redshift caused by varieties of SEDs, i.e. those for massive and less massive galaxies. However, I hardly see any significant difference in the best-fit SEDs for both populations in the sample. As the present pho-

Figure 4.2: Probability distributions of photometric redshifts of XDF463 and satellites

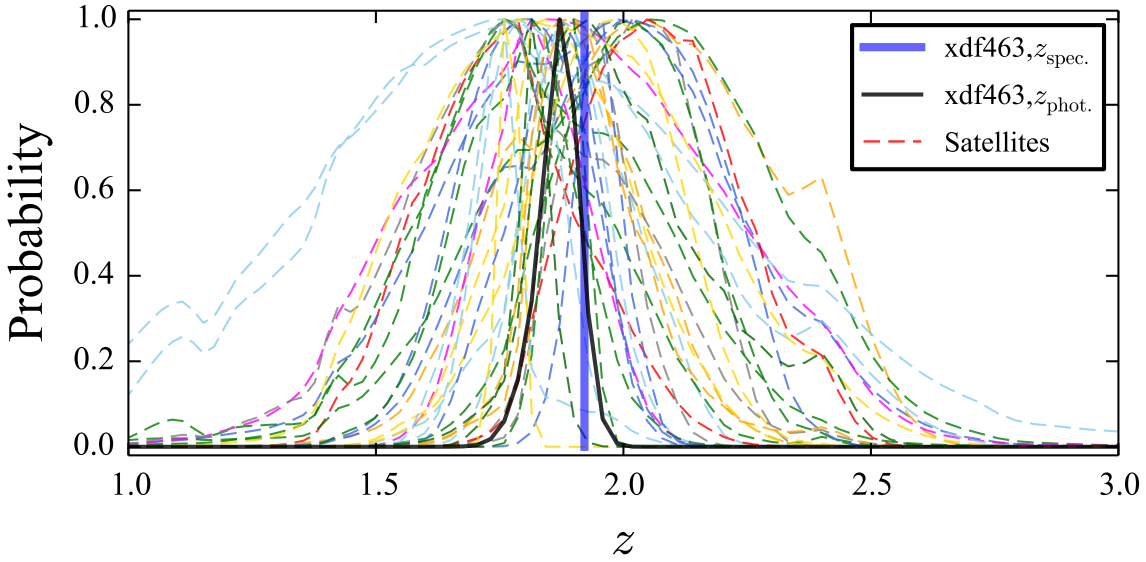

Probability distributions of photometric redshift for XDF463 (black solid line) and the satellites (colored dashed lines), derived with EAzY. Galaxies which satisfy $\delta z = (z_{\rm host} - z_{\rm phot})/(1+z_{\rm host}) < \delta z_{\rm crit} = 0.11$ are selected as the satellite galaxies of XDF463 at $z_{\rm host} = 1.9213$. The spectroscopic redshift of XDF463 is shown with a blue vertical bar.

tometric accuracy is high enough for SED fitting, the photo-z of our sample with low mass is well determined at $z \sim 2$ [e.g., Kajisawa et al., 2011a, Bezanson et al., 2015].

4.1.5 Satellite Galaxies of XDF463

I select galaxies which satisfies $\delta z = (z_{\rm host} - z_{\rm phot})/(1+z_{\rm host}) < \delta z_{\rm crit}$ as the satellite of XDF463, where $z_{\rm host} = 1.9213$ is the spectroscopic redshift of XDF463, and $\delta z = 0.11$. Since some galaxies have a large error, I further exclude the sample with $\sigma_z/(1+z_{\rm phot}) > \delta z_{\rm crit}$, where σ_z is 1σ photometric redshift error derived by EAzY. Out of 1369 candidate galaxies, I find 35 galaxies in the criteria above. One galaxy has a spectroscopic redshift, $z = 1.7672$, which is outside the redshift criteria and therefore is excluded from satellite sample. Finally, I confirm 34 satellites within $r_{\rm vir}$ of XDF463 (see Figure 4.1a). The redshift probability distributions of the satellites, as well as of the host, are shown in Figure 4.2. The SED properties of the satellites are obtained with FAST, in the same manner as done for XDF463, but fixed to the spectroscopic redshift of the host galaxy.

I note that it is still uncertain whether the satellite galaxies defined with the above criteria are gravitationally bound to the host galaxy, because of the large uncertainty in photometric redshift ($\sim 33000\,{\rm km\,s^{-1}}$), while medium-band imaging data might help to improve the accuracy (e.g., $\sim$ 6000-10000 $\rm km\,s^{-1}$; Kawinwanichakij et al. 2014).

The spatial distribution of the satellites, and the surface number density, are shown in Figures 4.1a and 4.1b. To calculate the surface number density, I count galaxies within 300 kpc at

each pixel, except for the peripheral region. I verified the number density within $r_{\rm vir}$ of XDF463 is by a factor ~ 2.3 higher than the median density in the XDF for the galaxies at the same redshift range. It is worth noting that there is no massive galaxy at the redshift around XDF463, and hence it would be reasonable to assume that all the satellite galaxies found in this study are likely to belong to XDF463. The east neighboring region, but outside $r_{\rm vir}$ of XDF463, also has the peak at $z \sim 1.9$. These galaxies could be also gravitationally bound by themselves (see discussion below).

4.2 Results

4.2.1 Expected Mass Increase by Satellite Accretion

The satellite galaxies found in this study have a wide range of stellar mass, $1.6 \times 10^7 M_\odot$ to $\sim 10^{10} M_\odot$. The total mass of 34 satellites is $\sim 4.3 \times 10^{10} M_\odot$, which is comparable to that of XDF463 — XDF463 can, at least, double the mass by the accretion of these satellite galaxies.

However, the mass growth is still in deficit to be a massive galaxy at $z \sim 0$ expected from Oser et al. [2010]'s simulation ($M_0 \sim 1.5 \times 10^{11} M_\odot$). The mass assembly history of M0209 in Oser et al. [2010] shows that $\sim 20\%$ of the total stellar mass at $z = 0$ ($M_0 \times 0.2 \sim 3 \times 10^{10} M_\odot$) is formed at $z > 2$ with in-situ mechanisms such as cold gas accretion and collapse-like star formation, while $\sim 80\%$ is formed at or outside the virial radius and accretes to the central galaxy at $z < 2$. The total stellar mass of the satellites found in this study is, however, only $\sim 30\%$ of M_0. This implies that there needs to be extra stellar mass growth from the outer region of r_{200} and/or in-situ star formation in the host and satellite galaxies, to be as massive as expected.

4.2.2 On the Star Formation of Satellite Galaxies

In Figure 4.3a, I show the star formation rate of the host and satellite galaxies as a function of stellar mass, to study the star forming properties. Most satellites found in this study are classified as star forming and form stars at the comparable rate to the main sequence of the star forming galaxies at the same redshift. This implies the possibility of mass increase by the in-situ star formation before these galaxies accrete the host galaxy. The blue rest-frame colors of the satellites in the *UVJ* diagram in Figure 4.3b also imply that they are not quenched yet even in the massive halo and can increase the stellar mass.

I first investigate the relation between stellar mass and SFR (star formation main sequence) of the satellite galaxies. In Figure 4.3a, I show the best fit slope for the satellite galaxies in the form of,

$$\log \mathrm{SFR} = a \log M_* + b, \tag{4.1}$$

where the best fit values of $a = 1.15 \pm 0.02$ and $b = -9.97 \pm 0.20$. I exclude one satellite galaxy near *UVJ* boundary from the fit, because it could be classified as quiescent within the error in Figure 4.3b. I also show two slopes by Speagle et al. [2014, hereafter S14] at $z \sim 2$ and Whitaker et al. [2014, hereafter W14] at $1.5 < z < 2.0$. The best fit slope derived in the present study

Figure 4.3: UVJ-diagram and starforming main sequence

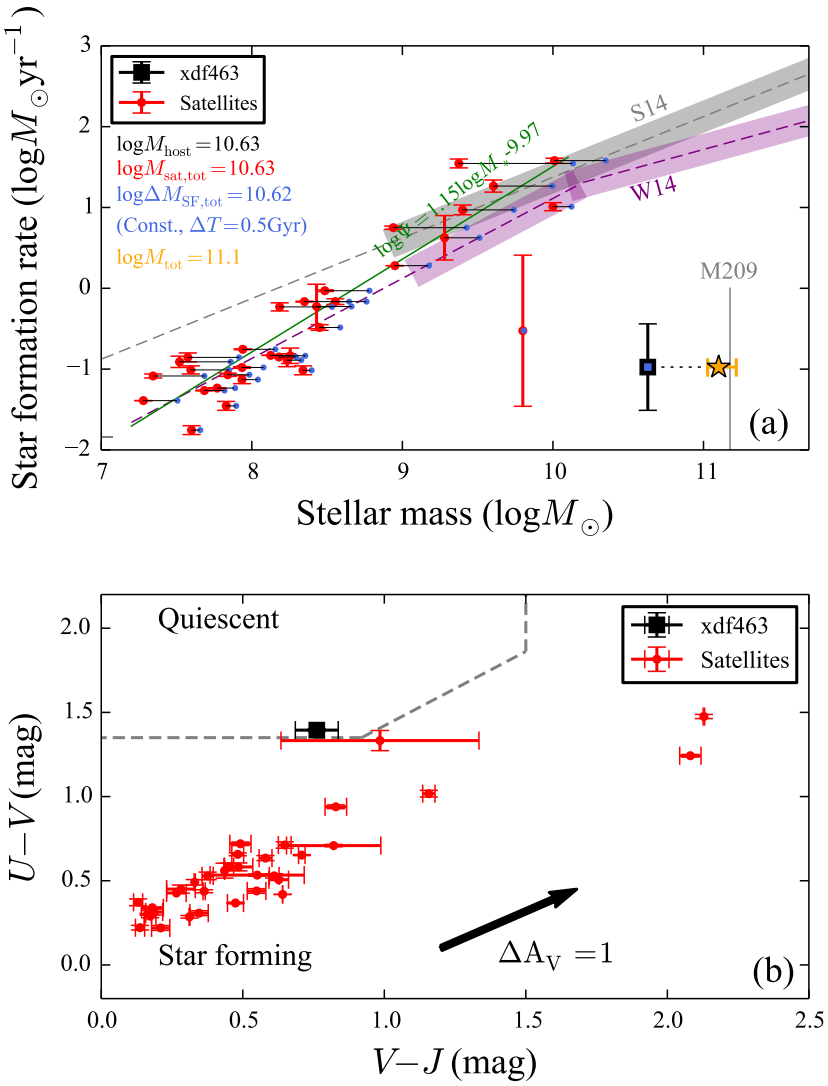

(a) Relation between the stellar mass and star formation rate (SFR) for XDF463 (black squares) and the satellites (red points), along with the main sequence of the star-forming galaxies at $z \sim 2$ by Speagle et al. [2014] (S14, gray dashed line) and at $1.5 < z < 2$ by Whitaker et al. [2014] (W14; magenta dashed line), and our best-fit slope, $\log \mathrm{SFR}/M_\odot \mathrm{yr}^{-1} = 0.99 \log M_*/M_\odot - 8.44$ (green solid line), with typical uncertainties (~ 0.2 dex). The expected stellar mass for each galaxy, by assuming a constant SFR of $\Delta T = 0.5$ Gyr, is shown with a smaller blue point. The total mass, if all satellites form stars for $\Delta T = 0.5$ Gyr and accrete to XDF463, comes to an orange asterisk symbol. The horizontal error bar of the asterisk accounts for the uncertainty of ΔT, where I set to 0.3 Gyr and 1.0 Gyr (see also the main text and Figure 4.4). (b) XDF463 (black squares) and the satellites (red points) in the rest-frame UVJ color diagram, where the quenched galaxies reside in the upper left region enclosed with dashed lines and star-forming in the other region. The error in the colors for each galaxy is estimated by the two different star formation histories. The uncertainty in the dust attenuation of $\Delta A_V = 1.0$ mag is shown with an arrow.

is much steeper than those in the previous studies ($a \sim 0.6$). Although W14 suggests a steeper slope ($a = 1.04 \pm 0.05$) at lower mass range ($\log M_*/M_\odot < 10.2$), the inconsistency could not be explained within the uncertainties in SFR and stellar mass[2]. This can be because of the low-mass population with $\log M_*/M_\odot \lesssim 8$, which is not included in the previous studies. Interestingly, the main sequence slope would be much milder ($a = 0.71 \pm 0.09$) if derived only for more massive galaxies ($\log M_*/M_\odot > 8.8$), which is in good agreement with S14 ($a = 0.75 \pm 0.03$), suggesting a possible knee at lower mass than that suggested in W14 ($\log M_*/M_\odot \sim 9$). However, it is also possible that these low mass satellites are affected by the environmental effect in the massive halo of XDF463 and lowered the observed SFRs.

From the observed SFR, I then estimate the stellar mass increase due to the in-situ star formation for each satellite. For this exercise, I assume that the star formation last over $\Delta T = 0.5$ Gyr at the same rate and mass return fraction of $R = 0.36$, i.e. $\Delta M_{\rm SF} = SFR \times (1-R) \times \Delta T$ [e.g., Leja et al., 2015]. The return fraction is calculated by `GALAXEV` assuming the Chabrier [2003] IMF. The expected increase of stellar mass for each satellite is shown with blue points in Figure 4.3a. The total stellar mass made by the in-situ star formation of the satellites would be $\sim 4.3 \times 10^{10} M_\odot$, comparable to the total *present* stellar mass of in the satellites. By accounting for the mass growth by the in-situ star formation, I find the total mass of the accreting satellites and XDF463 would be $\sim 1.3 \times 10^{11} M_\odot$, $\sim 83\%$ of M_0, as shown in Figure 4.3a.

The duration of the star formation, ΔT, is uncertain because of complex physics during merging events. As such, I also show the mass growth estimated with $\Delta T = 0.3$ Gyr (which results in 71% of M_0) and 1.0 Gyr (110%). The derived lower and upper values are shown as error bars in Figure 4.3a.

The merger time scale estimated with the numerical calculation is typically $\sim$ 1.0-1.5 Gyr for a satellite at $\sim$ 100 kpc [Lotz et al., 2011], or even longer for lower mass (see below), and I here set $\Delta T = 1.0$ Gyr as the maximum time duration of the star formation. In Figure 4.3a, I show the mass growth of XDF463 with a constant SFR, while during the merger event it could significantly vary.

It is noted that the accretion of satellites with gas (wet merger), on the contrary, would suppress the size growth [Naab et al., 2009, Hopkins et al., 2009a], while some studies claim the necessity of wetness ($\sim 4\%$ of gas to the total stellar mass; Sonnenfeld et al. 2014) in the context of the halo mass profile (i.e. core profile in the cener).

While these uncertainties are not trivial, I would stress here that the in-situ star formation of satellites would increase the stellar mass in the accreting phase, which would explain the significant mass growth at the outer envelope and supplement the deficit of the accreting component. It is worth noting that the main sequence slope for ΔM-evolved galaxies (blue points in Figure 4.3a) would become much milder than the current slope and become consistent with the previous results, which supports an assumption of the constant star formation during ΔT (see below).

2. While SFRs derived through SED fitting can vary with different star formation histories, those derived from nebular lines, e.g., Hα, are suffered from dust extinction.

4.3 Discussion

The mass growth of XDF463 is found to be in deficit when only considering the *present* satellite galaxies. However, the satellite galaxies are also found to be forming star from both SED-based star formation rate and UVJ diagram, which can compensate the deficit to the model expectation. With the expected mass growth estimated in previous sections, I discuss possible fates of XDF463.

4.3.1 Stellar Mass-Size Relation

I show the stellar mass-size diagram of XDF463 and its satellites in Figure 4.4a, along with that of the local early-type galaxies studied in Poggianti et al. [2013]. I convert the stellar mass in Poggianti et al. [2013] from Kroupa [2001] IMF to one with Chabrier, by using the relation in Cimatti et al. [2008]. The expected size growths in minor merger scenario ($\Delta r \propto \Delta M^2$) and major merger scenario with $\Delta r \propto \Delta M$ are shown with arrows. As is seen, the minor merger scenario is more preferable scenario, given XDF463 would be on the local relation. However, the significant size growth would be expected through merging with "quenched" satellites (dry minor merger), contrary to the finding in this study. Because of the complex dissipative process, it would not be straightforward if merging with star forming satellites (wet merger). In what follows, I investigate three simple scenarios for XDF463, focusing on the satellite properties. The expected mass and size growth of XDF463 should be within the scope of these three cases.

I first investigate the size growth via purely dry minor merger (Case A), neglecting the in-situ star formation of the satellite galaxies, but only considering the stellar dynamics, as is done in previous studies. The gas in the satellites is quickly exhausted or tidally stripped (e.g., environmental quenching; see also Section 4.3.3), and then the satellites accrete to the outer envelope of the host galaxy in due time. In this scenario the size of the host galaxy evolves as $\Delta r \propto \Delta M^2$ (A in Figure 4.4a). Considering the mass and size evolution in Figure 4.4a, I expect that the compact galaxy ends in the population of local compact galaxies. Although this scenario seems somehow "failure" given the discussion so far, this scenario, in fact, is plausible. For example, Poggianti et al. [2013] found that compact galaxies reside in relatively dense environments, rather than normal fields [e.g., Taylor et al., 2010].

It should be reminded of a dense region at the north-east of XDF463 found in Figure 4.1b. It is possible that some galaxies outside the virial radius of XDF463 would fall and then increase the mass and size, which would be possible to bring the compact galaxy on the local size-mass relation.

When counting the in-situ star formation of the satellites, the situation is changed. As suggested in Section 4.2.2, I take account for the mass growth of the satellites and assume that they would stop star formation activity before merging to the host (Case B). In this scenario, I expect the size growth with $\Delta r \propto \Delta M^2$, as well as Case A. Since stellar mass growth is much larger, the size growth is accordingly more significant than one in Case A, to be consistently on the local relation in Figure 4.4a.

It is possible that satellites continue star formation activity until they merge to the host, in which

Figure 4.4: Size-mass distribution of XDF463

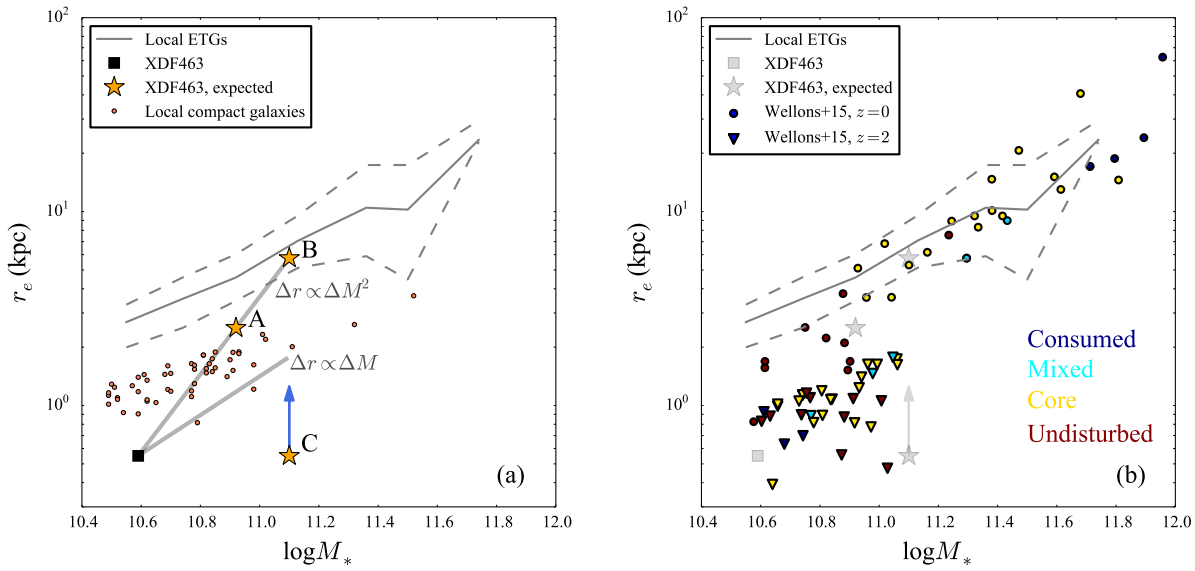

(a) Observed and expected size-stellar mass relation for XDF463 (black squares and yellow stars, respectively). The relation for the local early-type galaxies from Poggianti et al. [2013] is shown (gray solid lines) with 1σ error (dashed lines). Three predictions are shown, based on different assumptions that satellite (A) quench very soon and accrete to the outer envelope of the host, (B) continue in situ star formation and then quench before they accrete, or (C) continue forming stars until they induce wet mergers. Compact galaxies in the local universe [Poggianti et al., 2013] are shown with red circles, to suggest that non-evolution of the compact galaxies is also a case. The evolutions via major ($\Delta r \propto \Delta M$) and minor ($\Delta r \propto \Delta M^2$) mergers expected by assuming the virial theorem [e.g., Hopkins et al., 2009a] are shown with arrows. **(b)** Compact galaxies at $z = 2$ (inverted triangles) and their progenitors at $z = 0$ (circles) in the Illustris simulation [Wellons et al., 2016] are shown. Each data point is color-coded by 4 evolution paths, Consumed, Mixed, Core, and Undisturbed (see the main text). It is noted that the Illustris data are arbitrarily shifted for the comparison with our observed and expected values for XDF463 (shown with gray square and stars).

case the merger would be dissipative (Case C). However, it would be more difficult to predict the size evolution in this case, because of the complicated physical mechanisms after merging. The host galaxy can significantly change its morphology to, e.g., the late-type galaxy with much larger scale radius, or, on the opposite case, keep to be compact through the wet compaction [e.g., Dekel and Burkert, 2014]. As such, I show the expected mass but not size in Figure 4.4a.

It is also worth mentioning that if XDF463 experiences merger with the largest gas-rich satellites, it could end up with one of the local compact galaxies, by following $\Delta r \propto \Delta M$. Since major merger typically involves dissipative process and hence lose the angular momentum, the compact stellar system is another possible fate [e.g., Wuyts et al., 2010].

4.3.2 Size Growth Expected in Simulation

More specific discussion is available in numerical simulations. In Figure 4.4b, I show compact galaxies at $z = 2$ and their descendants at $z = 0$ calculated in the Illustris simulation [Wellons et al., 2016]. Since the compact galaxies in their study are more massive ($\log M_*/M_\odot > 11$) than the mass of the present study, I focus on discussing the relative evolution, rather than the specific position on the mass-size relation. I note that their 3-dimensional effective radius is converted to the projected 2-dimensional one by multiplying 0.75 for the fair comparison.

In Wellons et al. [2016], they classified the descendants of the compact galaxies as follows: Consumed (absorbed by more massive galaxies), Mixed (major merger), Core (minor merger, which keeps the compact galaxy in the core), and Undisturbed (newly formed and accreted mass is $< 10\%$ of $z \sim 2$ galaxies). It is noted the size growth is also observed in the Undisturbed class, where mass loss and adiabatic expansion contribute to $\sim 15\%$ size increase, as well as an artificial numerical effect of $\sim 15\%$ increase [Wellons et al., 2016]. As mentioned above, minor merger is thought to increase the galaxy size more efficiently compared to major merger. However, some of the satellites involved in minor merger might have gas, which I could not identify only with the data provided in Wellons et al. [2016].

By comparing with their data, the evolution paths of XDF463 expected in two of three cases are all assured to be possible — Case A is observed as core and undisturbed, and Case B as core. Interestingly, in their simulation there is no galaxy to decreases the size through interaction events, even though some of them have experienced wet merger. As such, I can safely set the lower limit for the size of XDF463 in Case B of Figure 4.4b.

4.3.3 Quenching the Satellite Galaxies

I have estimated the mass growth due to the in-situ star formation of the satellites with a simple assumption: star formation of each satellite is kept at constant rate for ΔT. Although the assumption is reasonable for galaxies in the field environment [Genzel et al., 2010, Kennicutt and Evans, 2012], it is not clear for the satellites in the massive halo of XDF463, where environmental effects are expected to shut out the on-going star formation [Peng et al., 2010, Koyama et al., 2014, Morishita et al., 2017].

One indicator known as a good indicator of the environmental effect is the distance from the mass center. I find, however, no significant dependence of the SFR nor UVJ colors of the satellites on the distance from the center i.e. no clear evidence of environmental quenching. While Wetzel et al. [2013] found satellite galaxies continue forming stars for a few Gyr after infalling within $r_{\rm vir}$ of their host galaxy, most of the satellites found in this study reside at $r > 100\,$kpc. Considering that I have few satellites close to the host galaxy (2 galaxies at $r_{\rm proj.} < 100\,$kpc), it is likely that we are witnessing satellites right after their infall into $r_{\rm vir}$. The result of the blue rest-frame colors of the satellites in Figure 4.3b would also support that these satellites are still young.

It should be recalled that the local elliptical galaxies are known to have flat age gradients, $< 1\,$Gyr difference between inner and outer radii, but rather have metallicity gradients [e.g., Tamura et al., 2000]. Given that the compact galaxy would be a typical local elliptical galaxy, this suggests that these satellites have to stop forming stars in a short time scale, $< 1\,$Gyr, so as to have a similar age to the host and less metal-enriched population. In a case that satellites would continue forming star for $> 1\,$Gyr (Case B), the host galaxy would have an age gradient, in contradiction with the local ellipticals.

4.3.4 Expecting the fate of XDF463

I have investigated the mass increase of XDF463, with the accreting satellites taking account of their in-situ star formation. Given the distance from the host, these satellites would merge in $\sim$ 1-3 Gyr, except for the smallest satellites ($< 1/100$ of the host galaxy), whose accretion time would exceed the Hubble time [Lotz et al., 2011, Wetzel et al., 2013, Tal et al., 2014]. In other words, the compact galaxy observed at $z \sim 2$ would be settled as the local analogous at $z \sim 1$, as shown in many other studies of massive galaxies [Bundy et al., 2009]. This is also consistent with recent studies on the evolution of the number density of compact galaxies [e.g., van Dokkum et al., 2015]. In Figure 4.5, I summarize the present study.

An interesting question yet to be answered is — After all satellites merge to the host galaxy, does not any merger happen? This seems not to be true; some previous studies show, by counting the pair fraction, that the merger rate of massive galaxies is not still negligible at $z < 1$ [$\sim 20\%$ Bluck et al., 2012, Newman et al., 2012]. While I have investigated satellites within $r_{\rm vir}$ of XDF463, it is likely that galaxies would fall into $r_{\rm vir}$ at the later epoch from the outer radius [e.g., Tal et al., 2014]. Furthermore, satellite galaxies typically have eccentric orbit [van den Bosch et al., 1999, Hayashi and Chiba, 2014], and avoid being detected within the projected $r_{\rm vir}$ at the observed redshift. To cover such candidates, kinematic information in the entire field would be helpful.

As noted before, I have found a peak of the number density of galaxies at $z \sim 1.9$ in the neighboring region at $r > r_{\rm vir}$ (but $\sim 400\,$kpc; Figure 4.1b), whose redshift distributions are similar to those of XDF463. Although I find no massive galaxy comparable to XDF463 in the neighboring region, galaxies therein may be trapped by the host halo of XDF463 in the near future.

I note some caveats on the finding that most satellite galaxies are star forming and reside at $r > 100\,$kpc from the compact galaxy. The finding is not consistent with the results of previous studies in some aspects. For example, Newman et al. [2012] searched satellite galaxies in $10 <$

Figure 4.5: Summary figure of the fate of XDF463

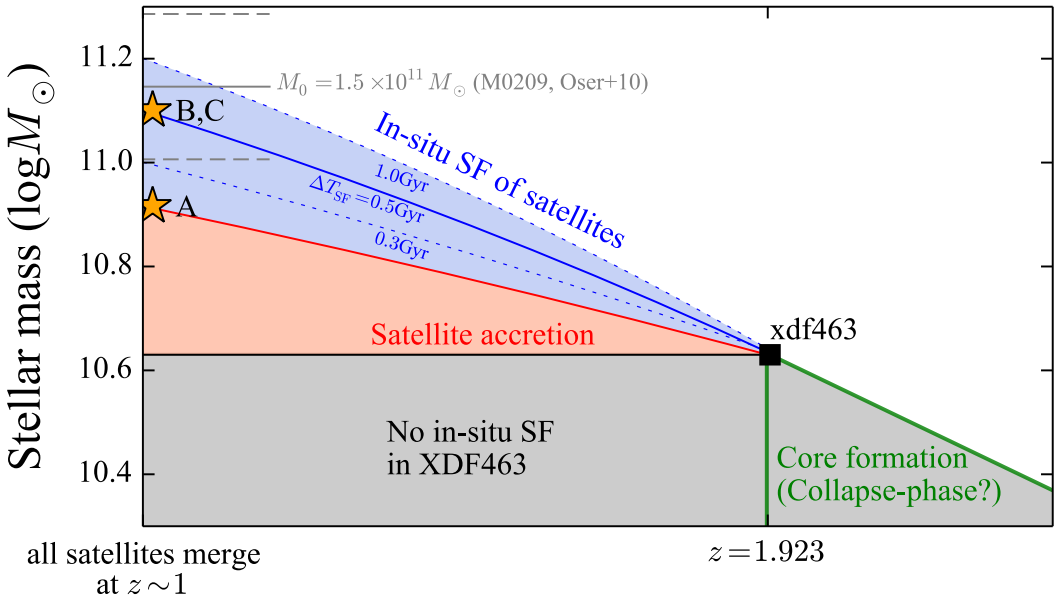

Summary figure of the expected growth of stellar mass as a function of redshift, taken from Morishita and Ichikawa [2016]. The compact galaxy, XDF463, has $\sim 23\%$ of the stellar mass expected at $z = 0$, $M_0 = 1.5 \times 10^{11} M_\odot$ (M0209 in Oser et al. 2010; horizontal gray solid line with uncertainties as dashed lines) at the observed redshift. The satellites found in this study account for $\sim 26\%$ of M_0. The in situ star formation of the satellites is assumed with $\Delta T = 0.5$ Gyr (blue solid line), which accounts for $\sim 28\%$ of M_0, and the net mass increase by the satellites would be $\sim 54\%$ of M_0 if all of them are merged in typical dynamical time (~ 1 Gyr). The contribution of the in situ star formation of the satellites with different time duration ($\Delta T = 0.3$ Gyr and 1.0 Gyr) is also shown with dotted blue lines.

$r/\mathrm{kpc} < 30$ around massive quiescent galaxies at $z \sim 2$, and found that $\sim 38\%$ of the satellites are quiescent, though their sample is a mixture of compact and normal quiescent galaxies. I recall two problems to be elucidated — the completeness of the low mass quiescent galaxies and the photometric redshift uncertainty.

Firstly, I clarify the detection limit for low mass quiescent satellites. Since quiescent galaxies are more difficult to detect than star forming galaxies with the same stellar mass, the detection bias should be properly examined. As described in Section 4.2, I set the stellar mass limit by scaling that of van der Wel et al. [2014] (for quiescent galaxies) to the detection limit of XDF data, i.e. $\log M_*/M_\odot > 7.2$. Since I have no quiescent satellite even in more massive stellar mass range, shifting the mass limit does not change the fraction of quiescent satellite. Furthermore, I investigate the satellite galaxies around massive quiescent galaxies ($\log M_*/M_\odot > 10.6$), but not compact, at $1 < z < 2.5$ in the XDF, in the same manner as for XDF463. I find that $\sim 50\%$ of the satellites are quiescent if the same mass limit as Newman et al. [2012] ($\log M_*/M_\odot > 9.5$) is applied.

Even though retrieving spectroscopic redshifts for all the satellites, and especially for low-mass ones, seems unrealistic with the current and future facilities, narrow-band imaging can partly mitigate the uncertainty in the redshift measurement [see for example, Hayashi et al., 2012, Koyama et al., 2014]. For example, by deeply imaging the narrow range of wavelength which corresponds to a strong emission line, such as Hα of star forming satellites, we can precisely determine the redshift. While this method is only effective to star-forming galaxies, given the finding of this study we can improve the investigation for more compact galaxies.

I investigate the possibility that quiescent galaxies are mistakenly excluded due to the redshift error. As an extreme test, I fix the redshift of *all the detected candidates* within $r < 300\,\mathrm{kpc}$ to the same redshift of the host ($z = 1.92$), and derive SED parameters and the rest-frame colors of candidates by using the derived SED templates. Intriguingly, I find no quiescent galaxies among them, strongly supporting our finding that most satellites around the compact galaxy are blue star forming galaxies.

I therefore conclude that XDF463 has some extraordinary nature apart from non-compact massive quiescent galaxies at similar redshifts — surrounded by starforming satellites at distances $\gtrsim 100\,\mathrm{kpc}$. The finding would give an important clue to the formation and fate of compact galaxies, which I further investigate in Chapter 5.

4.4 Summary

In this chapter, I investigate the latter epoch of the "two-phase" scenario, the accretion phase, by searching the accreting satellites within the virial radius of one compact galaxy, XDF463. Although this "case" study cannot be generalized to all compact galaxies observed at $z > 1$ or massive local galaxies, the detailed study of the host and surrounding environment has provided a lot of insight.

Previous studies have challenged the scenario in similar ways, resulting in difficulty to explain

the total mass increase only with the *present* satellites found in the near-infrared imaging. I made use of the extremely deep imaging data ($m_{\rm ACS} \sim 30.6$ ABmag) taken with *HST*/ACS, which enabled us to find more faint satellites. For the photometrically confirmed 34 satellite galaxies out of 1369 candidates within $r_{\rm vir}$, I derived their SED properties, i.e. SFR and stellar mass, finding that most of them are classified as star forming in the *UVJ* diagram. However, low-mass satellites are significantly below the star formation main sequence from the literature, resulting in a steeper slope of $\log {\rm SFR} = 1.15 \log M_*/M_\odot - 9.97$ (Figure 4.3a).

By assuming all the satellites would merge in ~ 0.5 Gyr, while keeping in-situ star formation (B in Figure 4.4a) the estimated mass increase due to the accretion and in-situ star formation would be $\sim 8.3 \times 10^{10} M_\odot$, which is roughly consistent with the expectation of the observations and simulations within uncertainties. However, I could not give a definitive conclusion how much the size of the compact galaxy would increase, because of lack for the satellite properties, which could also lead to the other evolution paths (A and C in Figure 4.4a). Since there are many compact galaxies found in the local universe, I stress that the significant size evolution to a local early-type galaxy is not the only fate of XDF463. Although the uncertainties in the duration of the star formation, merging time scale of the satellites, and photometric redshift affect the estimate, the contribution of the in-situ star formation of the *satellites*, which has been ignored in previous studies, would mitigate the known difficulty on the significant size and mass evolution of compact galaxies.

CHAPTER 5
[PART2] THE FATE OF MASSIVE BULGES

Brief summary

One of the most interesting findings from the previous chapters is that massive galaxy progenitors, which are expected to be $\log M_*/M_\odot > 11$ at $z \sim 0$, have already formed massive stellar component ($\log M_*/M_\odot \sim 10.7$) at $z \sim 2$. These massive galaxies are expected to evolve to the local early type galaxies through a number of dry minor mergers.

The expected evolution path is, on the other hand, largely based on some uncertain assumptions, such as small gas fraction of merging satellites and the total number of merging event. While the detailed study of one galaxy in Chapter 4 gave me an idea of possible paths of compact galaxies qualitatively, it could not reach any definitive conclusion. Quantitative questions, like, **"What is the fraction of local massive galaxies which have gone through the dry merger scenario?"**, are yet to be answered.

According to the fact that there is a strong connection between bulge formation and quiescence, and also that bulges in massive galaxies can be the relic of compact galaxies, in this last chapter I study the diversity in galaxies and their evolution by focusing on galaxies with massive bulge. The idea is as follows.

Firstly, I see the bulge fraction (i.e. bulge-to-total ratio, B/T) of the massive galaxy progenitors selected in the previous chapter. As I have seen in Section 3.4.4, galaxies at each redshift bin still have diversity in their properties. And, as expected, I show that the derived B/T has a huge scatter, which is partly caused by the moderate imaging depth of CANDELS [Grogin et al., 2011, Koekemoer et al., 2011].

Accordingly, after the first section, I limit myself to use deeper imaging data taken in XDF and Hubble Frontier Fields (HFF) to reliably measure B/Ts. In Section 5.2, I select sample galaxies at a constant bulge mass of $\log M_*/M_\odot \sim 10.8$. This mass is motivated by the average picture of MGs in Chapter 3, where bulges form first and then the mass accumulation occurs in the outer part at $z < 2$.

I quantitatively confirm that the evolution of massive galaxies after their massive bulge formation is divergent in the following ways;

1. A large fraction of massive bulge galaxies (26/37) have some features of merger and/or interaction, as expected in the two-phase scenario.

2. While these galaxies keep their bulges unchanged even with interactions, about a half of interacting galaxies resume star formation and are classified as starforming galaxies in the UVJ-diagram, which implies that *not all* minor mergers are dry.

3. Passive galaxies, even with ongoing interaction, mostly follow $\Delta r_e \propto \Delta M^2$, while starforming galaxies with companions follow or reside under $\Delta r_e \propto \Delta M$.

The assumption I have in this chapter is that the minor merging does not destroy the central bulge, so that I can trace the descendants of compact galaxies at a fixed bulge mass. While this could exclude some compact galaxies which are destroyed and become other types of galaxies (e.g., disk dominated galaxies), these galaxies are out of focus in this thesis. Another concern is that there are possibly massive bulge galaxies whose progenitors are not compact galaxies. I will discuss alternative scenarios of massive bulge galaxies supplementally.

5.1 Bulge-to-Total Ratio of Massive Galaxy Progenitors is Highly Divergent

In Figure 5.1, I show the bulge-to-total ratio (B/T) of massive galaxy progenitors (MGs), selected and studied in Chapter 3. The bulge-to-total ratio is derived from *HST* F160W imaging data (see the following section for the detailed method). The derived ratio for MGs is highly divergent and no clear trend along redshift is seen, against the assumption that these galaxies are selected at a constant number density and become "a" typical massive galaxy. Rather, what we are seeing here is consistent with what we saw in Section 3.4.4, that there is divergence in structural properties of galaxies at a given stellar mass. The average properties and evolution derived in Chapter 3 is, rather, a mixture of galaxies with different structural properties, such as B/T.

It is noted that the B/T of MGs is derived with CANDELS F160W imaging, whose limiting magnitude is ~ 24 mag [van der Wel et al., 2014]. Although the target galaxies here are quite massive and therefore bright, their *total* magnitude is comparable to the limiting magnitude in the highest redshift bin. In this case, the bulge/disk decomposition is often suffered from unexpected noise and the result could be wrong. Furthermore, faint companion around/interacting with the target galaxies, which are important to investigate their evolution path, can be easily missed in moderate depth imaging, as demonstrated in Figure 5.2. As such, in the following sections I make use of much deeper imaging data, ~ 29 mag, recently taken in XDF and HFF.

5.2 Data and Results

5.2.1 XDF+HFF Parallel Field Imaging

I make use of deep *HST* imaging data taken through XDF [Illingworth et al., 2013] and HFF [Lotz et al., 2017]. The XDF data is reduced in the same manner as explained in Chapter 4.

From the HFF data, I only use those in parallel pointings, which offset for ~ 4 arcmin away from cluster centers. While the depth of both pointings are similar ($m_{F160W} \sim 29$ mag), the central pointing has a merit of gravitational lensing effect by the massive clusters behind ($z \sim 0.5$). Lensing effect magnifies the source flux by a factor of ~ 2 to $\gtrsim 100$, which provides higher signal-to-noise ratios of high-z galaxies. However, such a strong magnification distorts the galaxy morphology, and the derived B/T ratio would be less meaningful. As such, I only use the parallel pointings, where magnification effect is much smaller ($\mu < 2$). Since I focus on massive galaxies, and the imaging is quite deep, magnification support is not necessary in this study.

Figure 5.1: Bulge-to-total mass ratio of massive galaxy progenitors

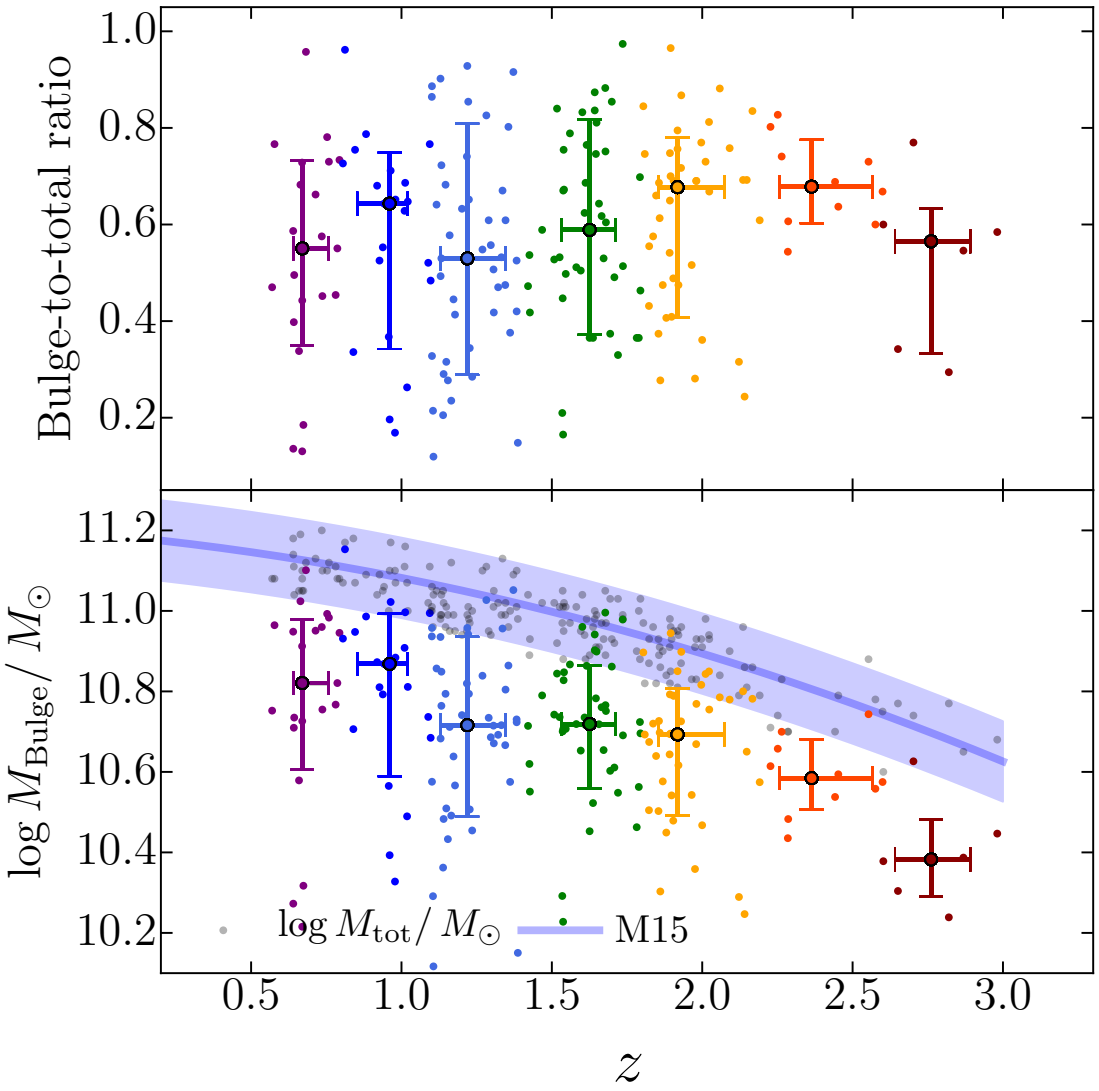

Top: Bulge-to-total ratio (B/T) of galaxies selected as massive galaxy progenitors (Section 3), as a function of redshift (colored circles). Only successful results are shown here. While a monotonic trend is expected from Section 3, a large scatter is observed in the derived B/T, which implies that **the abundance matching does not give any single population, but rather a mixture of different types of galaxies.** *Bottom:* Stellar mass in bulge for the same galaxies (colored circles). The total mass of the galaxies are also shown (gray circles), along with the constant number density (blue hatched region). While the average bulge mass is similar to what has been implied in Chapter 3 ($\log M_{*,\rm bulge} \sim 10.8$), a large scatter is observed. The observed scatter can be attributed to 1. deficiency of S/N of shallow imaging, and/or 2. intrinsic scatter, i.e. the fact that *all galaxies do not follow the average evolution* derived in Chapter 3.

Figure 5.2: Comparison of imaging depth of CANDELS and XDF

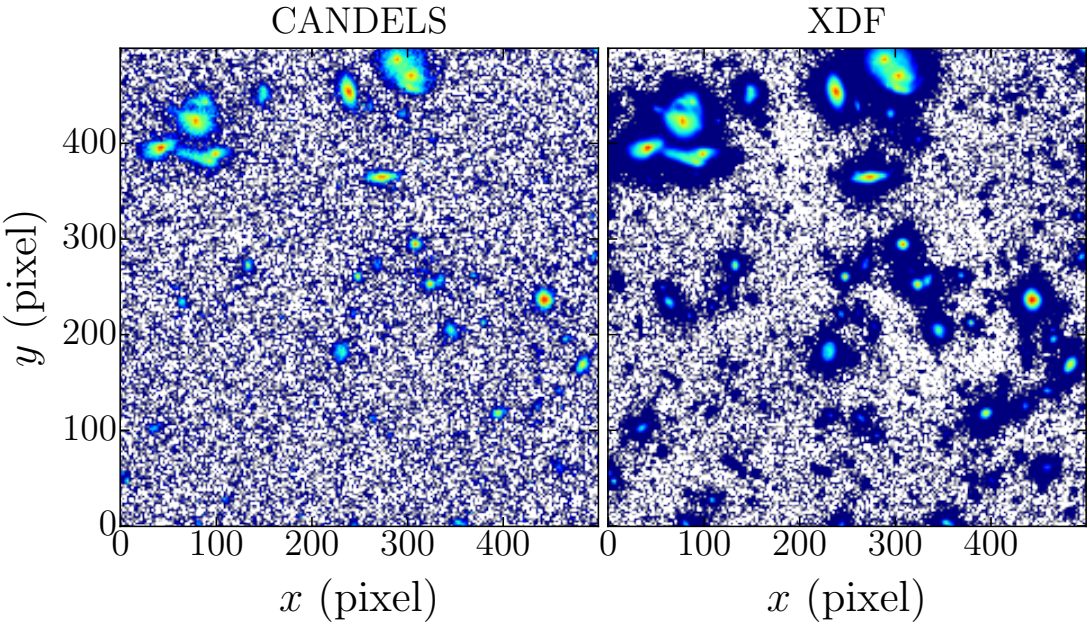

Imaging examples from CANDELS (left) and XDF (right), whose limiting magnitude is $m_{\mathrm{F160W}} \sim$ 24 mag and 29 mag, respectively. As is obvious, the XDF imaging captures more details of galaxies, such as outer faint envelope and surrounding objects, compared to the CANDELS, which securely provides the reliable structural measurement.

For HFF galaxies, I derive the photometric redshift with 7-filter band (F435/ 606/ 814/ 105/ 125/ 140/ 160W) by using `EAzY` code, and SED parameters by `FAST`. The only modification from Chapter 4 is the IMF - I assume Salpeter [1955] IMF for both XDF and HFF galaxies. The total area of 7 FoVs is $\sim 28\,\mathrm{arcmin}^2$.

5.2.2 Selecting Galaxies with Massive Bulges

I derive the bulge-to-total ratio by fitting galaxy light profile in F160W-band with `GALFIT`, in a similar manner as in previous chapters. Sérsic profiles with $n = 4$ for bulge and $n = 1$ for disk components are fixed while fitting. Galaxies with unphysical parameters are excluded as failure fitting. I also exclude galaxies with axis ratio, $q \equiv b/a < 0.3$ for the bulge component, which is a reasonable assumption as there is no "edge-on" bulge.

The bulge mass of each galaxy is obtained by multiplying B/T to the total stellar mass. Since galaxy SEDs are obtained by using colors in the central $0.''7$ aperture, stellar masses are possibly biased for some galaxies with strong color gradients. Morishita et al. [2015] (and Chapter 3) estimated the typical offset is $\sim 10\%$, which hardly affects the final result.

It is also noted that the structural parameters are derived by using F160W-band images, which traces the reft-frame wavelength of $\sim 1.0\,\mu$m at $z \sim 0.5$ and $\sim 0.4\,\mu$m at $z \sim 2.6$. Although there is scatter between the measurements at different bands, no trend is observed in, e.g., B/T-z space, by changing the RF-wavelength. I therefore use F160W imaging data for the consistency of the image quality.

From 344 massive galaxies of successful B/T decomposition, I select 37 galaxies with $10.6 < \log M_{*,\mathrm{bulge}} < 11$ at $z < 2.6$, with robust structural measurements ($\chi^2/\nu < 5$), where $M_{*,\mathrm{bulge}} = B/T \times M_{*,\mathrm{tot}}$. The mass range is made based on the estimate in Figure 3.4 in Chapter 3 at $z \sim 2$, where we see the massive bulge ($\log M_*/M_\odot \sim 10.8 \pm 0.2$[1]) is already formed.

It is noted that the bulge mass calculated in this way could be underestimated when there is a strong mass-to-light ratio (color) gradient. While the difference in the M/L is $\lesssim 2$ from Figure 3.6, more detailed approach would be needed to correct the effect.

The sample galaxies are plotted in Figure 5.3 and shown in Figure 5.4. The physical properties of the sample galaxies are summarized in Table 5.1. Although the total masses of the sample galaxies are roughly in agreement with the mass evolution of massive galaxies in Chapter 3 (blue hatched region), a large scatter (~ 0.2) is observed at all the redshifts. At $z \lesssim 1$, there seems that the total mass of galaxy is typically ~ 0.1 dex lower than the expected mass growth. This can be caused by later growth of the inner component (by a factor of ~ 1.6), as seen in Section 3.4.1, which increases B/T and lowers the total mass in the criterion here.

1. Stellar mass in Chapter 3 is derived with Chabrier [2003] IMF, which is systematically ~ 0.23 smaller than one with Salpeter [1955] IMF.

Figure 5.3: Bulge-to-total mass ratio of massive bulge galaxies

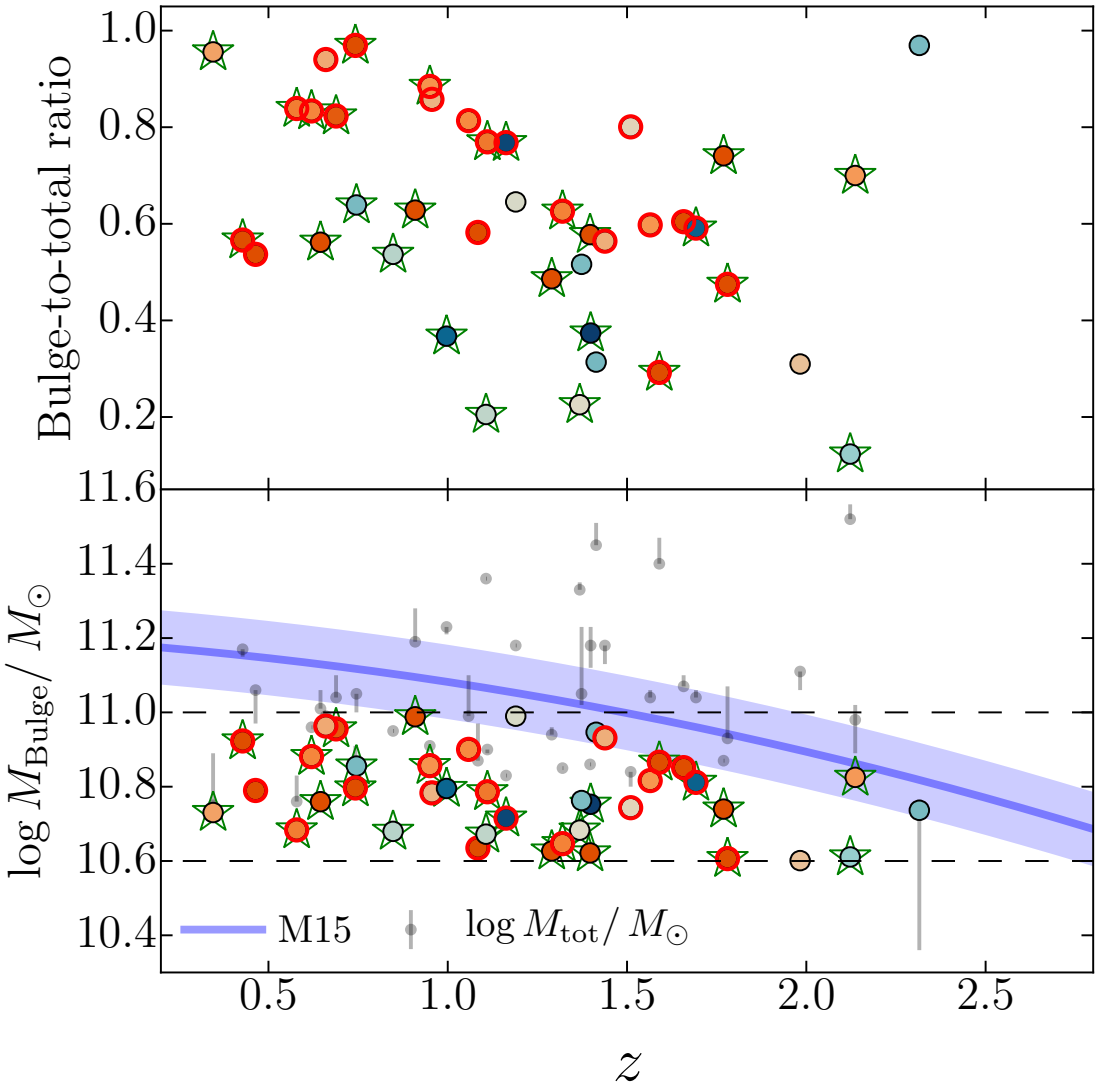

Same as Figure 5.1, but for galaxies selected at a fixed bulge mass ($\log M_{*,\rm bulge} = 10.8 \pm 0.2$; within dashed lines), color-coded by Sérsic indices (n_{tot}). Those which have merging/accretion features (Section 5.2.3) are marked with green stars, and those in the UVJ-passive region (Section 5.2.5) are marked with red circles. Some of these galaxies follow the selection criteria for massive galaxy progenitors (blue hatched region), *but not all* of the sample galaxies.

Figure 5.4: RGB stamps of massive bulge galaxies

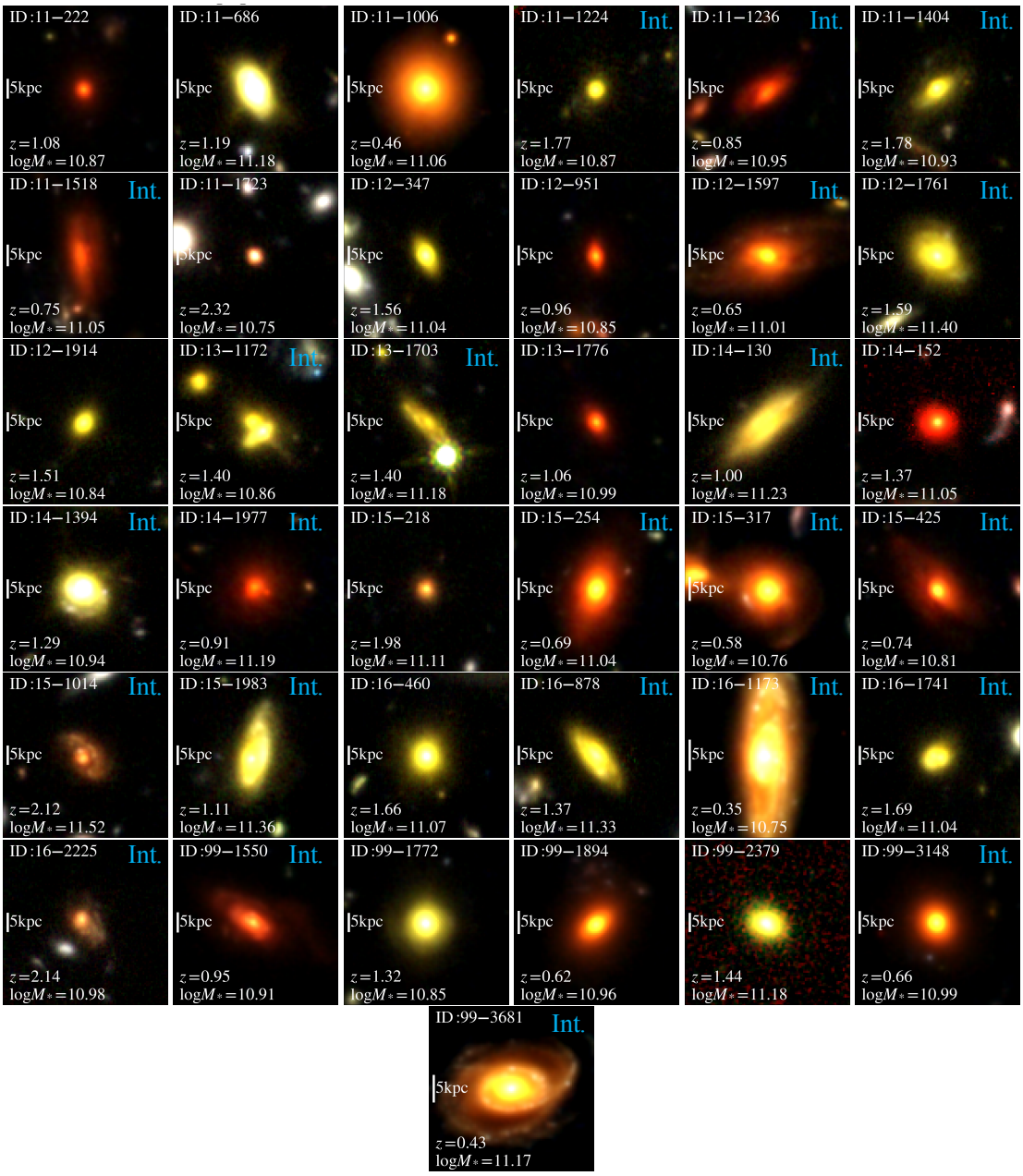

RGB postage stamps of massive bulge galaxies with $10.6 < \log M_{*,\mathrm{bulge}} < 11$. Stellar mass, redshift, and ID are shown in each stamp. Galaxies with interaction/accreting companion/merging features are flagged with "Int.".

Figure 5.5: Radial profiles of massive bulge galaxies

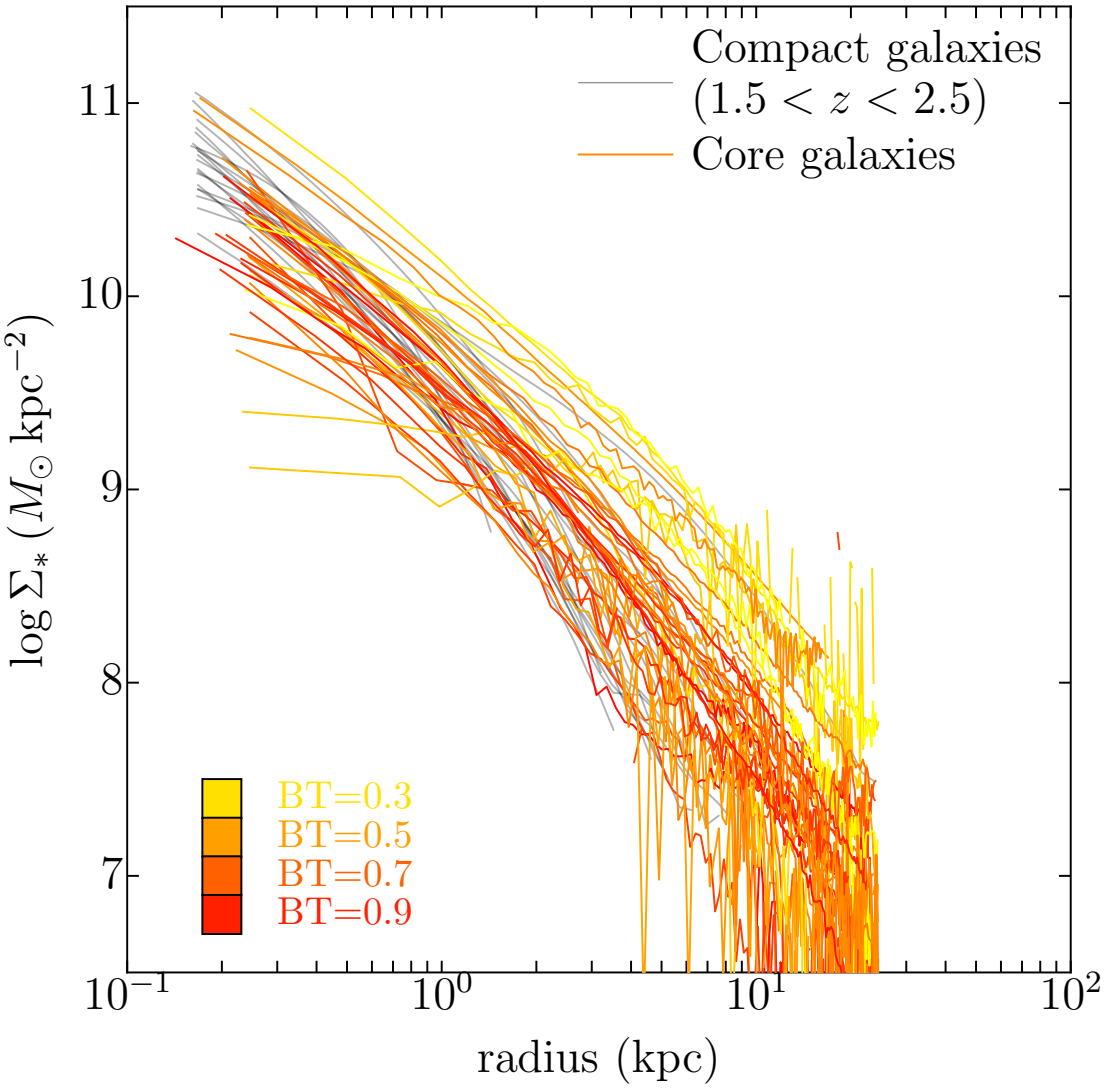

Radial stellar surface profiles of massive bulge galaxies, color coded by B/T values. Those of compact galaxies at $1.5 < z < 2.5$ [Szomoru et al., 2012] are also shown for comparison (see Figure 5.8 for cleared comparison). Slight decrease in the central surface density compared to the compact galaxies and additional stellar mass at $\gtrsim 10$ kpc are observed in those of massive bulge galaxies, which result larger effective radii ($\gtrsim 1$ kpc; see Figure 5.9).

Table 5.1: Physical Properties of Massive Bulge Galaxies

ID	z	$\log M_*$ ($\log M_\odot$)	m_{tot}[1] (mag)	r_{tot}[1] (kpc)	n_{tot}[1]	χ^2_{tot}/ν	m_{bulge}[2] (mag)	r_{bulge}[2] (kpc)	m_{disk}[2] (mag)	r_{disk}[2] (kpc)	χ^2_{bd}/ν	B/T	U-V[3] (mag)	V-J[3] (mag)	$f_{int.}$[4]
11-222	1.084	10.9	20.4	8.0	8.0	0.118	21.4	1.6	21.7	9.7	0.109	0.58	1.9	1.2	0
11-686	1.190	11.2	20.1	2.1	3.1	0.858	20.6	1.3	21.3	3.4	0.597	0.65	1.6	1.3	0
11-1006	0.464	11.1	17.7	20.6	8.0	0.187	19.0	2.6	19.2	11.4	0.145	0.54	2.2	1.3	0
11-1224	1.769	10.9	22.4	1.5	6.0	0.273	22.6	1.0	23.7	12.0	0.259	0.74	1.7	1.4	1
11-1236	0.848	10.9	20.2	4.0	2.7	0.526	21.0	2.9	21.1	4.9	0.382	0.54	2.3	1.9	1
11-1404	1.780	10.9	21.4	9.0	6.0	0.274	22.6	1.8	22.5	7.1	0.169	0.47	1.7	1.2	1
11-1518	0.745	11.1	20.3	6.3	2.1	0.224	20.7	9.1	21.3	5.3	0.190	0.64	2.1	2.1	1
11-1723	2.315	10.8	23.3	0.6	2.1	2.025	23.2	0.7	27.0	0.2	2.043	0.97	1.4	1.2	0
12-347	1.565	11.0	21.8	1.5	4.0	0.551	22.4	0.7	22.8	3.2	0.395	0.60	2.0	1.2	0
12-951	0.956	10.8	20.8	1.9	3.6	0.726	21.0	1.8	22.9	2.2	0.580	0.86	2.0	1.4	0
12-1597	0.645	11.0	18.9	7.7	8.0	0.706	19.9	1.6	20.1	8.8	0.395	0.56	2.2	1.7	1
12-1761	1.590	11.4	20.2	14.6	8.0	0.281	22.2	0.6	21.2	6.5	0.121	0.29	1.9	1.5	1
12-1914	1.510	10.8	22.1	1.7	3.3	0.288	22.4	1.5	23.9	2.1	0.250	0.80	2.0	1.5	0
13-1172	1.397	10.9	22.0	3.0	8.0	0.853	22.8	0.8	23.2	5.9	0.629	0.58	2.1	2.0	1
13-1776	1.058	11.0	20.5	2.1	4.2	0.238	20.8	1.5	22.4	4.0	0.223	0.81	1.9	1.2	0
14-130	0.997	11.2	20.9	8.5	1.2	0.231	21.9	14.4	21.3	8.6	0.154	0.37	2.2	2.2	1
14-152	1.373	11.1	21.2	1.9	2.1	0.272	21.9	1.6	22.0	2.5	0.256	0.52	2.0	1.8	0
14-1394	1.290	10.9	20.3	2.3	5.1	0.959	21.3	0.6	21.2	3.8	0.516	0.49	1.3	1.0	1
14-1977	0.909	11.2	19.4	12.7	6.8	0.124	20.3	3.2	20.9	11.4	0.099	0.63	2.2	1.6	1
15-218	1.983	11.1	23.1	2.1	3.5	0.409	24.5	0.4	23.6	2.6	0.379	0.31	2.2	1.7	0
15-254	0.689	11.0	18.9	4.7	4.8	0.639	19.2	3.0	20.9	10.2	0.531	0.82	2.1	1.2	1
15-317	0.579	10.8	18.9	4.6	4.3	0.371	19.2	3.3	21.0	8.3	0.277	0.84	2.0	1.2	1
15-425	0.742	10.8	19.3	12.0	8.0	0.301	19.9	3.7	23.6	3.9	0.476	0.97	1.9	1.4	1
15-1014	2.122	11.5	22.2	6.5	2.3	0.472	24.7	0.7	22.5	6.6	0.337	0.12	1.9	2.0	1
15-1983	1.107	11.4	20.5	7.9	2.8	0.606	22.4	1.3	21.0	7.9	0.277	0.21	1.9	2.1	1
16-460	1.658	11.1	20.9	3.7	6.6	0.896	21.7	1.1	22.1	4.9	0.823	0.60	1.6	1.1	0
16-878	1.368	11.3	20.9	5.3	3.2	0.531	22.7	0.8	21.4	5.6	0.308	0.23	2.2	1.8	1
16-1173	0.346	10.8	17.8	4.4	3.9	3.906	17.9	4.5	21.3	1.2	2.633	0.96	2.2	1.8	1
16-1741	1.692	11.0	21.9	2.3	1.2	0.872	22.4	2.3	22.8	2.1	0.496	0.59	1.7	1.1	1
16-2225	2.136	11.0	22.4	6.5	4.0	0.598	23.0	3.3	23.9	4.5	0.487	0.70	1.5	1.4	1
99-1550	0.950	10.9	19.9	6.5	4.0	1.832	20.2	5.1	22.4	7.0	1.167	0.88	1.9	1.4	1
99-1772	1.320	10.8	20.9	4.0	4.3	0.622	21.6	1.9	22.2	4.9	0.437	0.63	1.7	1.3	1
99-1894	0.620	11.0	19.7	2.5	4.2	2.594	19.8	2.2	21.5	14.8	1.809	0.83	2.0	1.3	1
99-2379	1.438	11.2	21.0	2.6	3.7	0.066	21.7	1.2	22.0	3.9	0.059	0.56	1.9	1.3	0
99-3148	0.660	11.0	19.6	1.6	3.8	1.567	19.7	1.8	22.6	0.7	1.075	0.94	2.0	1.3	0
99-3681	0.428	11.2	17.7	17.1	7.5	0.077	18.8	3.0	19.1	12.9	0.067	0.57	2.2	1.4	1

1:Structural parameters with a single Sérsic fit.

2:Structural parameters with a dual Sérsic fit, fixing $n = 4$ for bulge and $n = 1$ for disk components.

3:Rest-frame colors derived with the best fit `EAzY` template.

4:Interaction flag, 0 for galaxies without and 1 for interaction.

5.2.3 Merging Fraction

The latter phase of the two-phase scenario expects frequent minor merging events. While not a few number of studies have already investigated the number of minor merging event by counting surrounding satellites [e.g., Newman et al., 2012], none of those previous studies has focused on massive bulge galaxies as the relic population of compact galaxies. A detail look at surrounding environments of massive bulge galaxies is important in the context of the two-phase scenario.

I count the number of galaxies which have features of interaction with other galaxies, including satellite galaxies. In contrast to what I have done in Chapter 4, for this time I search very nearby of target galaxies ($\lesssim 10$ kpc), and define those with apparent interaction features (tidal tail, asymmetric outskirt, and close companion) as "interacting", so that the uncertainty from phot-z can be minimized. I visually check all 37 galaxies, which are shown in Figure 5.4, and tag those with the interacting feature. For bright galaxies, whose light dominates the postage stamp and disables to visually recognize companions, I make use of the residual image of `GALFIT`. In Figure 5.4, 22 out of 37 galaxies are tagged as interacting.

At the same time, galaxies in the similar mass range ($\log M_*/M_\odot > 10.6$), but with less massive bulge ($\log M_{*,\mathrm{bulge}}/M_\odot < 10.6$), are taken from the same parent sample. These galaxies are also important to be included in discussion because some of them can be the descendant of compact galaxies whose bulges have been destructed. Interestingly, the rate of interaction is higher for this sample than for the massive bulge galaxies. I will discuss this sample in Section 5.3.2, as post-bulge-destructed galaxies.

5.2.4 Mass Increase in Disk

At the same time when estimating the stellar mass in bulge, stellar mass in disk component is calculated by $M_{*,\mathrm{Disk}} = M_{*,\mathrm{total}} - M_{*,\mathrm{Bulge}}$[2]. Stellar mass in disk component obtained in this way ranges $\sim$ 20-80%, with a large scatter, while higher disk fraction galaxies are often tagged with interacting and UVJ starforming, as can be conjectured in Figure 5.3. Merger can even increase the disk mass up to $\sim 70\%$ while keeping the bulge component and star forming property as passive (e.g., 12-1761).

Interestingly, galaxies with higher disk fraction ($\mathrm{B/T} \lesssim 0.4$) are only found at $z > 1$. This is interpreted that low B/T galaxies at $z < 1$ would have to be *more than massive* whose total mass would be $\log M_*/M_\odot \gtrsim 11.5$, by the selection effect in this study. However, these very massive galaxies are expected to form much earlier epoch of $z > 1$ [Abramson et al., 2016, Morishita et al., 2017], and therefore are unlikely to have low B/T. These very massive galaxies are rather observed as, e.g., the brightest cluster galaxies. The high velocity dispersion of the whole system prevents galaxies from further interactions [e.g., Treu et al., 2003], resulting in less likely to be observed as interacting galaxies, neither.

2. This is not exactly disk mass, but rather *non-bulge* mass.

Figure 5.6: UVJ-diagram of massive bulge galaxies

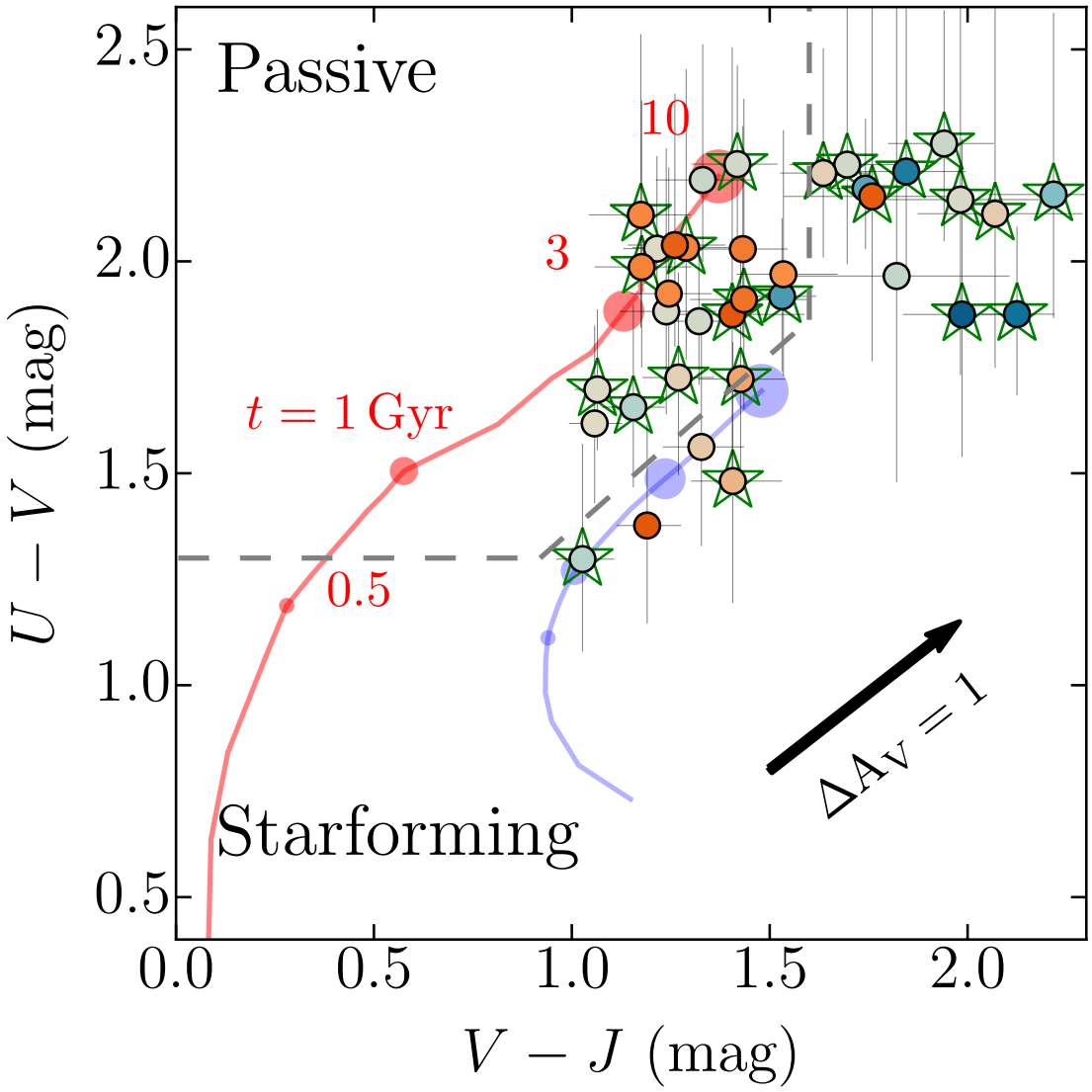

UVJ diagram for massive bulge galaxies, color-coded by B/T (blue is low, red is high values). Those which have merger/accretion features are marked with green stars. While the star-forming and dusty (right top) regions are dominated by merging galaxies, we also observe merging galaxies in the passive region, which implies that interactions for these galaxies do not induce significant star formation (i.e. dry merger). Color evolutions of two stellar evolution tracks, single burst (red line) and constant star formation (blue) models, are shown with ages (0.5, 1.0, 3.0, 10 Gyr from small to large circles). Both star formation histories assume the solar metallicity, Salpeter IMF, and no dust attenuation (typical dust attenuation of $\Delta A_V = 1$ is shown by an arrow). From the location in the diagram, those galaxies have old stellar population of $\gtrsim 1$ Gyr, though dust attenuation may seemingly overestimate the age.

5.2.5 *Rest Frame Colors and Star Formation Properties*

Minor merger can not only accrete to the outer envelope of galaxies and enlarge sizes, but also induce further star formation in some cases when, e.g., there is gas available, which even change galaxy structures. As mentioned in Chapter 4, satellite galaxies around a massive galaxy are still forming stars, while I was not allowed to investigate if they would keep their star formation rate until merged to the host nor induce another star formation. By focusing on galaxies with *interacting* satellites, this question can be pursued by making use of very deep imaging data.

In Figure 5.6, massive bulge galaxies are shown in the UVJ color diagram, a diagnosis of galaxy star-forming properties. It is noted that the star formation rate derived by SED fitting is often affected by assumptions, such as star formation histories and dust attenuation model (Chapter 3). Therefore, I make use of the UVJ diagram to diagnose their star formation activities.

In the right top of the diagram, high fraction of interacting galaxies is observed. The region is known as a dusty star-forming region, as the aging would not bring galaxies to this high $V-J$ value. The abundance of interacting galaxies in the dusty star-forming region implies a possibility that accretion of satellites to massive bulges can induce further star formation (rejuvenation), which is significant enough that the host galaxies are classified as dusty. These interacting galaxies typically have lower B/T than those without interaction, while there are three galaxies in the dusty star forming region with high-B/T (which are discussed below).

On the other hand, in the passive region, I find that $\sim 50\%$ of the galaxies have interaction flag, which implies that galaxies can also keep their quiescence when involved with accreting satellites. Galaxies in the passive region are also characterized to have higher B/T than those in dusty star-forming region. This is reasonable, given the fact that more significant impact from accreting satellites would trigger further star formation and make galaxies more dusty. 16 out of all 37 galaxies are classified as star forming population, while 12 out of 25 interacting galaxies are classified as so.

It is also noted that there might be slight overestimation in the $V-J$ color for high redshift galaxies, as the band coverage in this study (*HST*) does not extend to the rest frame infrared wavelength for them. In Figure 5.7 I show a test of the robustness of the rest frame colors used in this study. I compare the rest frame colors derived by using 7 *HST* bands (Case1) and using 7 *HST*+Ks+IRAC bands (Case2) for same objects from the photometric catalog, which is taken from ASTRODEEP project [Castellano et al., 2016]. The redshift and the rest frame colors are derived in the same manner as in the previous section. The comparison is only made for galaxies with same photometric redshifts for both cases ($|z_{HST} - z_{HST+Ks+IRAC}| < 0.05$), so that we can exclude the effect from the inconsistent redshift estimate. While $U-V$ color for galaxies at $z < 2.5$ and $V-J$ color for $z < 1.0$ show the good agreement, the latter color shows larger scatter for galaxies at $1.0 < z < 2.5$, with possible overestimation in *HST* only color. Although the result is not catastrophic, we need to admit that there might some outliers in the starforming region in Figure 5.6 which have intrinsically bluer $V-J$ color.

Figure 5.7: *UVJ* colors derived only with *HST* bands

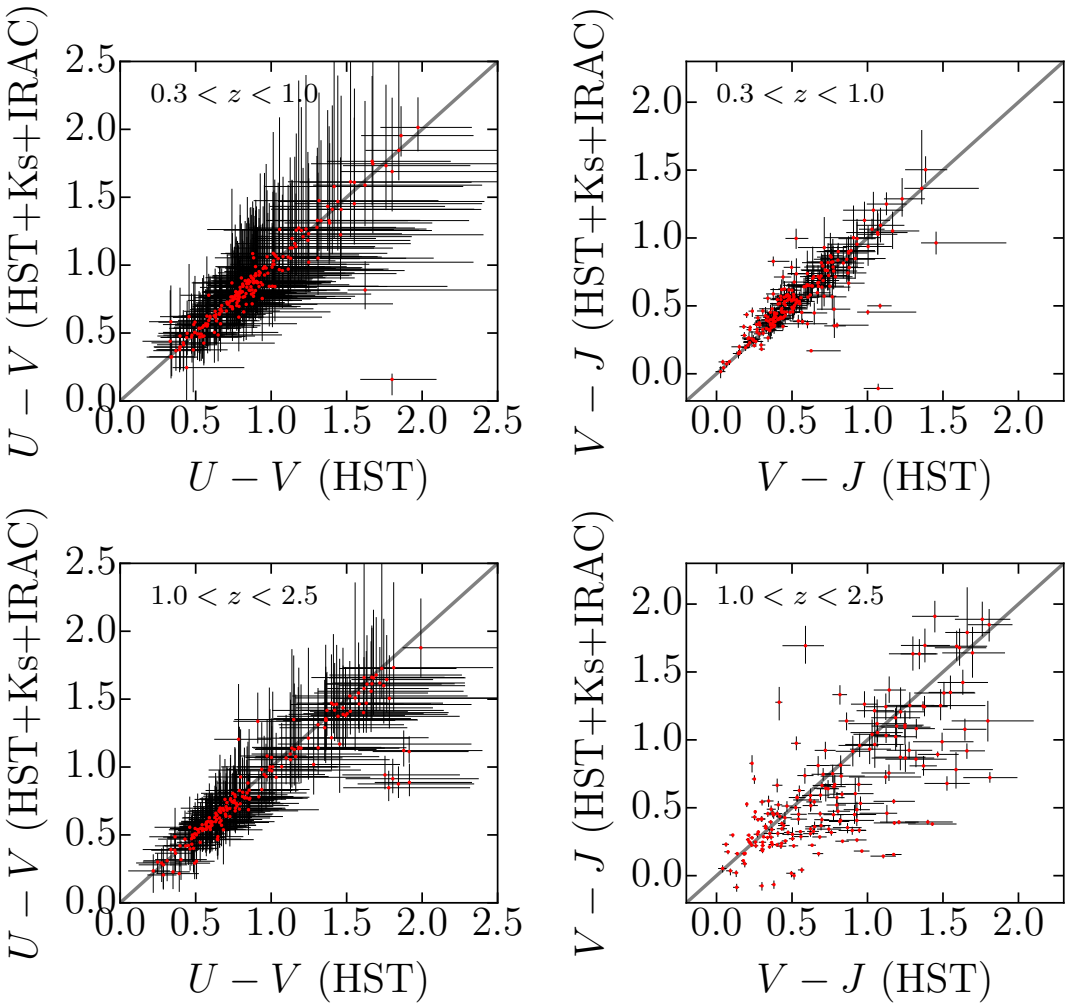

Top: Comparisons of the rest frame $U-V$ (left) and $V-J$ (right) colors derived with 7 *HST* bands (x-axis) and 7 *HST*+Ks+IRAC (Ch1+2) bands (y-axis) for galaxies at $0.3 < z < 1.0$. Only galaxies with $|z_{HST} - z_{HST+Ks+IRAC}| < 0.05$ are shown, to fairly compare the colors with the robust redshift measurement. Error bars are calculated by repeating the MCMC realization within the redshift error. *Bottom:* Same comparison as top panel but for galaxies at $1.0 < z < 2.5$. The scatter in $V-J$ color increases, as the *HST* bands can only cover the rest frame optical wavelength, while the scatter in the $U-V$ remains comparable as for the lower redshift galaxies.

Figure 5.8: Radial profiles of massive bulge galaxy and compact galaxies

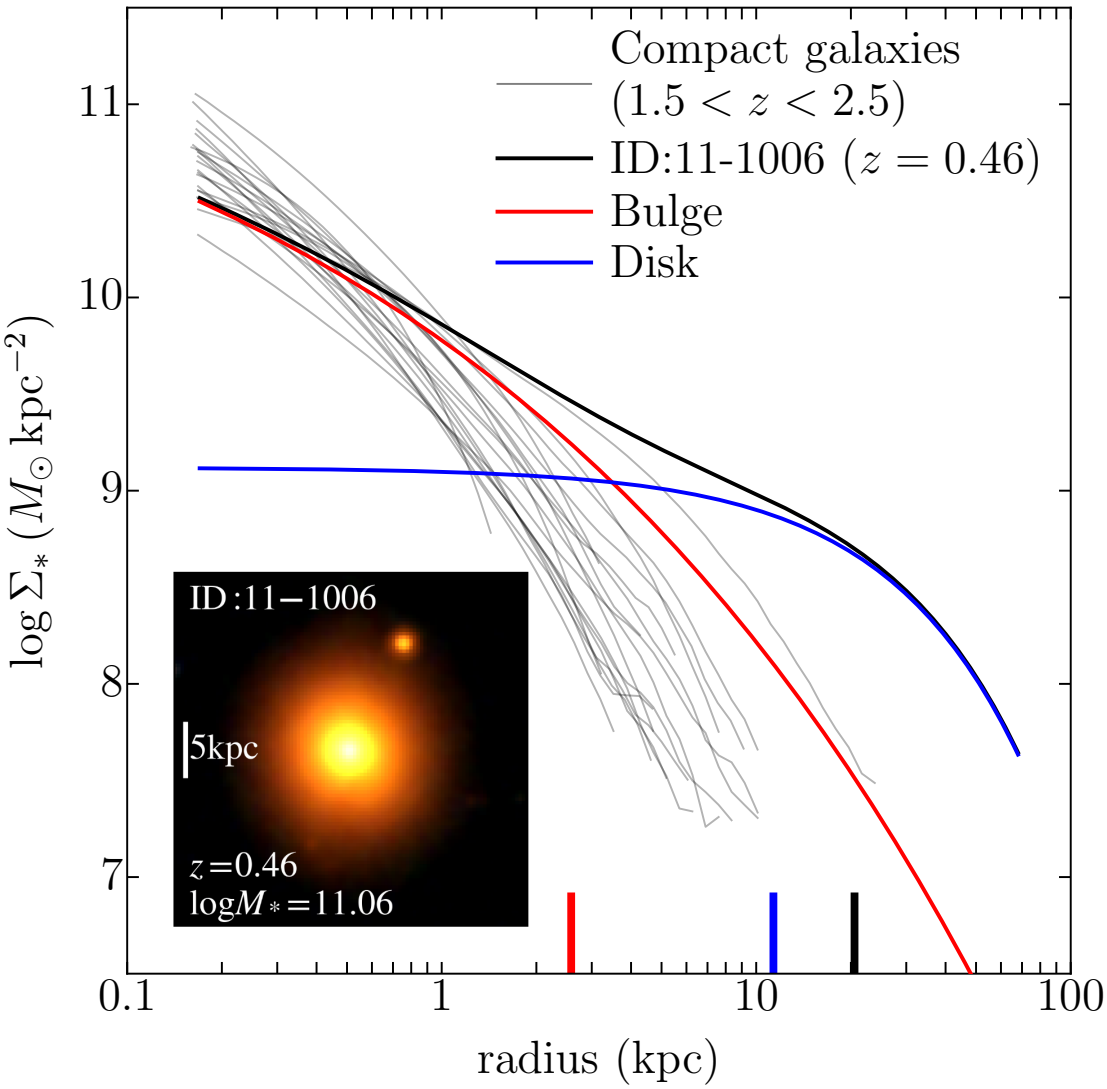

Radial light profile of one of massive bulge galaxies (ID:11-1006, black line), compared with compact galaxies at $1.5 < z < 2.5$ from [Szomoru et al., 2012, gray lines]. Each profile for bulge ($n = 4$, red line) and disk ($n = 1$, blue line) components is also shown. While the total light profile of 11-1006 deviates from the light profiles of compact galaxies, the bulge component shows the similarity, which implies that compact galaxies are buried in non-compact galaxies at low redshifts. The effective radii of the total (black), bulge (red), and disk (blue) components are also indicated in the bottom. While the effective radius for the total galaxy profile is much larger than the typical size of compact galaxies at $z \sim 2$ ($r_e \sim 1$ kpc), the bulge radius is comparable to them.

Figure 5.9: Size-mass relations of massive bulge galaxies

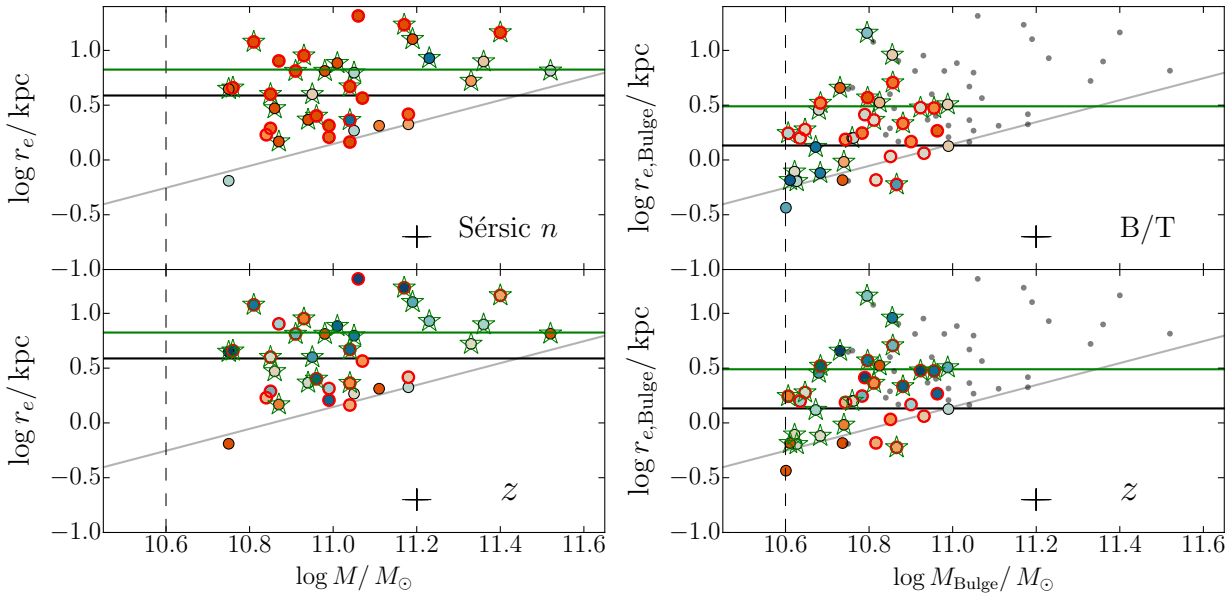

Left: total size-total mass distribution of massive bulge galaxies ($\log M_*/M_\odot > 10.6$; vertical dashed lines). Symbols are same as Figure 5.3, but color-coded (red for high and blue for low values) by Sérsic index (top) and redshift (bottom). The mean sizes for interacting galaxies (green lines) and non-interacting galaxies (black lines) are shown. Criterion for compact galaxies from van Dokkum et al. [2015] is shown (solid gray slopes). *Right:* same as left panel, but for bulge mass and size, color-coded by B/T (top) and redshift (bottom). The total masses and total sizes (from left panels) are shown for comparison (gray dots).

5.2.6 Bulge Size-Mass relation

Bulge size is one of the most important measurements in this study, since galaxies with massive bulge could be compact galaxies before being accompanied by disk component (Chapter 3). Measuring their sizes separately for bulge and disk components can mitigate systematic biases which happens in a single Sérsic fitting — for example, fitting a $(n = 1) + (n = 4)$ profile with a single Sérsic profile returns, say, $n = 2.5$ as the best fit solution, which is less meaningful. One example of this is shown in Figure 5.8. While the total (bulge+disk) profile shows large deviation from those of compact galaxies taken from Szomoru et al. [2012], the bulge profile shows more similarity. The derived effective radius of the bulge component is comparable to the typical size of compact galaxies ($r_e \sim 1$ kpc). To investigate the relation between massive bulge galaxies and compact galaxies, measuring bulge size is necessary for the further understanding of their future evolution path and the role of minor merger.

Firstly, I show the total size-total mass distribution of 37 massive bulge galaxies in Figure 5.9a. The "total size" ($r_{\rm e,tot.}$) is measured by fitting galaxies with a single Sérsic profile, without fixing n to any values. Although the redshift range is wide, the plotted galaxies show a clear trend — galaxies with accreting components have larger sizes than isolated. The mean size for the former is ~ 6.2 kpc, while the latter is ~ 4.8 kpc.

A black line shown in the same plot is a criterion for compact galaxies ($\log r_e < \log M_*/M_\odot - 10.7$) in van Dokkum et al. [2015]. Since the size in van Dokkum et al. [2015] is circularized ($r_e = \sqrt{q} \times a_e$), I correct the criterion for noncircularized radius for the present study by adding $\log\langle q \rangle \sim 0.076$. The definition differs in different studies [e.g., Barro et al., 2015], though changing the value does not affect the result here. With this criterion, I find three compact galaxies in the present sample. Two of them (11-1723, 12-347) have no accreting flag, and Sérsic indices $\sim$ 2-4, consistent with observed compact galaxies [van der Wel et al., 2010, Szomoru et al., 2012, Barro et al., 2015].

In Figure 5.9b, I then show the bulge size-bulge mass distribution of the same galaxies. Interestingly, I find bulge sizes are consistent with the compact criterion (~ 1.9 kpc and ~ 2.9 kpc, respectively). Those galaxies with large shift from $r_{\rm e,tot.}$ to $r_{\rm e,bulge}$ are mainly those with small B/Ts, which implies compact galaxies are buried in larger size (disky) galaxies. While similar analysis have already conducted for local galaxies and find the relics of compact galaxies [e.g., Trujillo et al., 2014], this is showing that massive bulges are under-constructing their outer envelope at higher redshifts.

The average bulge size of the interacting galaxies is still higher than those isolated. This might indicate that bulge size also grows through stellar accretion, though the residual at the outer radius can also affect the size. This is discussed in the following section.

Figure 5.10: ΔM_*-Δr_e of massive bulge galaxies

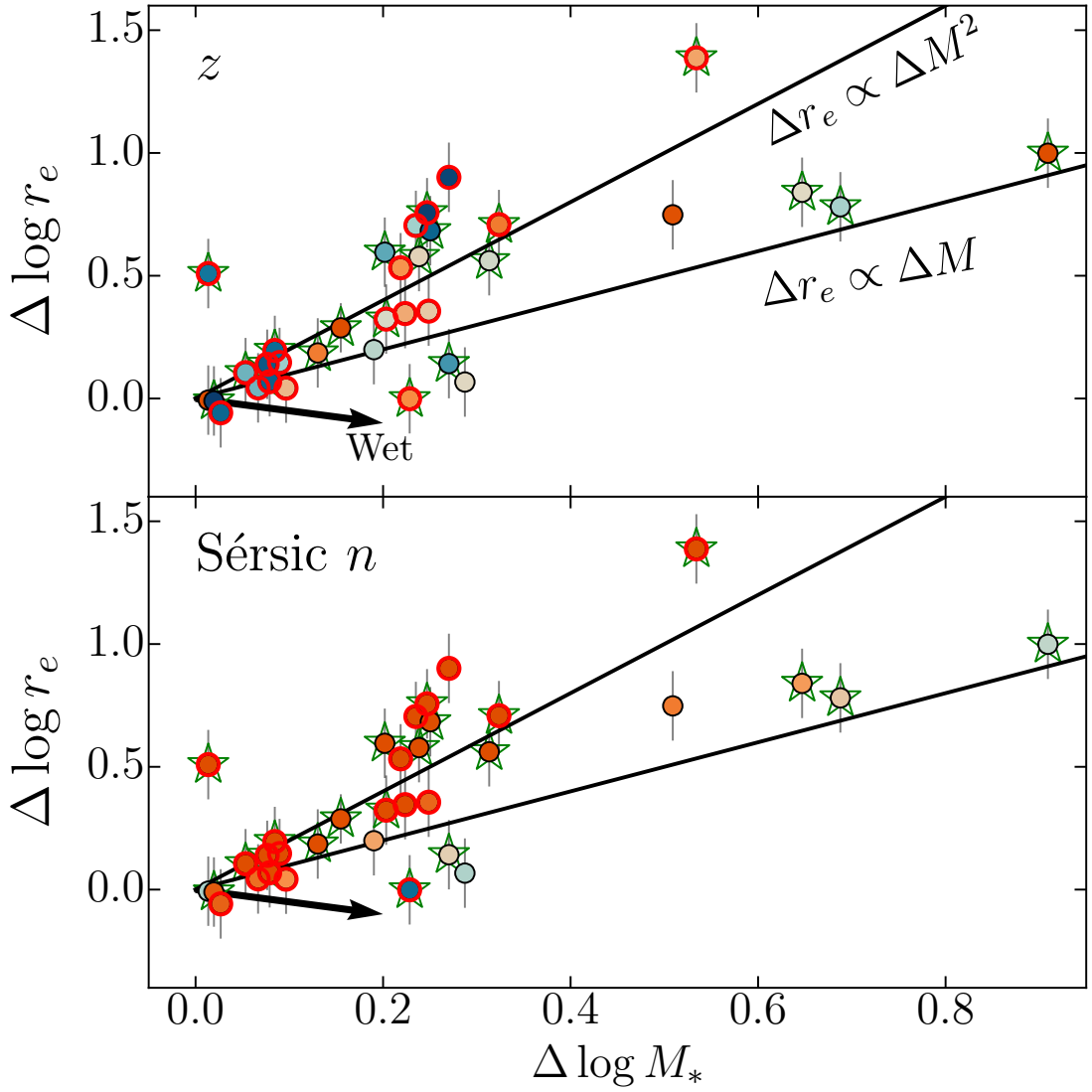

Distribution of offsets in stellar mass ($\Delta \log M_* \equiv \log M_{*,\mathrm{tot}} - \log M_{*,\mathrm{bulge}}$; it is noted that $\Delta \log M_*$ is a function of B/T) and radius ($\Delta \log r_\mathrm{e} \equiv \log r_{\mathrm{e,tot}} - \log r_{\mathrm{e,bulge}}$) for the massive bulge galaxies. Each plot is color-coded by and z (top) and Sérsic index (bottom). Passive galaxies in the UVJ-diagram are marked with red circles, and those with accretion features with green stars. Two lines, $\Delta \log r_e = \eta \Delta \log M_*$ (equivalent to $\Delta r_e \propto \Delta M_*^{\eta}$), with $\eta = 1$ and $\eta = 2$ are motivated by theoretical expectation for major and minor mergers, respectively, while the region below $\eta = 1$ line (arrow, though the slope is uncertain) is thought for highly dissipative merger[e.g., Ciotti et al., 2007, Naab et al., 2009].

Figure 5.11: Histogram of η

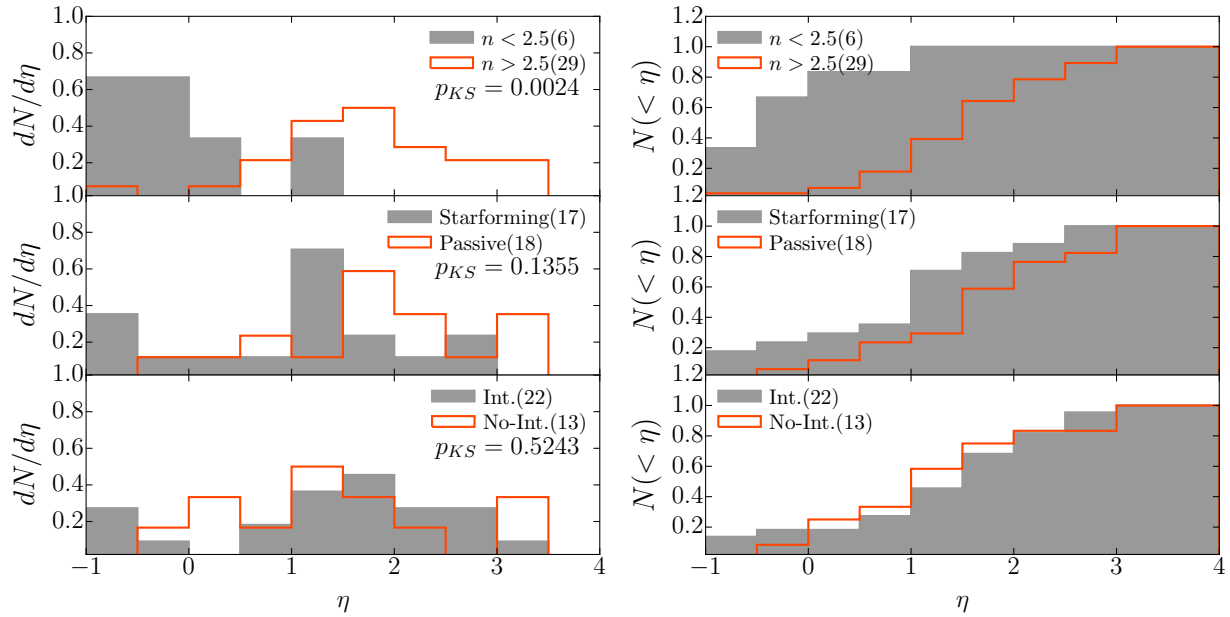

Left: distributions of $\eta = \Delta \log r_e / \Delta \log M_*$ for the present galaxies, separated by Sérsic index (top), UVJ colors (middle), and interaction flag (bottom). Each histogram is normalized in each subgroup. The result of Kolmogorov-Smirnov (K-S) test in each group is shown, which confirms distinctive distributions for subgroup of Sérsic index (the probability that both distributions are identical is $p_{KS} = 0.0024$) and UVJ colors ($p_{KS} = 0.1355$), while much weaker signal those divided by interaction flags ($p_{KS} = 0.5243$). It is noted that four galaxies with $\Delta r_e = 0$ (i.e. B/T=1) are not included here. *Right:* same histograms as left, but in cumulative ways.

5.3 Discussion

5.3.1 Impact of minor merger

I begin this section by investigating the impact of minor merger to massive bulge and size/mass growth. The argument for galaxy size growth, as a function of mass growth, usually assumes the virial theorem [e.g., Hopkins et al., 2009a, Naab et al., 2009] and gives us the following equation;

$$\Delta r \propto \Delta M^{\eta}, \tag{5.1}$$

where $\eta \sim 1$ for dissipative (and qual mass) merger, and $\eta \sim 2$ for minor (1:3 or larger ratio) merger. The argument also assumes the merging to be dissipationless for the effective growth [see, e.g., Hopkins et al., 2009a], though this assumption is not always true as discussed in Chapter 4 and Morishita and Ichikawa [2016].

In Figure 5.10, I show offsets in size ($\Delta \log r_{\rm e} \equiv \log r_{\rm e,tot} - \log r_{\rm e,bulge}$) and mass ($\Delta \log M_* \equiv \log M_{*,\rm tot} - \log M_{*,\rm bulge}$) for the present sample, to study the evolution mechanism of each galaxy. Along the $\eta = 2$ line, we see high-Sérsic n galaxies more, compared to those around the $\eta = 1$

line. In a case of dry merger, which would mostly contribute to the outer part of galaxies, the radial profile reasonably would become to have higher Sérsic index. It is noted that $> 50\%$ of these $\eta = 2$ galaxies are characterized as passive in the UVJ diagram (marked with red circles), while those on and below the $\eta = 1$ line region is dominated by non-passive galaxies. This implies that the dissipationless merger is more effective to increase galaxy sizes, or equivalently, that the dissipative merger induces star formation and in this case the size growth would be less effective than the dissipationless case. Galaxies with the largest mass increases ($\Delta \log M_* \gtrsim 0.6$; IDs 15-1014, 15-1983, and 16-878) all show prominent features of (possibly major) merger.

Figure 5.11 shows the histograms of η for different subgroups of galaxies, Sérsic index, UVJ colors, and interaction flags. The most distinct distributions are observed for the subgroup with Sérsic index — larger Sérsic index galaxies tend to follow $\eta = 2$ line while lower ones $\eta = 1$ or less. The Kolmogorov-Smirnov (KS) test confirms the distinct distribution, with the probability that those two are identical is $p_{KS} \sim 0.3\%$. Given the definitions of $\Delta \log r_{\rm e}$ and $\Delta \log M_*$, this suggests that those with larger Sérsic indices have more extended wings which increase galaxy radii.

Although weaker, the distinctness of distributions is seen in the second subgroup. The fact that passive galaxies tend to follow the $\eta = 2$ line supports the longstanding idea that the dry minor merger would increase galaxy sizes efficiently without significant star formation. On the other hand, star-forming galaxies tend to have lower η, i.e. less efficient size growth. The bottom panel shows that the distributions of interacting and non-interacting galaxies have similar distributions, as confirmed by a high probability from K-S test ($p_{KS} > 60\%$). This implies that the result would hardly be changed depending on the merger/interaction, as these signatures will disappear at some point without significantly affecting the measurements (B/T, $\Delta \log r_{\rm e}$). However, it is noted that the selection in this study is based on the bulge mass, and therefore the observed interaction is not significant as to destruct the bulge (see Section 5.3.2).

Therefore, according to the mass/size increase diagram, I conclude that the mass accretion to massive bulge galaxies can be caused either by dry merger scenario ($\eta = 2$ line), which results in high-Sérsic n and no significant star formation, or by wet merger/major merger scenario (on/below $\eta \lesssim 1$ line), which results in low Sérsic n and star formation. These variation can, for example, be depending on remained gas available for further forming stars in host/satellite galaxies. Although it is beyond the present study, surrounding environment is another key parameter [Dressler, 1980, Peng et al., 2010] to investigate the observed diversity, and thus wide field observations around selected massive galaxies would provide further insight.

5.3.2 Unselected Massive Galaxies

The present galaxies are selected by bulge mass, so that I can study evolution path(s) of massive galaxies after their core (bulge) formation. However, it is possible that there are galaxies which used to have massive bulge but have been destructed at later epochs and therefore not been selected in this study. Although the quantitative discussion is harder for this case (because there is no way only with the present data to find out massive galaxies which used to be compact), it is important

Figure 5.12: *UVJ*-diagram of less massive bulge galaxies

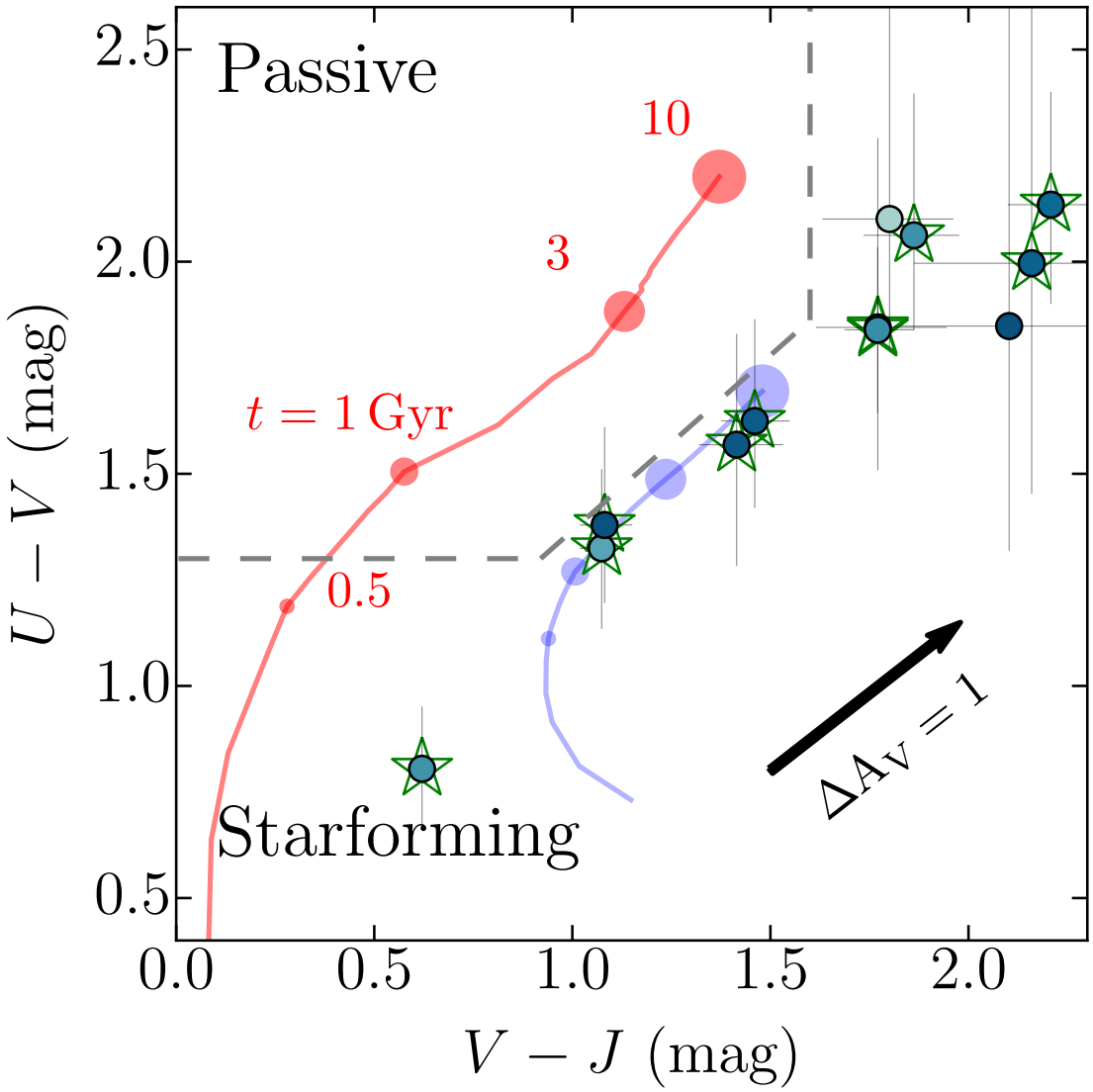

Same as Figure 5.6, but for less massive bulge galaxies. All the galaxies are classified as star forming, and most of them have the feature of interaction.

Table 5.2: Physical Properties of Less Massive Bulge Galaxies

ID	z	$\log M_*$ ($\log M_\odot$)	m_{tot}[1] (mag)	r_{tot}[1] (kpc)	n_{tot}[1]	χ^2_{tot}/ν	m_{bulge}[2] (mag)	r_{bulge}[2] (kpc)	m_{disk}[2] (mag)	r_{disk}[2] (kpc)	χ^2_{bd}/ν	B/T	U-V[3] (mag)	V-J[3] (mag)	$f_{int.}$[4]
11-786	1.325	11.0	22.0	6.9	1.3	0.280	24.8	1.4	22.1	7.4	0.215	0.08	1.8	2.1	1
12-166	1.709	11.2	22.2	4.2	3.1	0.395	23.8	1.2	22.7	4.2	0.333	0.27	2.1	1.9	1
12-570	1.500	11.1	22.0	4.7	0.9	0.274	23.3	18.7	22.2	4.4	0.264	0.26	1.8	1.8	1
12-1960	1.553	11.0	21.1	3.1	4.2	0.519	22.6	0.6	21.8	3.3	0.288	0.31	1.3	1.1	0
15-218	1.983	11.1	23.1	2.1	3.5	0.409	24.5	0.4	23.6	2.6	0.379	0.31	2.2	1.7	1
15-1512	2.239	11.1	20.6	11.0	7.4	0.374	22.6	0.6	21.5	5.4	0.210	0.27	0.8	0.6	1
15-1711	1.308	11.1	21.9	4.8	2.3	0.331	24.0	0.5	22.1	5.2	0.221	0.15	2.0	2.2	1
16-920	1.699	11.1	21.6	6.1	2.6	0.565	24.1	0.3	21.9	6.1	0.301	0.12	1.6	1.5	1
99-30	1.177	11.0	20.5	7.7	2.1	0.205	23.1	1.0	20.8	7.2	0.161	0.11	1.6	1.4	1
99-372	1.550	11.2	21.4	10.3	3.7	1.428	23.6	0.7	21.9	7.7	0.821	0.17	2.1	2.2	1
99-1742	1.310	11.0	21.3	4.1	2.3	2.457	22.9	1.7	21.8	4.1	1.521	0.26	1.8	1.8	1
99-3369	2.555	10.7	24.4	2.0	3.7	1.097	25.4	0.4	25.1	2.9	1.086	0.44	2.1	1.8	0

1:Structural parameters with a single Sérsic fit.
2:Structural parameters with a dual Sérsic fit, fixing $n = 4$ for bulge and $n = 1$ for disk components.
3:Rest-frame colors derived with the best fit EAzY template.
4:Interaction flag, 0 for galaxies without and 1 for interaction.

to study massive galaxies comparable to the total mass of massive bulge galaxies but with different bulge mass from the present criterion. If those galaxies were considered to be the *post*-compact galaxies, the impact by stellar accretion estimated in Section 5.3.1 could be underestimated for some degree.

To see these galaxies, I select massive galaxies with the same criterion ($\log M_*/M_\odot > 10.6$) but less massive bulge ($\log M_{*,\mathrm{bulge}} < 10.6$) — in total 84 galaxies are found. These galaxies do not satisfy the criterion for massive bulge galaxies, because they are 1. dominated by prominent $n = 1$ disks (i.e. bulge mass would be less than $\log M_*/M_\odot = 10.6$), and 2. the total masses are not as massive as the massive bulge galaxies. Surprisingly, the number of galaxies with accreting satellite is 55, or $\sim 65\%$ of the whole sample.

However, as mentioned, total masses of these galaxies are typically smaller than those of massive bulge galaxies, and therefore much less massive than massive galaxy progenitors in Chapter 3. To avoid the bias of comparing galaxies at different masses, I then switch to choose massive galaxies in the same criterion as for MGs (Equation 3.1, and also above this), but with less massive bulges ($\log M_{*,\mathrm{bulge}}/M_\odot < 10.6$). The selected 12 galaxies are shown in Figure 5.13, and their properties are summarized in Table 5.2.

Most of these galaxies show prominent features of on-going merger. Even during major merging, however, about half of these galaxies have cores, rather than complete absence/being destructed.

These galaxies are all classified as star-forming in Figure 5.12, and half of which are in dusty region, as expected from the high fraction of interaction. Since age estimate would be significantly suffered from degeneracy with dust attenuation in this diagram, I refrain from any conclusion about their origin (e.g., if their progenitors were bulge dominated galaxies or not; see also Section 5.3.3). Independent measurement for dust attenuation and age indicators (e.g., D_n4000) will solve the

Figure 5.13: RGB stamps of less massive bulge galaxies

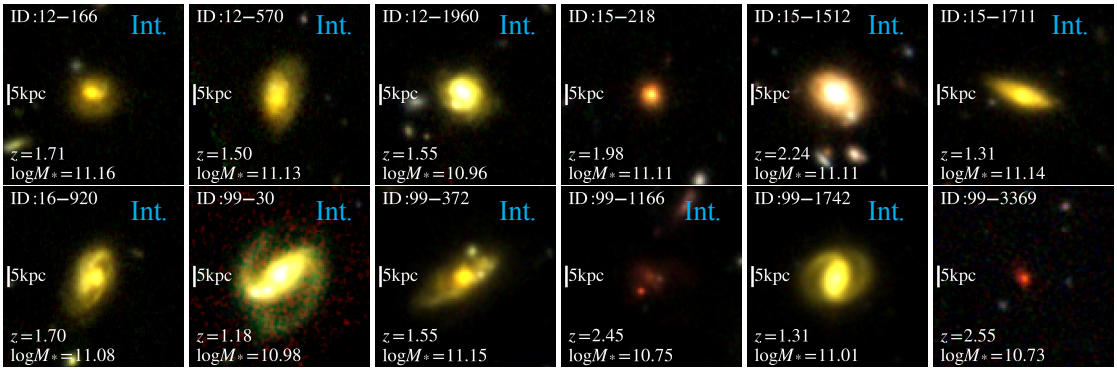

Same as Figure 5.4, but for less massive bulge galaxies ($\log M_{*,\mathrm{bulge}}/M_{\odot} < 10.6$ and $\log M_{*}/M_{\odot} > 11.42 - 0.068z - 0.04z^2$). Most of them are interacting, while two galaxies are small and unresolved.

degeneracy and provide further insight into these galaxies.

It is also possible that 12 galaxies here would (re-)construct the massive bulge component when relaxed (see also Section 5.3.3). The typical time scale for major merger is ~ 1 Gyr, and therefore these galaxies have enough time to be observed as massive bulge galaxies at $z < 1$, if bulges would be formed. Even though these galaxies would be possible to have similar light profiles that we are witnessing for the massive bulge galaxies at later epochs, the stellar properties should indicate distinct features (e.g., younger age, less alpha enhancement, more metal rich) from what have seen in compact/massive bulge galaxies. Precise measurements for age and abundance ratios would lead to conclusive discussion [Thomas et al., 2005, Choi et al., 2014][3].

5.3.3 Alternative Scenarios for Massive Bulge+Disk Galaxies

I have studied galaxies with massive bulge (+disk/accreting components), as the relic of compact galaxies, based on the result obtained in Chapter 3, and also theoretical expectations in two-phase scenario. However, it is necessary to take account for alternative scenarios for the formation of massive bulge galaxies.

For example, the violent disk instability [Noguchi, 1998, Bournaud et al., 2007] is known to rapidly form such systems from highly dissipative gas disks, i.e. from disk then bulge or in "outside-in" scheme. However, the mechanism is usually accompanied with giant star forming clumps within disk, which is not observed in the present sample, but rather for less massive galaxies [e.g., Guo et al., 2015], as seen in the less massive galaxy sample in Section 5.3.2. The colors in UVJ-diagram also imply that the present galaxies have old stellar population ($\gtrsim 2$ Gyr, though dust attenuation might overestimated age), while disk instability can reproduce relatively young bulges

3. These measurements would also be ideal to handle previously discussed issues such as progenitor bias in size-mass diagram [Carollo et al., 2013].

($\lesssim 1$ Gyr). In the present sample, no such young galaxies are observed in Figure 5.6. Therefore, I safely conclude that the sample galaxies in this study are not likely to be formed through such an outside-in scheme.[4]

Among 12 less massive bulge galaxies in Figure 5.12, I find one galaxy with a young age. The galaxy, 15-1512, is at $z \sim 2.24$ and surrounded by few blobs, though not very much like a typical clumpy galaxy. With the present data, it is not possible to conclude this galaxy is at the late stage of clump migration or galaxy with merging satellites.

The progenitor bias [van Dokkum and Franx, 1996, Carollo et al., 2013, Choi et al., 2014] — recently quenched (larger size) star-forming galaxies can be mixed in ancient quenched galaxies — is also discussed in literatures and to be mentioned here. However, as already discussed above, these newly quenched galaxies typically have younger age than descendants of compact galaxies. In addition, these galaxies have low Sérsic index [Morishita et al., 2014, Whitaker et al., 2016], and therefore less bulge dominated, unlike massive bulge galaxies observed in this study. *Unless* there is a significant morphological change accompanied with quenching [e.g., Martig et al., 2009, Genzel et al., 2014], massive bulge galaxies observed in this study are unlikely to be recently quenched star-forming galaxies.

5.3.4 So, what is the fate of compact quiescent galaxies?

We now know that the massive bulge galaxies are involved with both dry and wet mergers — about half of them are classified as star forming. From the result, I am allowed to make a prediction of the fate of compact galaxies in the following ~ 10 Gyr. As discussed in Chapter 4, the possible evolution paths for compact galaxies are;

1. Compact galaxies (i.e. no interaction).
2. Elliptical galaxies through a number of dry minor merger events.
3. S0 or later type galaxies through dissipative process.
4. Disappear (i.e. bulge is destructed or absorbed by a larger galaxy).

The first scenario is investigated in a number of previous studies, most of which conclude it is unlikely in the normal field [e.g., Taylor et al., 2010]. The number density of compact galaxies in the local universe is, at least, by an order of magnitude lower [$n \sim 10^{-5}$ Mpc^{-3}; e.g., Valentinuzzi et al., 2010] than high-z [$n \sim 10^{-4}$ Mpc^{-3}; e.g., Barro et al., 2013]. Although there is a claim that compact galaxies survive in the dense environment, such as a cluster of galaxies [e.g., Poggianti et al., 2013], the limited survey volume of the high-z universe with 1 kpc resolution (i.e. *HST* imaging) makes it difficult to study the environment of the compact galaxies and compare the

4. Disk instability could be an ideal mechanism for the formation of massive bulges, which are observed as compact star-forming galaxies at higher redshift range than the present study [Barro et al., 2013, Tadaki et al., 2014, Tacchella et al., 2015].

number density with the one in the local universe. The future large volume survey, such as WFIRST [Spergel et al., 2015], will provide plenty of high-z galaxies for the purpose.

The second scenario, which has been believed for long time and the key of this study, can be assessed by using the estimates in the previous sections. For example, to increase the mass from $\log M_*/M_\odot = 10.8$ (the median of the present sample) to $\log M_*/M_\odot = 11.5$ (a typical mass of local elliptical galaxies), we need ~ 6 times of 1:3 merger. By taking the fraction of passive galaxies in Figure 5.6, the fraction of compact galaxies to be classified as star-forming can be estimated as $p_{SF} = (N_{SF} \pm \sqrt{N_{tot}})/N_{tot} = (16 \pm 6.1)/37 = 0.43 \pm 0.17$. Therefore, the probability that a passive galaxy would not resume star formation after $n = 6$ times 1:3 minor merger is,

$$p = (1 - p_{SF})^n \sim 0.034^{+0.130}_{-0.030}, \tag{5.2}$$

which is very low possibility as *an standard evolution theory* of compact galaxies. It is noted that host galaxies which induce star formation temporarily could quickly quench and be observed as passive at the final mass. In this case, the probability would be more likely than the estimate here. However, in this case the observed stellar population would be younger, inconsistent with previous studies of local ellipticals [e.g., Thomas et al., 2005, Treu et al., 2005].

In related with the third scenario, de la Rosa et al. [2016] studied the morphology of the hosts of local massive bulge galaxies, and found the following fractions at a mass range of $11 < \log M_*/M_\odot < 11.5$; $\sim 40\%$ for elliptical, $\sim 40\%$ S0, and $< 15\%$ late-type galaxies. Considering that elliptical galaxies also contain the outcome from major merger, whose origins are not necessarily massive bulge galaxies, the more favorable fate of massive bulge (i.e. compact galaxies) studied here is likely to be S0/later type galaxies, rather than elliptical. Given the observed decrease of the number density of compact galaxies from $z \sim 1$ to 0 [Cassata et al., 2013, Damjanov et al., 2015], the unlikeliness of the *standard* two-phase scenario is not outlandish. This conclusion is also strengthen by findings from galaxy kinematics — fast rotators at slightly less massive range ($10.5 < \log M_*/M_\odot < 11.3$, similar to the present mass range) while slow rotators at more massive range [e.g., Cappellari et al., 2013, ; see also Tapia et al. 2014 for a simulation of S0 formation].

In the fourth scenario, compact galaxies would be destructed by violent mechanisms (e.g., merger with gas rich galaxies) or absorbed by larger galaxies. As discussed in Section 5.3.2, in the former case galaxies are observed as, e.g., less massive bulge galaxies (Figure 5.13).

One important note is that the typical compact galaxies are not the most massive galaxies at $z \sim 2$. A recent study by Patel et al. [2017] showed that the most massive galaxies at $z \sim 2$ are actually more massive than typical compact galaxies ($\log M_*/M_\odot > 11.25$; cf. $\log M_*/M_\odot \sim 11$ of compact galaxies) and have larger sizes ($r_e \sim 3$ kpc; cf. $r_e \sim 1$ kpc), but they are just rare and hardly found in previous surveys, such as CANDELS. When these massive galaxies are connected to the size of local massive galaxies at a given mass, the expected size growth would be by a factor of ~ 3, much smaller than the previously expectation for compact galaxies. Large field near-infrared imaging surveys, such as WFIRST, will provide further insight with robust statistical power.

5.4 Summary

Motivated by an average picture derived for massive galaxies in Chapter 3, I studied massive bulge galaxies individually to understand the fate of compact galaxies, as previously challenged in Chapter 4. While the derived picture ("two-phase" scenario) expects the formation of massive bulges ($\log M_*/M_\odot \sim 10.8$) at $z \sim 2$, after which the stellar accumulation happens mostly at the outer part of galaxies, massive galaxies show a large scatter in the derived bulge mass. This implies that galaxies selected at a fixed number density are yet the mixture of diversity, as discussed in Section 3.4.4. Motivated by this inconsistency, I selected galaxies at a fixed bulge mass ($10.6 < \log M_{*,\mathrm{bulge}} < 11$), as the relic of compact galaxies at higher redshifts, to study the ongoing process directly and quantitatively assess the favored two-phase scenario. The main conclusions are as follows;

1. Massive bulge galaxies are observed either as passive/star-forming galaxies, with early-type/interacting appearance, i.e. *anything*, all of which have been expected in Chapter 4.

2. Some galaxies classified as passive galaxies can still have accretion features, which implies that the satellite accretion proceeds in a dissipationless manner for these systems.

3. Those classified as star-forming are more likely accompanied by satellite galaxies/accretion features, which implies that the minor merging can also induce/resume the star formation activity.

4. While there are few galaxies which satisfies the compact galaxy criterion in the total size-total mass diagram, more galaxies satisfy the criterion when looked in the bulge size-bulge mass space, implying that these bulges can used to be compact galaxies in the past, as demonstrated in Figure 5.8.

5. By looking at the relation between increases in mass and size ($\Delta r \propto \Delta M^{\eta}$), I discussed physical mechanisms which have derived the size increase in Figure 5.10.

6. Those classified as passive galaxies are aligned on and around $\eta = 2$ line (i.e. dry minor merger), while those classified as star forming with interaction are on and below $\eta = 1$ line (i.e. major merger and dissipation merger), which implies dry merger is more efficient to increase galaxies sizes.

7. While dry merger is a favorable mechanism for compact galaxies to be the local elliptical galaxies, the derived probability is very low ($p \sim 3\%$; Section 5.3.4), and other paths to, for example S0s, are comparably worthy to be taken account for.

CHAPTER 6
SUMMARY OF THESIS

In this thesis, I studied the properties of massive galaxies at $z < 3$, and derived the evolutionary picture over the redshift range, focusing on the fate of compact galaxies recently found at $z > 1$. These galaxies are literally believed to be local early-type galaxies, through a number of dry minor merger events which increase their measured size by a factor of ~ 5. From the global properties obtained in Chapters 2 and 3, the evolutionary picture is found to be, at some degree, a good approximation. However, when I see each composing galaxy in detail, there is still huge scatter in their properties, such as morphology (Section 3.4.3) and bulge mass (Section 5.1). This implies that these compact galaxies would possibly evolve in divergent ways, as suggested in Chapter 4. Since the diversity of the evolutionary paths has not been quantitatively investigated yet, I studied small number of galaxies (< 100) in Chapter 5. While about a half of massive bulge galaxies remain their star formation property as quiescent, even with merging/accreting component, the other half are classified as starforming galaxies, which can be interpreted that these galaxies resume forming stars after forming massive bulges. This reconfirmed that the fate of compact galaxies are not necessarily elliptical galaxies, as believed in literature without doubt, but can also be S0/later types.

One question we may want to ask is, then, "which compact galaxies would become present typical elliptical galaxies, including the most massive galaxies in clusters?" Intensive studies of stellar population in $z < 1$ galaxies from literature [e.g., Thomas et al., 2005, Treu et al., 2005] have revealed that those elliptical galaxies have stopped forming stars for $\gtrsim 10$ Gyr, i.e. $z_{\rm form} \gtrsim 2$, after which they have increased mass by accretion. Actually, the progenitors of those passive galaxies recently start to be found at $z > 3$ with very sensitive ground-based spectroscopic observations [Marsan et al., 2015, Glazebrook et al., 2017], with prominent 4000 Å absorption features [estimated age is ~ 0.5-1 Gyr; Glazebrook et al., 2017] and submm bands detection [with obscured SFR of $\sim 100\,M_\odot\,{\rm yr}^{-1}$; Simpson et al., 2017]. However, these galaxies are typically already more massive ($\log M_*/M_\odot \gtrsim 11.25$) than the bulge mass studied in Chapter 5. These galaxies are also not compact but rather have larger radius [$\langle r_e \rangle \sim 3$; Patel et al., 2017], which mitigate the significant size evolution through minor mergers. Such super massive galaxies are rare ($\sim 10^{-5}\,{\rm Mpc}^{-3}$) and hardly discovered in the present or other surveys based on *HST*.

Given these facts, massive elliptical galaxies found in the local universe *must* be, at least, passive galaxies with massive bulge at the redshift of Chapter 5, and might be missed because of upper mass limit, $\log M_{*,\rm bulge}/M_\odot = 11$ (but some of the most massive galaxies in Figure 2.12 can be good candidates). In this sense, the massive bulge galaxies classified as star-forming are reasonably excluded from the candidates. However, any other conclusions cannot be made only with the data presented in this thesis.

One key parameter, which I could not discuss in this thesis, would improve the situation — kinematics. Galaxy kinematic parameters, such as rotation velocity and dispersion, represent galaxy structural properties in much more accurate ways. Recent deep NIR spectroscopic observations [e.g., van Dokkum et al., 2009, Onodera et al., 2012, van de Sande et al., 2013, Belli

et al., 2014, Newman et al., 2015, Belli et al., 2017] have successfully obtained the stellar velocity dispersion of passive galaxies through absorption features, and shown that these massive (compact) galaxies are dispersion supported systems ($\sigma \gtrsim 200$ km/s). Selecting galaxies based on a fixed velocity dispersion would be an alternative (and probably better) opportunity to trace galaxy evolution over wide redshift range.

Another question yet to be answered is the progenitor of compact galaxies. Since the compact galaxies are already passive and massive at $z \sim 2$, it is required to study $z > 3$ galaxies as their progenitors. Recent progress is made by looking their starforming progenitors at similar redshifts, compact starforming galaxies or so called "blue nuggets" [Barro et al., 2013, Tadaki et al., 2014]. AGN activity and formation of massive black hole are expected to have key roles at such high redshift range, as these are known to be strongly related to star formation activity [e.g., Bundy et al., 2008, Cheung et al., 2016] and bulge formation [e.g., Magorrian et al., 1998, Häring and Rix, 2004]. Although these previous studies have revealed many new aspects of compact starforming galaxies through nebular emission lines (e.g., gas-phase kinematics), comprehensive studies are still suffered from the limitation by their intrinsic properties (i.e. dusty) and instrumental aspects. To unveil their dust/starforming properties, resolved submm observations (e.g., ALMA) would help [e.g., Tacconi et al., 2013, Tadaki et al., 2017]. By mapping their dust/gas geometry, and possibly kinematics, further arguments of their *future* star formation would be made. These insight would then help to reveal the origin of correlation between their quiescence and structural properties.

Finally, another improvement would be achieved by having deep insight into their chemical abundances and IMF. It is recently known that the IMF of massive galaxies is not universal but rather become bottom heavier in the past [e.g., van Dokkum et al., 2008, Treu et al., 2010, Cappellari et al., 2012]. For example, NIR spectroscopy with *JWST*/NIRSPEC would cover the optical feature for galaxies at $2 < z < 5$. By making use of optical absorption lines to obtain metallicity, alpha abundance ratios, and IMF sensitive features [e.g., Conroy et al., 2014, Choi et al., 2014], we would have access to the formation of massive galaxies at the very first phase of their formation. By adding these information to much finer resolution imaging by *JWST*/NIRCAM, we are finally allowed to comprehensively cover the fate of compact galaxies from the beginning.

REFERENCES

R. G. Abraham and S. van den Bergh. The Morphological Evolution of Galaxies. Science, 293: 1273–1278, August 2001. doi: 10.1126/science.1060855.

L. E. Abramson, M. D. Gladders, A. Dressler, A. Oemler, Jr., B. Poggianti, and B. Vulcani. Return to [Log-]Normalcy: Rethinking Quenching, The Star Formation Main Sequence, and Perhaps Much More. ApJ, 832:7, November 2016. doi: 10.3847/0004-637X/832/1/7.

D. M. Alexander, F. E. Bauer, W. N. Brandt, D. P. Schneider, A. E. Hornschemeier, C. Vignali, A. J. Barger, P. S. Broos, L. L. Cowie, G. P. Garmire, L. K. Townsley, M. W. Bautz, G. Chartas, and W. L. W. Sargent. The Chandra Deep Field North Survey. XIII. 2 Ms Point-Source Catalogs. AJ, 126:539–574, August 2003. doi: 10.1086/376473.

J. E. Barnes. Encounters of disk/halo galaxies. ApJ, 331:699–717, August 1988. doi: 10.1086/166593.

G. Barro, S. M. Faber, P. G. Pérez-González, D. C. Koo, C. C. Williams, D. D. Kocevski, J. R. Trump, M. Mozena, E. McGrath, A. van der Wel, S. Wuyts, E. F. Bell, D. J. Croton, D. Ceverino, A. Dekel, M. L. N. Ashby, E. Cheung, H. C. Ferguson, A. Fontana, J. Fang, M. Giavalisco, N. A. Grogin, Y. Guo, N. P. Hathi, P. F. Hopkins, K.-H. Huang, A. M. Koekemoer, J. S. Kartaltepe, K.-S. Lee, J. A. Newman, L. A. Porter, J. R. Primack, R. E. Ryan, D. Rosario, R. S. Somerville, M. Salvato, and L.-T. Hsu. CANDELS: The Progenitors of Compact Quiescent Galaxies at z ˜ 2. ApJ, 765:104, March 2013. doi: 10.1088/0004-637X/765/2/104.

G. Barro, S. M. Faber, P. G. Pérez-González, C. Pacifici, J. R. Trump, D. C. Koo, S. Wuyts, Y. Guo, E. Bell, A. Dekel, L. Porter, J. Primack, H. Ferguson, M. L. N. Ashby, K. Caputi, D. Ceverino, D. Croton, G. G. Fazio, M. Giavalisco, L. Hsu, D. Kocevski, A. Koekemoer, P. Kurczynski, P. Kollipara, J. Lee, D. H. McIntosh, E. McGrath, C. Moody, R. Somerville, C. Papovich, M. Salvato, P. Santini, T. Tal, A. van der Wel, C. C. Williams, S. P. Willner, and A. Zolotov. CANDELS+3D-HST: Compact SFGs at z ˜ 2-3, the Progenitors of the First Quiescent Galaxies. ApJ, 791:52, August 2014. doi: 10.1088/0004-637X/791/1/52.

G. Barro, S. M. Faber, D. C. Koo, A. Dekel, J. J. Fang, J. R. Trump, P. G. Perez-Gonzalez, C. Pacifici, J. R. Primack, R. S. Somerville, H. Yan, Y. Guo, F. Liu, D. Ceverino, D. D. Kocevski, and E. McGrath. A universal structural and star-forming relation since $z \sim 3$: connecting compact star-forming and quiescent galaxies. ArXiv e-prints, September 2015.

P. S. Behroozi, R. H. Wechsler, and C. Conroy. The Average Star Formation Histories of Galaxies in Dark Matter Halos from z = 0-8. ApJ, 770:57, June 2013. doi: 10.1088/0004-637X/770/1/57.

E. F. Bell, A. van der Wel, C. Papovich, D. Kocevski, J. Lotz, D. H. McIntosh, J. Kartaltepe, S. M. Faber, H. Ferguson, A. Koekemoer, N. Grogin, S. Wuyts, E. Cheung, C. J. Conselice, A. Dekel, J. S. Dunlop, M. Giavalisco, J. Herrington, D. C. Koo, E. J. McGrath, D. de Mello, H.-W. Rix,

A. R. Robaina, and C. C. Williams. What Turns Galaxies Off? The Different Morphologies of Star-forming and Quiescent Galaxies since z ˜ 2 from CANDELS. ApJ, 753:167, July 2012. doi: 10.1088/0004-637X/753/2/167.

S. Belli, A. B. Newman, and R. S. Ellis. Velocity Dispersions and Dynamical Masses for a Large Sample of Quiescent Galaxies at z 1: Improved Measures of the Growth in Mass and Size. ApJ, 783:117, March 2014. doi: 10.1088/0004-637X/783/2/117.

S. Belli, A. B. Newman, and R. S. Ellis. MOSFIRE Spectroscopy of Quiescent Galaxies at 1.5 z 2.5. I. Evolution of Structural and Dynamical Properties. ApJ, 834:18, January 2017. doi: 10.3847/1538-4357/834/1/18.

E. Bertin and S. Arnouts. SExtractor: Software for source extraction. A&AS, 117:393–404, June 1996.

R. Bezanson, D. A. Wake, G. B. Brammer, P. G. van Dokkum, M. Franx, I. Labbé, J. Leja, I. G. Momcheva, E. J. Nelson, R. F. Quadri, R. E. Skelton, B. J. Weiner, and K. E. Whitaker. Leveraging 3D-HST Grism Redshifts to Quantify Photometric Redshift Performance. ArXiv e-prints, October 2015.

A. F. L. Bluck, C. J. Conselice, F. Buitrago, R. Grützbauch, C. Hoyos, A. Mortlock, and A. E. Bauer. The Structures and Total (Minor + Major) Merger Histories of Massive Galaxies up to z ˜ 3 in the HST GOODS NICMOS Survey: A Possible Solution to the Size Evolution Problem. ApJ, 747:34, March 2012. doi: 10.1088/0004-637X/747/1/34.

F. Bournaud, B. G. Elmegreen, and D. M. Elmegreen. Rapid Formation of Exponential Disks and Bulges at High Redshift from the Dynamical Evolution of Clump-Cluster and Chain Galaxies. ApJ, 670:237–248, November 2007. doi: 10.1086/522077.

G. B. Brammer, P. G. van Dokkum, and P. Coppi. EAZY: A Fast, Public Photometric Redshift Code. ApJ, 686:1503–1513, October 2008. doi: 10.1086/591786.

V. A. Bruce, J. S. Dunlop, M. Cirasuolo, R. J. McLure, T. A. Targett, E. F. Bell, D. J. Croton, A. Dekel, S. M. Faber, H. C. Ferguson, N. A. Grogin, D. D. Kocevski, A. M. Koekemoer, D. C. Koo, K. Lai, J. M. Lotz, E. J. McGrath, J. A. Newman, and A. van der Wel. The morphologies of massive galaxies at 1 z 3 in the CANDELS-UDS field: compact bulges, and the rise and fall of massive discs. MNRAS, 427:1666–1701, December 2012. doi: 10.1111/j.1365-2966.2012.22087.x.

G. Bruzual and S. Charlot. Stellar population synthesis at the resolution of 2003. MNRAS, 344:1000–1028, October 2003. doi: 10.1046/j.1365-8711.2003.06897.x.

K. Bundy, A. Georgakakis, K. Nandra, R. S. Ellis, C. J. Conselice, E. Laird, A. Coil, M. C. Cooper, S. M. Faber, J. A. Newman, C. M. Pierce, J. R. Primack, and R. Yan. AEGIS: New Evidence

Linking Active Galactic Nuclei to the Quenching of Star Formation. ApJ, 681:931-943, July 2008. doi: 10.1086/588719.

K. Bundy, M. Fukugita, R. S. Ellis, T. A. Targett, S. Belli, and T. Kodama. The Greater Impact of Mergers on the Growth of Massive Galaxies: Implications for Mass Assembly and Evolution since z sime 1. ApJ, 697:1369–1383, June 2009. doi: 10.1088/0004-637X/697/2/1369.

A. J. Bunker. Galaxy Morphology in the GTO-NICMOS Northern Hubble Deep Field. In R. Weymann, L. Storrie-Lombardi, M. Sawicki, and R. Brunner, editors, Photometric Redshifts and the Detection of High Redshift Galaxies, volume 191 of Astronomical Society of the Pacific Conference Series, page 317, 1999.

D. Calzetti, L. Armus, R. C. Bohlin, A. L. Kinney, J. Koornneef, and T. Storchi-Bergmann. The Dust Content and Opacity of Actively Star-forming Galaxies. ApJ, 533:682–695, April 2000. doi: 10.1086/308692.

M. Cappellari, R. Bacon, M. Bureau, M. C. Damen, R. L. Davies, P. T. de Zeeuw, E. Emsellem, J. Falcón-Barroso, D. Krajnović, H. Kuntschner, R. M. McDermid, R. F. Peletier, M. Sarzi, R. C. E. van den Bosch, and G. van de Ven. The SAURON project - IV. The mass-to-light ratio, the virial mass estimator and the Fundamental Plane of elliptical and lenticular galaxies. MNRAS, 366:1126–1150, March 2006. doi: 10.1111/j.1365-2966.2005.09981.x.

M. Cappellari, R. M. McDermid, K. Alatalo, L. Blitz, M. Bois, F. Bournaud, M. Bureau, A. F. Crocker, R. L. Davies, T. A. Davis, P. T. de Zeeuw, P.-A. Duc, E. Emsellem, S. Khochfar, D. Krajnović, H. Kuntschner, P.-Y. Lablanche, R. Morganti, T. Naab, T. Oosterloo, M. Sarzi, N. Scott, P. Serra, A.-M. Weijmans, and L. M. Young. Systematic variation of the stellar initial mass function in early-type galaxies. Nature, 484:485–488, April 2012. doi: 10.1038/nature10972.

M. Cappellari, R. M. McDermid, K. Alatalo, L. Blitz, M. Bois, F. Bournaud, M. Bureau, A. F. Crocker, R. L. Davies, T. A. Davis, P. T. de Zeeuw, P.-A. Duc, E. Emsellem, S. Khochfar, D. Krajnović, H. Kuntschner, R. Morganti, T. Naab, T. Oosterloo, M. Sarzi, N. Scott, P. Serra, A.-M. Weijmans, and L. M. Young. The ATLAS^{3D} project - XX. Mass-size and mass-σ distributions of early-type galaxies: bulge fraction drives kinematics, mass-to-light ratio, molecular gas fraction and stellar initial mass function. MNRAS, 432:1862–1893, July 2013. doi: 10.1093/mnras/stt644.

J. A. Cardelli, G. C. Clayton, and J. S. Mathis. The relationship between infrared, optical, and ultraviolet extinction. ApJ, 345:245–256, October 1989. doi: 10.1086/167900.

C. M. Carollo, T. J. Bschorr, A. Renzini, S. J. Lilly, P. Capak, A. Cibinel, O. Ilbert, M. Onodera, N. Scoville, E. Cameron, B. Mobasher, D. Sanders, and Y. Taniguchi. Newly Quenched Galaxies as the Cause for the Apparent Evolution in Average Size of the Population. ApJ, 773:112, August 2013. doi: 10.1088/0004-637X/773/2/112.

P. Cassata, M. Giavalisco, C. C. Williams, Y. Guo, B. Lee, A. Renzini, H. Ferguson, S. F. Faber, G. Barro, D. H. McIntosh, Y. Lu, E. F. Bell, D. C. Koo, C. J. Papovich, R. E. Ryan, C. J. Conselice, N. Grogin, A. Koekemoer, and N. P. Hathi. Constraining the Assembly of Normal and Compact Passively Evolving Galaxies from Redshift z = 3 to the Present with CANDELS. ApJ, 775:106, October 2013. doi: 10.1088/0004-637X/775/2/106.

M. Castellano, R. Amorín, E. Merlin, A. Fontana, R. J. McLure, E. Mármol-Queraltó, A. Mortlock, S. Parsa, J. S. Dunlop, D. Elbaz, I. Balestra, A. Boucaud, N. Bourne, K. Boutsia, G. Brammer, V. A. Bruce, F. Buitrago, P. Capak, N. Cappelluti, L. Ciesla, A. Comastri, F. Cullen, S. Derriere, S. M. Faber, E. Giallongo, A. Grazian, C. Grillo, A. Mercurio, M. J. Michałowski, M. Nonino, D. Paris, L. Pentericci, S. Pilo, P. Rosati, P. Santini, C. Schreiber, X. Shu, and T. Wang. The ASTRODEEP Frontier Fields Catalogues: II - Photometric redshifts and rest-frame properties in Abell-2744 and MACS-J0416. ArXiv e-prints, March 2016.

G. Chabrier. Galactic Stellar and Substellar Initial Mass Function. PASP, 115:763–795, July 2003. doi: 10.1086/376392.

E. Cheung, S. M. Faber, D. C. Koo, A. A. Dutton, L. Simard, E. J. McGrath, J.-S. Huang, E. F. Bell, A. Dekel, J. J. Fang, S. Salim, G. Barro, K. Bundy, A. L. Coil, M. C. Cooper, C. J. Conselice, M. Davis, A. Domínguez, S. A. Kassin, D. D. Kocevski, A. M. Koekemoer, L. Lin, J. M. Lotz, J. A. Newman, A. C. Phillips, D. J. Rosario, B. J. Weiner, and C. N. A. Willmer. The Dependence of Quenching upon the Inner Structure of Galaxies at 0.5 = z 0.8 in the DEEP2/AEGIS Survey. ApJ, 760:131, December 2012. doi: 10.1088/0004-637X/760/2/131.

E. Cheung, K. Bundy, M. Cappellari, S. Peirani, W. Rujopakarn, K. Westfall, R. Yan, M. Bershady, J. E. Greene, T. M. Heckman, N. Drory, D. R. Law, K. L. Masters, D. Thomas, D. A. Wake, A.-M. Weijmans, K. Rubin, F. Belfiore, B. Vulcani, Y.-M. Chen, K. Zhang, J. D. Gelfand, D. Bizyaev, A. Roman-Lopes, and D. P. Schneider. Suppressing star formation in quiescent galaxies with supermassive black hole winds. Nature, 533:504–508, May 2016. doi: 10.1038/nature18006.

J. Choi, C. Conroy, J. Moustakas, G. J. Graves, B. P. Holden, M. Brodwin, M. J. I. Brown, and P. G. van Dokkum. The Assembly Histories of Quiescent Galaxies since z = 0.7 from Absorption Line Spectroscopy. ApJ, 792:95, September 2014. doi: 10.1088/0004-637X/792/2/95.

A. Cimatti, P. Cassata, L. Pozzetti, J. Kurk, M. Mignoli, A. Renzini, E. Daddi, M. Bolzonella, M. Brusa, G. Rodighiero, M. Dickinson, A. Franceschini, G. Zamorani, S. Berta, P. Rosati, and C. Halliday. GMASS ultradeep spectroscopy of galaxies at z ˜ 2. II. Superdense passive galaxies: how did they form and evolve? A&A, 482:21–42, April 2008. doi: 10.1051/0004-6361:20078739.

L. Ciotti, B. Lanzoni, and M. Volonteri. The Importance of Dry and Wet Merging on the Formation and Evolution of Elliptical Galaxies. ApJ, 658:65–77, March 2007. doi: 10.1086/510773.

C. Conroy and R. H. Wechsler. Connecting Galaxies, Halos, and Star Formation Rates Across Cosmic Time. ApJ, 696:620–635, May 2009. doi: 10.1088/0004-637X/696/1/620.

C. Conroy, G. J. Graves, and P. G. van Dokkum. Early-type Galaxy Archeology: Ages, Abundance Ratios, and Effective Temperatures from Full-spectrum Fitting. ApJ, 780:33, January 2014. doi: 10.1088/0004-637X/780/1/33.

C. J. Conselice, J. A. Blackburne, and C. Papovich. The Luminosity, Stellar Mass, and Number Density Evolution of Field Galaxies of Known Morphology from z = 0.5 to 3. ApJ, 620:564–583, February 2005. doi: 10.1086/426102.

M. Covington, A. Dekel, T. J. Cox, P. Jonsson, and J. R. Primack. Predicting the properties of the remnants of dissipative galaxy mergers. MNRAS, 384:94–106, February 2008. doi: 10.1111/j.1365-2966.2007.12601.x.

E. Daddi, A. Renzini, N. Pirzkal, A. Cimatti, S. Malhotra, M. Stiavelli, C. Xu, A. Pasquali, J. E. Rhoads, M. Brusa, S. di Serego Alighieri, H. C. Ferguson, A. M. Koekemoer, L. A. Moustakas, N. Panagia, and R. A. Windhorst. Passively Evolving Early-Type Galaxies at 1.4 ˜ z ˜ 2.5 in the Hubble Ultra Deep Field. ApJ, 626:680–697, June 2005. doi: 10.1086/430104.

E. Daddi, D. M. Alexander, M. Dickinson, R. Gilli, A. Renzini, D. Elbaz, A. Cimatti, R. Chary, D. Frayer, F. E. Bauer, W. N. Brandt, M. Giavalisco, N. A. Grogin, M. Huynh, J. Kurk, M. Mignoli, G. Morrison, A. Pope, and S. Ravindranath. Multiwavelength Study of Massive Galaxies at z˜2. II. Widespread Compton-thick Active Galactic Nuclei and the Concurrent Growth of Black Holes and Bulges. ApJ, 670:173–189, November 2007. doi: 10.1086/521820.

I. Damjanov, P. J. McCarthy, R. G. Abraham, K. Glazebrook, H. Yan, E. Mentuch, D. Le Borgne, S. Savaglio, D. Crampton, R. Murowinski, S. Juneau, R. G. Carlberg, I. Jørgensen, K. Roth, H.-W. Chen, and R. O. Marzke. Red Nuggets at z ˜ 1.5: Compact Passive Galaxies and the Formation of the Kormendy Relation. ApJ, 695:101–115, April 2009. doi: 10.1088/0004-637X/695/1/101.

I. Damjanov, M. J. Geller, H. J. Zahid, and H. S. Hwang. Quiescent Compact Galaxies at Intermediate Redshift in the COSMOS Field. The Number Density. ApJ, 806:158, June 2015. doi: 10.1088/0004-637X/806/2/158.

I. G. de la Rosa, F. La Barbera, I. Ferreras, J. Sánchez Almeida, C. Dalla Vecchia, I. Martínez-Valpuesta, and M. Stringer. The fate of high-redshift massive compact galaxies. MNRAS, 457:1916–1930, April 2016. doi: 10.1093/mnras/stw130.

A. Dekel and Y. Birnboim. Galaxy bimodality due to cold flows and shock heating. MNRAS, 368:2–20, May 2006. doi: 10.1111/j.1365-2966.2006.10145.x.

A. Dekel and A. Burkert. Wet disc contraction to galactic blue nuggets and quenching to red nuggets. MNRAS, 438:1870–1879, February 2014. doi: 10.1093/mnras/stt2331.

M. Dickinson. The first galaxies: structure and stellar populations. In Astronomy, physics and chemistry of H^+_3, volume 358 of Royal Society of London Philosophical Transactions Series A, page 2001, July 2000. doi: 10.1098/rsta.2000.0626.

M. Dickinson, M. Giavalisco, and GOODS Team. The Great Observatories Origins Deep Survey. In R. Bender and A. Renzini, editors, The Mass of Galaxies at Low and High Redshift, page 324, 2003. doi: 10.1007/10899892_78.

S. Djorgovski and M. Davis. Fundamental properties of elliptical galaxies. ApJ, 313:59–68, February 1987. doi: 10.1086/164948.

A. Dressler. Galaxy morphology in rich clusters - Implications for the formation and evolution of galaxies. ApJ, 236:351–365, March 1980. doi: 10.1086/157753.

A. Dressler, D. Lynden-Bell, D. Burstein, R. L. Davies, S. M. Faber, R. Terlevich, and G. Wegner. Spectroscopy and photometry of elliptical galaxies. I - A new distance estimator. ApJ, 313: 42–58, February 1987. doi: 10.1086/164947.

A. Dressler, D. D. Kelson, L. E. Abramson, M. D. Gladders, A. Oemler, Jr., B. M. Poggianti, J. S. Mulchaey, B. Vulcani, S. A. Shectman, R. J. Williams, and P. J. McCarthy. Demonstrating Diversity in Star Formation Histories with the CSI Survey. ArXiv e-prints, July 2016.

O. J. Eggen, D. Lynden-Bell, and A. R. Sandage. Evidence from the motions of old stars that the Galaxy collapsed. ApJ, 136:748, November 1962. doi: 10.1086/147433.

D. Elbaz, M. Dickinson, H. S. Hwang, T. Díaz-Santos, G. Magdis, B. Magnelli, D. Le Borgne, F. Galliano, M. Pannella, P. Chanial, L. Armus, V. Charmandaris, E. Daddi, H. Aussel, P. Popesso, J. Kartaltepe, B. Altieri, I. Valtchanov, D. Coia, H. Dannerbauer, K. Dasyra, R. Leiton, J. Mazzarella, D. M. Alexander, V. Buat, D. Burgarella, R.-R. Chary, R. Gilli, R. J. Ivison, S. Juneau, E. Le Floc'h, D. Lutz, G. E. Morrison, J. R. Mullaney, E. Murphy, A. Pope, D. Scott, M. Brodwin, D. Calzetti, C. Cesarsky, S. Charlot, H. Dole, P. Eisenhardt, H. C. Ferguson, N. Förster Schreiber, D. Frayer, M. Giavalisco, M. Huynh, A. M. Koekemoer, C. Papovich, N. Reddy, C. Surace, H. Teplitz, M. S. Yun, and G. Wilson. GOODS-Herschel: an infrared main sequence for star-forming galaxies. A&A, 533:A119, September 2011. doi: 10.1051/0004-6361/201117239.

S. M. Faber and R. E. Jackson. Velocity dispersions and mass-to-light ratios for elliptical galaxies. ApJ, 204:668–683, March 1976. doi: 10.1086/154215.

L. Fan, A. Lapi, G. De Zotti, and L. Danese. The Dramatic Size Evolution of Elliptical Galaxies and the Quasar Feedback. ApJ, 689:L101–L104, December 2008. doi: 10.1086/595784.

L. Ferrarese, F. C. van den Bosch, H. C. Ford, W. Jaffe, and R. W. O'Connell. Hubble Space Telescope photometry of the central regions of Virgo cluster elliptical galaxies. 3: Brightness profiles. AJ, 108:1598–1609, November 1994. doi: 10.1086/117180.

M. Franx, P. G. van Dokkum, N. M. F. Schreiber, S. Wuyts, I. Labbé, and S. Toft. Structure and Star Formation in Galaxies out to z = 3: Evidence for Surface Density Dependent Evolution and Upsizing. ApJ, 688:770–788, December 2008. doi: 10.1086/592431.

M. Fukugita, T. Ichikawa, J. E. Gunn, M. Doi, K. Shimasaku, and D. P. Schneider. The Sloan Digital Sky Survey Photometric System. AJ, 111:1748, April 1996. doi: 10.1086/117915.

R. Genzel, L. J. Tacconi, J. Gracia-Carpio, A. Sternberg, M. C. Cooper, K. Shapiro, A. Bolatto, N. Bouché, F. Bournaud, A. Burkert, F. Combes, J. Comerford, P. Cox, M. Davis, N. M. F. Schreiber, S. Garcia-Burillo, D. Lutz, T. Naab, R. Neri, A. Omont, A. Shapley, and B. Weiner. A study of the gas-star formation relation over cosmic time. MNRAS, 407:2091–2108, October 2010. doi: 10.1111/j.1365-2966.2010.16969.x.

R. Genzel, N. M. Förster Schreiber, P. Lang, S. Tacchella, L. J. Tacconi, S. Wuyts, K. Bandara, A. Burkert, P. Buschkamp, C. M. Carollo, G. Cresci, R. Davies, F. Eisenhauer, E. K. S. Hicks, J. Kurk, S. J. Lilly, D. Lutz, C. Mancini, T. Naab, S. Newman, Y. Peng, A. Renzini, K. Shapiro Griffin, A. Sternberg, D. Vergani, E. Wisnioski, E. Wuyts, and G. Zamorani. The SINS/zC-SINF Survey of z ˜ 2 Galaxy Kinematics: Evidence for Gravitational Quenching. ApJ, 785:75, April 2014. doi: 10.1088/0004-637X/785/1/75.

K. Glazebrook, C. Schreiber, I. Labbé, T. Nanayakkara, G. G. Kacprzak, P. A. Oesch, C. Papovich, L. R. Spitler, C. M. S. Straatman, K.-V. H. Tran, and T. Yuan. A massive, quiescent galaxy at a redshift of 3.717. Nature, 544:71–74, April 2017. doi: 10.1038/nature21680.

Fruchter A. Gonzaga, S. H. W. and J. Mack. The DrizzlePac Handbook. Baltimore, STScI, 2011.

N. A. Grogin, D. D. Kocevski, S. M. Faber, H. C. Ferguson, A. M. Koekemoer, A. G. Riess, V. Acquaviva, D. M. Alexander, O. Almaini, M. L. N. Ashby, M. Barden, E. F. Bell, F. Bournaud, T. M. Brown, K. I. Caputi, S. Casertano, P. Cassata, M. Castellano, P. Challis, R.-R. Chary, E. Cheung, M. Cirasuolo, C. J. Conselice, A. Roshan Cooray, D. J. Croton, E. Daddi, T. Dahlen, R. Davé, D. F. de Mello, A. Dekel, M. Dickinson, T. Dolch, J. L. Donley, J. S. Dunlop, A. A. Dutton, D. Elbaz, G. G. Fazio, A. V. Filippenko, S. L. Finkelstein, A. Fontana, J. P. Gardner, P. M. Garnavich, E. Gawiser, M. Giavalisco, A. Grazian, Y. Guo, N. P. Hathi, B. Häussler, P. F. Hopkins, J.-S. Huang, K.-H. Huang, S. W. Jha, J. S. Kartaltepe, R. P. Kirshner, D. C. Koo, K. Lai, K.-S. Lee, W. Li, J. M. Lotz, R. A. Lucas, P. Madau, P. J. McCarthy, E. J. McGrath, D. H. McIntosh, R. J. McLure, B. Mobasher, L. A. Moustakas, M. Mozena, K. Nandra, J. A. Newman, S.-M. Niemi, K. G. Noeske, C. J. Papovich, L. Pentericci, A. Pope, J. R. Primack, A. Rajan, S. Ravindranath, N. A. Reddy, A. Renzini, H.-W. Rix, A. R. Robaina, S. A. Rodney, D. J. Rosario, P. Rosati, S. Salimbeni, C. Scarlata, B. Siana, L. Simard, J. Smidt, R. S. Somerville, H. Spinrad, A. N. Straughn, L.-G. Strolger, O. Telford, H. I. Teplitz, J. R. Trump, A. van der Wel, C. Villforth, R. H. Wechsler, B. J. Weiner, T. Wiklind, V. Wild, G. Wilson, S. Wuyts, H.-J. Yan, and M. S. Yun. CANDELS: The Cosmic Assembly Near-infrared Deep Extragalactic Legacy Survey. ApJS, 197:35, December 2011. doi: 10.1088/0067-0049/197/2/35.

Q. Guo, S. White, C. Li, and M. Boylan-Kolchin. How do galaxies populate dark matter haloes? MNRAS, 404:1111–1120, May 2010. doi: 10.1111/j.1365-2966.2010.16341.x.

Y. Guo, D. H. McIntosh, H. J. Mo, N. Katz, F. C. van den Bosch, M. Weinberg, S. M. Weinmann, A. Pasquali, and X. Yang. Structural properties of central galaxies in groups and clusters. MNRAS, 398:1129–1149, September 2009. doi: 10.1111/j.1365-2966.2009.15223.x.

Y. Guo, H. C. Ferguson, E. F. Bell, D. C. Koo, C. J. Conselice, M. Giavalisco, S. Kassin, Y. Lu, R. Lucas, N. Mandelker, D. M. McIntosh, J. R. Primack, S. Ravindranath, G. Barro, D. Ceverino, A. Dekel, S. M. Faber, J. J. Fang, A. M. Koekemoer, K. Noeske, M. Rafelski, and A. Straughn. Clumpy Galaxies in CANDELS. I. The Definition of UV Clumps and the Fraction of Clumpy Galaxies at 0.5 z 3. ApJ, 800:39, February 2015. doi: 10.1088/0004-637X/800/1/39.

N. Häring and H.-W. Rix. On the Black Hole Mass-Bulge Mass Relation. ApJ, 604:L89–L92, April 2004. doi: 10.1086/383567.

B. Häußler, D. H. McIntosh, M. Barden, E. F. Bell, H.-W. Rix, A. Borch, S. V. W. Beckwith, J. A. R. Caldwell, C. Heymans, K. Jahnke, S. Jogee, S. E. Koposov, K. Meisenheimer, S. F. Sánchez, R. S. Somerville, L. Wisotzki, and C. Wolf. GEMS: Galaxy Fitting Catalogs and Testing Parametric Galaxy Fitting Codes: GALFIT and GIM2D. ApJS, 172:615–633, October 2007. doi: 10.1086/518836.

B. Häußler, S. P. Bamford, M. Vika, A. L. Rojas, M. Barden, L. S. Kelvin, M. Alpaslan, A. S. G. Robotham, S. P. Driver, I. K. Baldry, S. Brough, A. M. Hopkins, J. Liske, R. C. Nichol, C. C. Popescu, and R. J. Tuffs. MegaMorph - multiwavelength measurement of galaxy structure: complete Sérsic profile information from modern surveys. MNRAS, 430:330–369, March 2013. doi: 10.1093/mnras/sts633.

K. Hayashi and M. Chiba. The Prolate Dark Matter Halo of the Andromeda Galaxy. ApJ, 789:62, July 2014. doi: 10.1088/0004-637X/789/1/62.

M. Hayashi, T. Kodama, K.-i. Tadaki, Y. Koyama, and I. Tanaka. A Starbursting Proto-cluster in Making Associated with a Radio Galaxy at z = 2.53 Discovered by Hα Imaging. ApJ, 757:15, September 2012. doi: 10.1088/0004-637X/757/1/15.

A. Heavens, B. Panter, R. Jimenez, and J. Dunlop. The star-formation history of the Universe from the stellar populations of nearby galaxies. Nature, 428:625–627, April 2004. doi: 10.1038/nature02474.

J. A. Högbom. Aperture Synthesis with a Non-Regular Distribution of Interferometer Baselines. A&AS, 15:417, June 1974.

D. W. Hogg, M. R. Blanton, D. J. Eisenstein, J. E. Gunn, D. J. Schlegel, I. Zehavi, N. A. Bahcall, J. Brinkmann, I. Csabai, D. P. Schneider, D. H. Weinberg, and D. G. York. The Overdensities

of Galaxy Environments as a Function of Luminosity and Color. ApJ, 585:L5–L9, March 2003. doi: 10.1086/374238.

P. F. Hopkins, L. Hernquist, T. J. Cox, T. Di Matteo, B. Robertson, and V. Springel. A Unified, Merger-driven Model of the Origin of Starbursts, Quasars, the Cosmic X-Ray Background, Supermassive Black Holes, and Galaxy Spheroids. ApJS, 163:1–49, March 2006. doi: 10.1086/499298.

P. F. Hopkins, L. Hernquist, T. J. Cox, D. Keres, and S. Wuyts. Dissipation and Extra Light in Galactic Nuclei. IV. Evolution in the Scaling Relations of Spheroids. ApJ, 691:1424–1458, February 2009a. doi: 10.1088/0004-637X/691/2/1424.

P. F. Hopkins, L. Hernquist, T. J. Cox, D. Keres, and S. Wuyts. Dissipation and Extra Light in Galactic Nuclei. IV. Evolution in the Scaling Relations of Spheroids. ApJ, 691:1424–1458, February 2009b. doi: 10.1088/0004-637X/691/2/1424.

T. Ichikawa, R. Suzuki, C. Tokoku, Y. K. Uchimoto, M. Konishi, T. Yoshikawa, T. Yamada, I. Tanaka, K. Omata, and T. Nishimura. MOIRCS: multi-object infrared camera and spectrograph for SUBARU. In Society of Photo-Optical Instrumentation Engineers (SPIE) Conference Series, volume 6269 of Society of Photo-Optical Instrumentation Engineers (SPIE) Conference Series, July 2006. doi: 10.1117/12.670078.

T. Ichikawa, R. Suzuki, C. Tokoku, Y. K. Uchimoto, M. Konishi, T. Yoshikawa, M. Kajisawa, M. Ouchi, T. Hamana, M. Akiyama, T. Nishimura, K. Omata, I. Tanaka, and T. Yamada. MOIRCS Deep Survey. II. Clustering Properties of K-Band Selected Galaxies in GOODS-North Region. PASJ, 59:1081–, December 2007. doi: 10.1093/pasj/59.6.1081.

G. D. Illingworth, D. Magee, P. A. Oesch, R. J. Bouwens, I. Labbé, M. Stiavelli, P. G. van Dokkum, M. Franx, M. Trenti, C. M. Carollo, and V. Gonzalez. The HST eXtreme Deep Field (XDF): Combining All ACS and WFC3/IR Data on the HUDF Region into the Deepest Field Ever. ApJS, 209:6, November 2013. doi: 10.1088/0067-0049/209/1/6.

P. H. Johansson, T. Naab, and J. P. Ostriker. Gravitational Heating Helps Make Massive Galaxies Red and Dead. ApJ, 697:L38–L43, May 2009. doi: 10.1088/0004-637X/697/1/L38.

M. Kajisawa and T. Yamada. When Did the Hubble Sequence Appear?: Morphology, Color, and Number-Density Evolution of the Galaxies in the Hubble Deep Field North. PASJ, 53:833–852, October 2001.

M. Kajisawa, T. Ichikawa, I. Tanaka, M. Konishi, T. Yamada, M. Akiyama, R. Suzuki, C. Tokoku, Y. K. Uchimoto, T. Yoshikawa, M. Ouchi, I. Iwata, T. Hamana, and M. Onodera. MOIRCS Deep Survey. IV. Evolution of Galaxy Stellar Mass Function Back to z ˜ 3. ApJ, 702:1393–1412, September 2009. doi: 10.1088/0004-637X/702/2/1393.

M. Kajisawa, T. Ichikawa, I. Tanaka, T. Yamada, M. Akiyama, R. Suzuki, C. Tokoku, Y. Katsuno Uchimoto, M. Konishi, T. Yoshikawa, T. Nishimura, K. Omata, M. Ouchi, I. Iwata, T. Hamana, and M. Onodera. MOIRCS Deep Survey. IX. Deep Near-Infrared Imaging Data and Source Catalog. PASJ, 63:379–, March 2011a.

M. Kajisawa, T. Ichikawa, T. Yoshikawa, T. Yamada, M. Onodera, M. Akiyama, and I. Tanaka. MOIRCS Deep Survey. X. Evolution of Quiescent Galaxies as a Function of Stellar Mass at 0.5 z 2.5. PASJ, 63:403–, March 2011b.

D. Kashino, J. D. Silverman, G. Rodighiero, A. Renzini, N. Arimoto, E. Daddi, S. J. Lilly, D. B. Sanders, J. Kartaltepe, H. J. Zahid, T. Nagao, N. Sugiyama, P. Capak, C. M. Carollo, J. Chu, G. Hasinger, O. Ilbert, M. Kajisawa, L. J. Kewley, A. M. Koekemoer, K. Kovač, O. Le Fèvre, D. Masters, H. J. McCracken, M. Onodera, N. Scoville, V. Strazzullo, M. Symeonidis, and Y. Taniguchi. The FMOS-COSMOS Survey of Star-forming Galaxies at z ˜ 1.6. I. Hα-based Star Formation Rates and Dust Extinction. ApJ, 777:L8, November 2013. doi: 10.1088/2041-8205/777/1/L8.

L. Kawinwanichakij, C. Papovich, R. F. Quadri, K.-V. H. Tran, L. R. Spitler, G. G. Kacprzak, I. Labbé, C. M. S. Straatman, K. Glazebrook, R. Allen, M. Cowley, R. Davé, A. Dekel, H. C. Ferguson, W. G. Hartley, A. M. Koekemoer, D. C. Koo, Y. Lu, N. Mehrtens, T. Nanayakkara, S. E. Persson, G. Rees, B. Salmon, V. Tilvi, A. R. Tomczak, and P. van Dokkum. The Distribution of Satellites around Massive Galaxies at 1 z 3 in ZFOURGE/CANDELS: Dependence on Star Formation Activity. ApJ, 792:103, September 2014. doi: 10.1088/0004-637X/792/2/103.

R. C. Kennicutt and N. J. Evans. Star Formation in the Milky Way and Nearby Galaxies. ARA&A, 50:531–608, September 2012. doi: 10.1146/annurev-astro-081811-125610.

R. C. Kennicutt, Jr. Star Formation in Galaxies Along the Hubble Sequence. ARA&A, 36:189–232, 1998. doi: 10.1146/annurev.astro.36.1.189.

A. M. Koekemoer, S. M. Faber, H. C. Ferguson, N. A. Grogin, D. D. Kocevski, D. C. Koo, K. Lai, J. M. Lotz, R. A. Lucas, E. J. McGrath, S. Ogaz, A. Rajan, A. G. Riess, S. A. Rodney, L. Strolger, S. Casertano, M. Castellano, T. Dahlen, M. Dickinson, T. Dolch, A. Fontana, M. Giavalisco, A. Grazian, Y. Guo, N. P. Hathi, K.-H. Huang, A. van der Wel, H.-J. Yan, V. Acquaviva, D. M. Alexander, O. Almaini, M. L. N. Ashby, M. Barden, E. F. Bell, F. Bournaud, T. M. Brown, K. I. Caputi, P. Cassata, P. J. Challis, R.-R. Chary, E. Cheung, M. Cirasuolo, C. J. Conselice, A. Roshan Cooray, D. J. Croton, E. Daddi, R. Davé, D. F. de Mello, L. de Ravel, A. Dekel, J. L. Donley, J. S. Dunlop, A. A. Dutton, D. Elbaz, G. G. Fazio, A. V. Filippenko, S. L. Finkelstein, C. Frazer, J. P. Gardner, P. M. Garnavich, E. Gawiser, R. Gruetzbauch, W. G. Hartley, B. Häussler, J. Herrington, P. F. Hopkins, J.-S. Huang, S. W. Jha, A. Johnson, J. S. Kartaltepe, A. A. Khostovan, R. P. Kirshner, C. Lani, K.-S. Lee, W. Li, P. Madau, P. J. McCarthy, D. H. McIntosh, R. J. McLure, C. McPartland, B. Mobasher, H. Moreira, A. Mortlock, L. A. Moustakas, M. Mozena, K. Nandra, J. A. Newman, J. L. Nielsen, S. Niemi, K. G. Noeske, C. J.

Papovich, L. Pentericci, A. Pope, J. R. Primack, S. Ravindranath, N. A. Reddy, A. Renzini, H.-W. Rix, A. R. Robaina, D. J. Rosario, P. Rosati, S. Salimbeni, C. Scarlata, B. Siana, L. Simard, J. Smidt, D. Snyder, R. S. Somerville, H. Spinrad, A. N. Straughn, O. Telford, H. I. Teplitz, J. R. Trump, C. Vargas, C. Villforth, C. R. Wagner, P. Wandro, R. H. Wechsler, B. J. Weiner, T. Wiklind, V. Wild, G. Wilson, S. Wuyts, and M. S. Yun. CANDELS: The Cosmic Assembly Near-infrared Deep Extragalactic Legacy SurveyThe Hubble Space Telescope Observations, Imaging Data Products, and Mosaics. ApJS, 197:36, December 2011. doi: 10.1088/0067-0049/197/2/36.

J. Kormendy and G. Illingworth. The L varies as sigma to the N power relation for the bulge components of disk galaxies. ApJ, 265:632–642, February 1983. doi: 10.1086/160709.

Y. Koyama, T. Kodama, K.-i. Tadaki, M. Hayashi, I. Tanaka, and R. Shimakawa. The Environmental Impacts on the Star Formation Main Sequence: An Hα Study of the Newly Discovered Rich Cluster at z = 1.52. ApJ, 789:18, July 2014. doi: 10.1088/0004-637X/789/1/18.

M. Kriek, P. G. van Dokkum, I. Labbé, M. Franx, G. D. Illingworth, D. Marchesini, and R. F. Quadri. An Ultra-Deep Near-Infrared Spectrum of a Compact Quiescent Galaxy at z = 2.2. ApJ, 700:221–231, July 2009. doi: 10.1088/0004-637X/700/1/221.

J. Krist. Simulation of HST PSFs using Tiny Tim. In R. A. Shaw, H. E. Payne, and J. J. E. Hayes, editors, Astronomical Data Analysis Software and Systems IV, volume 77 of Astronomical Society of the Pacific Conference Series, page 349, 1995.

P. Kroupa. On the variation of the initial mass function. MNRAS, 322:231–246, April 2001. doi: 10.1046/j.1365-8711.2001.04022.x.

H. Kuntschner, E. Emsellem, R. Bacon, M. Cappellari, R. L. Davies, P. T. de Zeeuw, J. Falcón-Barroso, D. Krajnović, R. M. McDermid, R. F. Peletier, M. Sarzi, K. L. Shapiro, R. C. E. van den Bosch, and G. van de Ven. The SAURON project - XVII. Stellar population analysis of the absorption line strength maps of 48 early-type galaxies. MNRAS, 408:97–132, October 2010. doi: 10.1111/j.1365-2966.2010.17161.x.

I. Labbé, G. Rudnick, M. Franx, E. Daddi, P. G. van Dokkum, N. M. Förster Schreiber, K. Kuijken, A. Moorwood, H.-W. Rix, H. Röttgering, I. Trujillo, A. van der Wel, P. van der Werf, and L. van Starkenburg. Large Disklike Galaxies at High Redshift. ApJ, 591:L95–L98, July 2003. doi: 10.1086/377149.

R. B. Larson. Models for the formation of elliptical galaxies. MNRAS, 173:671–699, December 1975. doi: 10.1093/mnras/173.3.671.

J. Leja, P. G. van Dokkum, M. Franx, and K. E. Whitaker. Reconciling the Observed Star-forming Sequence with the Observed Stellar Mass Function. ApJ, 798:115, January 2015. doi: 10.1088/0004-637X/798/2/115.

J. M. Lotz, J. Primack, and P. Madau. A New Nonparametric Approach to Galaxy Morphological Classification. AJ, 128:163–182, July 2004. doi: 10.1086/421849.

J. M. Lotz, P. Jonsson, T. J. Cox, D. Croton, J. R. Primack, R. S. Somerville, and K. Stewart. The Major and Minor Galaxy Merger Rates at z 1.5. ApJ, 742:103, December 2011. doi: 10.1088/0004-637X/742/2/103.

J. M. Lotz, A. Koekemoer, D. Coe, N. Grogin, P. Capak, J. Mack, J. Anderson, R. Avila, E. A. Barker, D. Borncamp, G. Brammer, M. Durbin, H. Gunning, B. Hilbert, H. Jenkner, H. Khandrika, Z. Levay, R. A. Lucas, J. MacKenty, S. Ogaz, B. Porterfield, N. Reid, M. Robberto, P. Royle, L. J. Smith, L. J. Storrie-Lombardi, B. Sunnquist, J. Surace, D. C. Taylor, R. Williams, J. Bullock, M. Dickinson, S. Finkelstein, P. Natarajan, J. Richard, B. Robertson, J. Tumlinson, A. Zitrin, K. Flanagan, K. Sembach, B. T. Soifer, and M. Mountain. The Frontier Fields: Survey Design and Initial Results. ApJ, 837:97, March 2017. doi: 10.3847/1538-4357/837/1/97.

P. Madau and M. Dickinson. Cosmic Star-Formation History. ARA&A, 52:415–486, August 2014. doi: 10.1146/annurev-astro-081811-125615.

J. Magorrian, S. Tremaine, D. Richstone, R. Bender, G. Bower, A. Dressler, S. M. Faber, K. Gebhardt, R. Green, C. Grillmair, J. Kormendy, and T. Lauer. The Demography of Massive Dark Objects in Galaxy Centers. AJ, 115:2285–2305, June 1998. doi: 10.1086/300353.

F. Mannucci, G. Cresci, R. Maiolino, A. Marconi, and A. Gnerucci. A fundamental relation between mass, star formation rate and metallicity in local and high-redshift galaxies. MNRAS, 408:2115–2127, November 2010. doi: 10.1111/j.1365-2966.2010.17291.x.

C. Maraston, J. Pforr, A. Renzini, E. Daddi, M. Dickinson, A. Cimatti, and C. Tonini. Star formation rates and masses of z ˜ 2 galaxies from multicolour photometry. MNRAS, 407:830–845, September 2010. doi: 10.1111/j.1365-2966.2010.16973.x.

E. Mármol-Queraltó, I. Trujillo, P. G. Pérez-González, J. Varela, and G. Barro. Satellites around massive galaxies since z
2. MNRAS, 422:2187–2194, May 2012. doi: 10.1111/j.1365-2966.2012.20765.x.

Z. C. Marsan, D. Marchesini, G. B. Brammer, M. Stefanon, A. Muzzin, A. Fernández-Soto, S. Geier, K. N. Hainline, H. Intema, A. Karim, I. Labbé, S. Toft, and P. G. van Dokkum. Spectroscopic Confirmation of an Ultra Massive and Compact Galaxy at z = 3.35: a Detailed Look at an Early Progenitor of Local Giant Ellipticals. ApJ, 801:133, March 2015. doi: 10.1088/0004-637X/801/2/133.

M. Martig, F. Bournaud, R. Teyssier, and A. Dekel. Morphological Quenching of Star Formation: Making Early-Type Galaxies Red. ApJ, 707:250–267, December 2009. doi: 10.1088/0004-637X/707/1/250.

R. M. McDermid, K. Alatalo, L. Blitz, F. Bournaud, M. Bureau, M. Cappellari, A. F. Crocker, R. L. Davies, T. A. Davis, P. T. de Zeeuw, P.-A. Duc, E. Emsellem, S. Khochfar, D. Krajnović, H. Kuntschner, R. Morganti, T. Naab, T. Oosterloo, M. Sarzi, N. Scott, P. Serra, A.-M. Weijmans, and L. M. Young. The ATLAS^{3D} Project - XXX. Star formation histories and stellar population scaling relations of early-type galaxies. MNRAS, 448:3484–3513, April 2015. doi: 10.1093/mnras/stv105.

I. G. Momcheva, G. B. Brammer, P. G. van Dokkum, R. E. Skelton, K. E. Whitaker, E. J. Nelson, M. Fumagalli, M. V. Maseda, J. Leja, M. Franx, H.-W. Rix, R. Bezanson, E. Da Cunha, C. Dickey, N. M. Förster Schreiber, G. Illingworth, M. Kriek, I. Labbé, J. Ulf Lange, B. F. Lundgren, D. Magee, D. Marchesini, P. Oesch, C. Pacifici, S. G. Patel, S. Price, T. Tal, D. A. Wake, A. van der Wel, and S. Wuyts. The 3D-HST Survey: Hubble Space Telescope WFC3/G141 Grism Spectra, Redshifts, and Emission Line Measurements for ˜ 100,000 Galaxies. ApJS, 225: 27, August 2016. doi: 10.3847/0067-0049/225/2/27.

T. Morishita and T. Ichikawa. The Fate of a Red Nugget: In Situ Star Formation of Satellites around a Massive Compact Galaxy. ApJ, 816:87, January 2016. doi: 10.3847/0004-637X/816/2/87.

T. Morishita, T. Ichikawa, and M. Kajisawa. The Evolution of Galaxy Size and Morphology at z ˜ 0.5-3.0 in the GOODS-N Region with Hubble Space Telescope/WFC3 Data. ApJ, 785:18, April 2014. doi: 10.1088/0004-637X/785/1/18.

T. Morishita, T. Ichikawa, M. Noguchi, M. Akiyama, S. G. Patel, M. Kajisawa, and T. Obata. From Diversity to Dichotomy, and Quenching: Milky-Way-like and Massive Galaxy Progenitors at 0.5 z 3.0. ApJ, 805:34, May 2015. doi: 10.1088/0004-637X/805/1/34.

T. Morishita, L. E. Abramson, T. Treu, B. Vulcani, K. B. Schmidt, A. Dressler, B. M. Poggianti, M. A. Malkan, X. Wang, K.-H. Huang, M. Trenti, M. Bradač, and A. Hoag. The Grism Lens-amplified Survey from Space (Glass). IX. The Dual Origin of Low-mass Cluster Galaxies as Revealed by New Structural Analyses. ApJ, 835:254, February 2017. doi: 10.3847/1538-4357/835/2/254.

M. Mosleh, R. J. Williams, and M. Franx. On the Robustness of z = 0-1 Galaxy Size Measurements through Model and Non-parametric Fits. ApJ, 777:117, November 2013. doi: 10.1088/0004-637X/777/2/117.

B. P. Moster, T. Naab, and S. D. M. White. Galactic star formation and accretion histories from matching galaxies to dark matter haloes. MNRAS, 428:3121–3138, February 2013. doi: 10.1093/mnras/sts261.

T. Naab, P. H. Johansson, J. P. Ostriker, and G. Efstathiou. Formation of Early-Type Galaxies from Cosmological Initial Conditions. ApJ, 658:710–720, April 2007. doi: 10.1086/510841.

T. Naab, P. H. Johansson, and J. P. Ostriker. Minor Mergers and the Size Evolution of Elliptical Galaxies. ApJ, 699:L178–L182, July 2009. doi: 10.1088/0004-637X/699/2/L178.

E. Nelson, P. van Dokkum, M. Franx, G. Brammer, I. Momcheva, N. F. Schreiber, E. da Cunha, L. Tacconi, R. Bezanson, A. Kirkpatrick, J. Leja, H.-W. Rix, R. Skelton, A. van der Wel, K. Whitaker, and S. Wuyts. A massive galaxy in its core formation phase three billion years after the Big Bang. Nature, 513:394–397, September 2014. doi: 10.1038/nature13616.

A. B. Newman, R. S. Ellis, K. Bundy, and T. Treu. Can Minor Merging Account for the Size Growth of Quiescent Galaxies? New Results from the CANDELS Survey. ApJ, 746:162, February 2012. doi: 10.1088/0004-637X/746/2/162.

A. B. Newman, S. Belli, and R. S. Ellis. Discovery of a Strongly Lensed Massive Quiescent Galaxy at z = 2.636: Spatially Resolved Spectroscopy and Indications of Rotation. ApJ, 813: L7, November 2015. doi: 10.1088/2041-8205/813/1/L7.

M. Noguchi. Clumpy star-forming regions as the origin of the peculiar morphology of high-redshift galaxies. Nature, 392:253, March 1998. doi: 10.1038/32596.

J. B. Oke and J. E. Gunn. Secondary standard stars for absolute spectrophotometry. ApJ, 266: 713–717, March 1983. doi: 10.1086/160817.

M. Onodera, A. Renzini, M. Carollo, M. Cappellari, C. Mancini, V. Strazzullo, E. Daddi, N. Arimoto, R. Gobat, Y. Yamada, H. J. McCracken, O. Ilbert, P. Capak, A. Cimatti, M. Giavalisco, A. M. Koekemoer, X. Kong, S. Lilly, K. Motohara, K. Ohta, D. B. Sanders, N. Scoville, N. Tamura, and Y. Taniguchi. Deep Near-infrared Spectroscopy of Passively Evolving Galaxies at z ˜ 1.4. ApJ, 755:26, August 2012. doi: 10.1088/0004-637X/755/1/26.

L. Oser, J. P. Ostriker, T. Naab, P. H. Johansson, and A. Burkert. The Two Phases of Galaxy Formation. ApJ, 725:2312–2323, December 2010. doi: 10.1088/0004-637X/725/2/2312.

L. Oser, T. Naab, J. P. Ostriker, and P. H. Johansson. The Cosmological Size and Velocity Dispersion Evolution of Massive Early-type Galaxies. ApJ, 744:63, January 2012. doi: 10.1088/0004-637X/744/1/63.

S. G. Patel, P. G. van Dokkum, M. Franx, R. F. Quadri, A. Muzzin, D. Marchesini, R. J. Williams, B. P. Holden, and M. Stefanon. HST/WFC3 Confirmation of the Inside-out Growth of Massive Galaxies at 0 z 2 and Identification of Their Star-forming Progenitors at z ˜ 3. ApJ, 766:15, March 2013. doi: 10.1088/0004-637X/766/1/15.

S. G. Patel, Y. X. Hong, R. F. Quadri, B. P. Holden, and R. J. Williams. A comparison of the most massive quiescent galaxies from $z \sim 3$ to the present: slow evolution in size, and spheroid-dominated. ArXiv e-prints, April 2017.

C. Y. Peng, L. C. Ho, C. D. Impey, and H.-W. Rix. Detailed Structural Decomposition of Galaxy Images. AJ, 124:266–293, July 2002. doi: 10.1086/340952.

Y.-j. Peng, S. J. Lilly, K. Kovač, M. Bolzonella, L. Pozzetti, A. Renzini, G. Zamorani, O. Ilbert, C. Knobel, A. Iovino, C. Maier, O. Cucciati, L. Tasca, C. M. Carollo, J. Silverman, P. Kampczyk, L. de Ravel, D. Sanders, N. Scoville, T. Contini, V. Mainieri, M. Scodeggio, J.-P. Kneib, O. Le Fèvre, S. Bardelli, A. Bongiorno, K. Caputi, G. Coppa, S. de la Torre, P. Franzetti, B. Garilli, F. Lamareille, J.-F. Le Borgne, V. Le Brun, M. Mignoli, E. Perez Montero, R. Pello, E. Ricciardelli, M. Tanaka, L. Tresse, D. Vergani, N. Welikala, E. Zucca, P. Oesch, U. Abbas, L. Barnes, R. Bordoloi, D. Bottini, A. Cappi, P. Cassata, A. Cimatti, M. Fumana, G. Hasinger, A. Koekemoer, A. Leauthaud, D. Maccagni, C. Marinoni, H. McCracken, P. Memeo, B. Meneux, P. Nair, C. Porciani, V. Presotto, and R. Scaramella. Mass and Environment as Drivers of Galaxy Evolution in SDSS and zCOSMOS and the Origin of the Schechter Function. ApJ, 721:193–221, September 2010. doi: 10.1088/0004-637X/721/1/193.

B. M. Poggianti, R. Calvi, D. Bindoni, M. D'Onofrio, A. Moretti, T. Valentinuzzi, G. Fasano, J. Fritz, G. De Lucia, B. Vulcani, D. Bettoni, M. Gullieuszik, and A. Omizzolo. Superdense Galaxies and the Mass-Size Relation at Low Redshift. ApJ, 762:77, January 2013. doi: 10.1088/0004-637X/762/2/77.

S. Ravindranath, M. Giavalisco, H. C. Ferguson, C. Conselice, N. Katz, M. Weinberg, J. Lotz, M. Dickinson, S. M. Fall, B. Mobasher, and C. Papovich. The Morphological Diversities among Star-forming Galaxies at High Redshifts in the Great Observatories Origins Deep Survey. ApJ, 652:963–980, December 2006. doi: 10.1086/507016.

A. Rest, F. C. van den Bosch, W. Jaffe, H. Tran, Z. Tsvetanov, H. C. Ford, J. Davies, and J. Schafer. WFPC2 Images of the Central Regions of Early-Type Galaxies. I. The Data. AJ, 121:2431–2482, May 2001. doi: 10.1086/320370.

E. E. Salpeter. The Luminosity Function and Stellar Evolution. ApJ, 121:161, January 1955. doi: 10.1086/145971.

J. A. Sellwood and J. J. Binney. Radial mixing in galactic discs. MNRAS, 336:785–796, November 2002. doi: 10.1046/j.1365-8711.2002.05806.x.

J. L. Sersic. Atlas de galaxias australes. 1968.

S. Shen, H. J. Mo, S. D. M. White, M. R. Blanton, G. Kauffmann, W. Voges, J. Brinkmann, and I. Csabai. The size distribution of galaxies in the Sloan Digital Sky Survey. MNRAS, 343: 978–994, August 2003. doi: 10.1046/j.1365-8711.2003.06740.x.

J. M. Simpson, I. Smail, W.-H. Wang, D. Riechers, J. S. Dunlop, Y. Ao, N. Bourne, A. Bunker, S. C. Chapman, C.-C. Chen, H. Dannerbauer, J. E. Geach, T. Goto, C. M. Harrison, H. S. Hwang, R. J. Ivison, T. Kodama, C.-H. Lee, H.-M. Lee, M. Lee, C.-F. Lim, M. J. Michalowski, D. J. Rosario, H. Shim, X. W. Shu, A. M. Swinbank, W.-L. Tee, Y. Toba, E. Valiante, J. Wang, and X. Z. Zheng. An imperfectly passive nature: Bright sub-millimeter emission from dust-obscured star formation in the z=3.717 "passive" system, ZF20115. ArXiv e-prints, April 2017.

R. E. Skelton, K. E. Whitaker, I. G. Momcheva, G. B. Brammer, P. G. van Dokkum, I. Labbé, M. Franx, A. van der Wel, R. Bezanson, E. Da Cunha, M. Fumagalli, N. Förster Schreiber, M. Kriek, J. Leja, B. F. Lundgren, D. Magee, D. Marchesini, M. V. Maseda, E. J. Nelson, P. Oesch, C. Pacifici, S. G. Patel, S. Price, H.-W. Rix, T. Tal, D. A. Wake, and S. Wuyts. 3D-HST WFC3-selected Photometric Catalogs in the Five CANDELS/3D-HST Fields: Photometry, Photometric Redshifts, and Stellar Masses. ApJS, 214:24, October 2014. doi: 10.1088/0067-0049/214/2/24.

A. Sonnenfeld, C. Nipoti, and T. Treu. Purely Dry Mergers do not Explain the Observed Evolution of Massive Early-type Galaxies since z ˜ 1. ApJ, 786:89, May 2014. doi: 10.1088/0004-637X/786/2/89.

J. S. Speagle, C. L. Steinhardt, P. L. Capak, and J. D. Silverman. A Highly Consistent Framework for the Evolution of the Star-Forming "Main Sequence" from z ˜ 0-6. ApJS, 214:15, October 2014. doi: 10.1088/0067-0049/214/2/15.

D. Spergel, N. Gehrels, C. Baltay, D. Bennett, J. Breckinridge, M. Donahue, A. Dressler, B. S. Gaudi, T. Greene, O. Guyon, C. Hirata, J. Kalirai, N. J. Kasdin, B. Macintosh, W. Moos, S. Perlmutter, M. Postman, B. Rauscher, J. Rhodes, Y. Wang, D. Weinberg, D. Benford, M. Hudson, W.-S. Jeong, Y. Mellier, W. Traub, T. Yamada, P. Capak, J. Colbert, D. Masters, M. Penny, D. Savransky, D. Stern, N. Zimmerman, R. Barry, L. Bartusek, K. Carpenter, E. Cheng, D. Content, F. Dekens, R. Demers, K. Grady, C. Jackson, G. Kuan, J. Kruk, M. Melton, B. Nemati, B. Parvin, I. Poberezhskiy, C. Peddie, J. Ruffa, J. K. Wallace, A. Whipple, E. Wollack, and F. Zhao. Wide-Field InfrarRed Survey Telescope-Astrophysics Focused Telescope Assets WFIRST-AFTA 2015 Report. ArXiv e-prints, March 2015.

I. Strateva, Ž. Ivezić, G. R. Knapp, V. K. Narayanan, M. A. Strauss, J. E. Gunn, R. H. Lupton, D. Schlegel, N. A. Bahcall, J. Brinkmann, R. J. Brunner, T. Budavári, I. Csabai, F. J. Castander, M. Doi, M. Fukugita, Z. Győry, M. Hamabe, G. Hennessy, T. Ichikawa, P. Z. Kunszt, D. Q. Lamb, T. A. McKay, S. Okamura, J. Racusin, M. Sekiguchi, D. P. Schneider, K. Shimasaku, and D. York. Color Separation of Galaxy Types in the Sloan Digital Sky Survey Imaging Data. AJ, 122:1861–1874, October 2001. doi: 10.1086/323301.

R. Suzuki, C. Tokoku, T. Ichikawa, Y. K. Uchimoto, M. Konishi, T. Yoshikawa, I. Tanaka, T. Yamada, K. Omata, and T. Nishimura. Multi-Object Infrared Camera and Spectrograph (MOIRCS) for the Subaru Telescope I. Imaging. PASJ, 60:1347–, December 2008.

D. Szomoru, M. Franx, P. G. van Dokkum, M. Trenti, G. D. Illingworth, I. Labbé, R. J. Bouwens, P. A. Oesch, and C. M. Carollo. Confirmation of the Compactness of a z = 1.91 Quiescent Galaxy with Hubble Space Telescope's Wide Field Camera 3. ApJ, 714:L244–L248, May 2010. doi: 10.1088/2041-8205/714/2/L244.

D. Szomoru, M. Franx, and P. G. van Dokkum. Sizes and Surface Brightness Profiles of Quiescent Galaxies at z ˜ 2. ApJ, 749:121, April 2012. doi: 10.1088/0004-637X/749/2/121.

D. Szomoru, M. Franx, P. G. van Dokkum, M. Trenti, G. D. Illingworth, I. Labbé, and P. Oesch. The Stellar Mass Structure of Massive Galaxies from z = 0 to z = 2.5: Surface Density Profiles and Half-mass Radii. ApJ, 763:73, February 2013. doi: 10.1088/0004-637X/763/2/73.

S. Tacchella, C. M. Carollo, A. Renzini, N. M. F. Schreiber, P. Lang, S. Wuyts, G. Cresci, A. Dekel, R. Genzel, S. J. Lilly, C. Mancini, S. Newman, M. Onodera, A. Shapley, L. Tacconi, J. Woo, and G. Zamorani. Evidence for mature bulges and an inside-out quenching phase 3 billion years after the Big Bang. Science, 348:314–317, April 2015. doi: 10.1126/science.1261094.

L. J. Tacconi, R. Neri, R. Genzel, F. Combes, A. Bolatto, M. C. Cooper, S. Wuyts, F. Bournaud, A. Burkert, J. Comerford, P. Cox, M. Davis, N. M. Förster Schreiber, S. García-Burillo, J. Gracia-Carpio, D. Lutz, T. Naab, S. Newman, A. Omont, A. Saintonge, K. Shapiro Griffin, A. Shapley, A. Sternberg, and B. Weiner. Phibss: Molecular Gas Content and Scaling Relations in z ˜ 1-3 Massive, Main-sequence Star-forming Galaxies. ApJ, 768:74, May 2013. doi: 10.1088/0004-637X/768/1/74.

K.-i. Tadaki, T. Kodama, I. Tanaka, M. Hayashi, Y. Koyama, and R. Shimakawa. The Nature of Hα-selected Galaxies at z 2. II. Clumpy Galaxies and Compact Star-forming Galaxies. ApJ, 780:77, January 2014. doi: 10.1088/0004-637X/780/1/77.

K.-i. Tadaki, R. Genzel, T. Kodama, S. Wuyts, E. Wisnioski, N. M. Förster Schreiber, A. Burkert, P. Lang, L. J. Tacconi, D. Lutz, S. Belli, R. I. Davies, B. Hatsukade, M. Hayashi, R. Herrera-Camus, S. Ikarashi, S. Inoue, K. Kohno, Y. Koyama, J. T. Mendel, K. Nakanishi, R. Shimakawa, T. L. Suzuki, Y. Tamura, I. Tanaka, H. Übler, and D. J. Wilman. Bulge-forming Galaxies with an Extended Rotating Disk at z ˜ 2. ApJ, 834:135, January 2017. doi: 10.3847/1538-4357/834/2/135.

T. Tal, A. Dekel, P. Oesch, A. Muzzin, G. B. Brammer, P. G. van Dokkum, M. Franx, G. D. Illingworth, J. Leja, D. Magee, D. Marchesini, I. Momcheva, E. J. Nelson, S. G. Patel, R. F. Quadri, H.-W. Rix, R. E. Skelton, D. A. Wake, and K. E. Whitaker. Observations of Environmental Quenching in Groups in the 11GYR since z = 2.5: Different Quenching for Central and Satellite Galaxies. ApJ, 789:164, July 2014. doi: 10.1088/0004-637X/789/2/164.

N. Tamura and K. Ohta. Color Gradients in Early-Type Galaxies in Abell 2199. AJ, 126:596–631, August 2003. doi: 10.1086/376469.

N. Tamura and K. Ohta. Radial variation of optical and near-infrared colours in luminous early-type galaxies in A2199. MNRAS, 355:617–626, December 2004. doi: 10.1111/j.1365-2966.2004.08350.x.

N. Tamura, C. Kobayashi, N. Arimoto, T. Kodama, and K. Ohta. Origin of Color Gradients in Elliptical Galaxies. AJ, 119:2134–2145, May 2000. doi: 10.1086/301333.

T. Tapia, M. C. Eliche-Moral, M. Querejeta, M. Balcells, A. César González-García, M. Prieto, J. A. L. Aguerri, J. Gallego, J. Zamorano, C. Rodríguez-Pérez, and A. Borlaff. Evolution induced by dry minor mergers onto fast-rotator S0 galaxies. A&A, 565:A31, May 2014. doi: 10.1051/0004-6361/201321386.

E. N. Taylor, M. Franx, J. Brinchmann, A. van der Wel, and P. G. van Dokkum. On the Masses of Galaxies in the Local Universe. ApJ, 722:1–19, October 2010. doi: 10.1088/0004-637X/722/1/1.

H. I. Teplitz, M. Rafelski, P. Kurczynski, N. A. Bond, N. Grogin, A. M. Koekemoer, H. Atek, T. M. Brown, D. Coe, J. W. Colbert, H. C. Ferguson, S. L. Finkelstein, J. P. Gardner, E. Gawiser, M. Giavalisco, C. Gronwall, D. J. Hanish, K.-S. Lee, D. F. de Mello, S. Ravindranath, R. E. Ryan, B. D. Siana, C. Scarlata, E. Soto, E. N. Voyer, and A. M. Wolfe. UVUDF: Ultraviolet Imaging of the Hubble Ultra Deep Field with Wide-Field Camera 3. AJ, 146:159, December 2013. doi: 10.1088/0004-6256/146/6/159.

D. Thomas, C. Maraston, R. Bender, and C. Mendes de Oliveira. The Epochs of Early-Type Galaxy Formation as a Function of Environment. ApJ, 621:673–694, March 2005. doi: 10.1086/426932.

S. Toft, V. Smolčić, B. Magnelli, A. Karim, A. Zirm, M. Michalowski, P. Capak, K. Sheth, K. Schawinski, J.-K. Krogager, S. Wuyts, D. Sanders, A. W. S. Man, D. Lutz, J. Staguhn, S. Berta, H. Mccracken, J. Krpan, and D. Riechers. Submillimeter Galaxies as Progenitors of Compact Quiescent Galaxies. ApJ, 782:68, February 2014. doi: 10.1088/0004-637X/782/2/68.

R. Tojeiro and W. J. Percival. The evolution of luminous red galaxies in the Sloan Digital Sky Survey 7th data release. MNRAS, 405:2534–2548, July 2010. doi: 10.1111/j.1365-2966.2010.16630.x.

A. Toomre. Mergers and Some Consequences. In B. M. Tinsley and R. B. G. Larson, D. Campbell, editors, Evolution of Galaxies and Stellar Populations, page 401, 1977.

C. A. Tremonti, T. M. Heckman, G. Kauffmann, J. Brinchmann, S. Charlot, S. D. M. White, M. Seibert, E. W. Peng, D. J. Schlegel, A. Uomoto, M. Fukugita, and J. Brinkmann. The Origin of the Mass-Metallicity Relation: Insights from 53,000 Star-forming Galaxies in the Sloan Digital Sky Survey. ApJ, 613:898–913, October 2004. doi: 10.1086/423264.

T. Treu, R. S. Ellis, J.-P. Kneib, A. Dressler, I. Smail, O. Czoske, A. Oemler, and P. Natarajan. A Wide-Field Hubble Space Telescope Study of the Cluster Cl 0024+16 at z = 0.4. I. Morphological Distributions to 5 Mpc Radius. ApJ, 591:53–78, July 2003. doi: 10.1086/375314.

T. Treu, R. S. Ellis, T. X. Liao, P. G. van Dokkum, P. Tozzi, A. Coil, J. Newman, M. C. Cooper, and M. Davis. The Assembly History of Field Spheroidals: Evolution of Mass-to-Light Ratios and Signatures of Recent Star Formation. ApJ, 633:174–197, November 2005. doi: 10.1086/444585.

T. Treu, M. W. Auger, L. V. E. Koopmans, R. Gavazzi, P. J. Marshall, and A. S. Bolton. The Initial Mass Function of Early-Type Galaxies. ApJ, 709:1195–1202, February 2010. doi: 10.1088/0004-637X/709/2/1195.

I. Trujillo, C. J. Conselice, K. Bundy, M. C. Cooper, P. Eisenhardt, and R. S. Ellis. Strong size evolution of the most massive galaxies since z ˜ 2. MNRAS, 382:109–120, November 2007. doi: 10.1111/j.1365-2966.2007.12388.x.

I. Trujillo, A. Ferré-Mateu, M. Balcells, A. Vazdekis, and P. Sánchez-Blázquez. NGC 1277: A Massive Compact Relic Galaxy in the Nearby Universe. ApJ, 780:L20, January 2014. doi: 10.1088/2041-8205/780/2/L20.

T. Valentinuzzi, J. Fritz, B. M. Poggianti, A. Cava, D. Bettoni, G. Fasano, M. D'Onofrio, W. J. Couch, A. Dressler, M. Moles, A. Moretti, A. Omizzolo, P. Kjærgaard, E. Vanzella, and J. Varela. Superdense Massive Galaxies in Wings Local Clusters. ApJ, 712:226–237, March 2010. doi: 10.1088/0004-637X/712/1/226.

J. van de Sande, M. Kriek, M. Franx, P. G. van Dokkum, R. Bezanson, R. J. Bouwens, R. F. Quadri, H.-W. Rix, and R. E. Skelton. Stellar Kinematics of z ˜ 2 Galaxies and the Inside-out Growth of Quiescent Galaxies. ApJ, 771:85, July 2013. doi: 10.1088/0004-637X/771/2/85.

F. C. van den Bosch, G. F. Lewis, G. Lake, and J. Stadel. Substructure in Dark Halos: Orbital Eccentricities and Dynamical Friction. ApJ, 515:50–68, April 1999. doi: 10.1086/307023.

A. van der Wel, E. F. Bell, B. P. Holden, R. A. Skibba, and H.-W. Rix. The Physical Origins of the Morphology-Density Relation: Evidence for Gas Stripping from the Sloan Digital Sky Survey. ApJ, 714:1779–1788, May 2010. doi: 10.1088/0004-637X/714/2/1779.

A. van der Wel, E. F. Bell, B. Häussler, E. J. McGrath, Y.-Y. Chang, Y. Guo, D. H. McIntosh, H.-W. Rix, M. Barden, E. Cheung, S. M. Faber, H. C. Ferguson, A. Galametz, N. A. Grogin, W. Hartley, J. S. Kartaltepe, D. D. Kocevski, A. M. Koekemoer, J. Lotz, M. Mozena, M. A. Peth, and C. Y. Peng. Structural Parameters of Galaxies in CANDELS. ApJS, 203:24, December 2012. doi: 10.1088/0067-0049/203/2/24.

A. van der Wel, M. Franx, P. G. van Dokkum, R. E. Skelton, I. G. Momcheva, K. E. Whitaker, G. B. Brammer, E. F. Bell, H.-W. Rix, S. Wuyts, H. C. Ferguson, B. P. Holden, G. Barro, A. M. Koekemoer, Y.-Y. Chang, E. J. McGrath, B. Häussler, A. Dekel, P. Behroozi, M. Fumagalli, J. Leja, B. F. Lundgren, M. V. Maseda, E. J. Nelson, D. A. Wake, S. G. Patel, I. Labbé, S. M. Faber, N. A. Grogin, and D. D. Kocevski. 3D-HST+CANDELS: The Evolution of the Galaxy Size-Mass Distribution since z = 3. ApJ, 788:28, June 2014. doi: 10.1088/0004-637X/788/1/28.

P. van Dokkum, G. Brammer, I. Momcheva, R. E. Skelton, K. E. Whitaker, and for the 3D-HST team. 3D-HST Data Release v3.0: Extremely Deep Spectra in the UDF and WFC3 Mosaics in the 3D-HST/CANDELS Fields. ArXiv e-prints, May 2013a.

P. G. van Dokkum and M. Franx. The Fundamental Plane in CL 0024 at z = 0.4: implications for the evolution of the mass-to-light ratio. MNRAS, 281:985–1000, August 1996. doi: 10.1093/mnras/281.3.985.

P. G. van Dokkum, M. Franx, M. Kriek, B. Holden, G. D. Illingworth, D. Magee, R. Bouwens, D. Marchesini, R. Quadri, G. Rudnick, E. N. Taylor, and S. Toft. Confirmation of the Remarkable Compactness of Massive Quiescent Galaxies at z ˜ 2.3: Early-Type Galaxies Did not Form in a Simple Monolithic Collapse. ApJ, 677:L5–L8, April 2008. doi: 10.1086/587874.

P. G. van Dokkum, M. Kriek, and M. Franx. A high stellar velocity dispersion for a compact massive galaxy at redshift z = 2.186. Nature, 460:717–719, August 2009. doi: 10.1038/nature08220.

P. G. van Dokkum, K. E. Whitaker, G. Brammer, M. Franx, M. Kriek, I. Labbé, D. Marchesini, R. Quadri, R. Bezanson, G. D. Illingworth, A. Muzzin, G. Rudnick, T. Tal, and D. Wake. The Growth of Massive Galaxies Since z = 2. ApJ, 709:1018–1041, February 2010. doi: 10.1088/0004-637X/709/2/1018.

P. G. van Dokkum, J. Leja, E. J. Nelson, S. Patel, R. E. Skelton, I. Momcheva, G. Brammer, K. E. Whitaker, B. Lundgren, M. Fumagalli, C. Conroy, N. Förster Schreiber, M. Franx, M. Kriek, I. Labbé, D. Marchesini, H.-W. Rix, A. van der Wel, and S. Wuyts. The Assembly of Milky-Way-like Galaxies Since z ˜ 2.5. ApJ, 771:L35, July 2013b. doi: 10.1088/2041-8205/771/2/L35.

P. G. van Dokkum, E. J. Nelson, M. Franx, P. Oesch, I. Momcheva, G. Brammer, N. M. Förster Schreiber, R. E. Skelton, K. E. Whitaker, A. van der Wel, R. Bezanson, M. Fumagalli, G. D. Illingworth, M. Kriek, J. Leja, and S. Wuyts. Forming Compact Massive Galaxies. ApJ, 813:23, November 2015. doi: 10.1088/0004-637X/813/1/23.

M. B. Vila-Costas and M. G. Edmunds. The relation between abundance gradients and the physical properties of spiral galaxies. MNRAS, 259:121–145, November 1992.

S. Wellons, P. Torrey, C.-P. Ma, V. Rodriguez-Gomez, A. Pillepich, D. Nelson, S. Genel, M. Vogelsberger, and L. Hernquist. The diverse evolutionary paths of simulated high-z massive, compact galaxies to z = 0. MNRAS, 456:1030–1048, February 2016. doi: 10.1093/mnras/stv2738.

A. R. Wetzel, J. L. Tinker, C. Conroy, and F. C. van den Bosch. Galaxy evolution in groups and clusters: satellite star formation histories and quenching time-scales in a hierarchical Universe. MNRAS, 432:336–358, June 2013. doi: 10.1093/mnras/stt469.

K. E. Whitaker, P. G. van Dokkum, G. Brammer, and M. Franx. The Star Formation Mass Sequence Out to z = 2.5. ApJ, 754:L29, August 2012. doi: 10.1088/2041-8205/754/2/L29.

K. E. Whitaker, M. Franx, J. Leja, P. G. van Dokkum, A. Henry, R. E. Skelton, M. Fumagalli, I. G. Momcheva, G. B. Brammer, I. Labbé, E. J. Nelson, and J. R. Rigby. Constraining the Low-mass Slope of the Star Formation Sequence at 0.5 z 2.5. ApJ, 795:104, November 2014. doi: 10.1088/0004-637X/795/2/104.

K. E. Whitaker, R. Bezanson, P. G. van Dokkum, M. Franx, A. van der Wel, G. Brammer, N. M. Forster-Schreiber, M. Giavalisco, I. Labbe, I. G. Momcheva, E. J. Nelson, and R. Skelton. Predicting Quiescence: The Dependence of Specific Star Formation Rate on Galaxy Size and Central Density at 0.5z2.5. ArXiv e-prints, July 2016.

R. J. Williams, R. F. Quadri, M. Franx, P. van Dokkum, and I. Labbé. Detection of Quiescent Galaxies in a Bicolor Sequence from Z = 0-2. ApJ, 691:1879–1895, February 2009. doi: 10.1088/0004-637X/691/2/1879.

J. Woo, A. Dekel, S. M. Faber, and D. C. Koo. Two Conditions for Galaxy Quenching: Compact Centres and Massive Haloes. ArXiv e-prints, June 2014.

S. Wuyts, T. J. Cox, C. C. Hayward, M. Franx, L. Hernquist, P. F. Hopkins, P. Jonsson, and P. G. van Dokkum. On Sizes, Kinematics, M/L Gradients, and Light Profiles of Massive Compact Galaxies at z ˜ 2. ApJ, 722:1666–1684, October 2010. doi: 10.1088/0004-637X/722/2/1666.

S. Wuyts, N. M. Förster Schreiber, D. Lutz, R. Nordon, S. Berta, B. Altieri, P. Andreani, H. Aussel, A. Bongiovanni, J. Cepa, A. Cimatti, E. Daddi, D. Elbaz, R. Genzel, A. M. Koekemoer, B. Magnelli, R. Maiolino, E. J. McGrath, A. Pérez García, A. Poglitsch, P. Popesso, F. Pozzi, M. Sanchez-Portal, E. Sturm, L. Tacconi, and I. Valtchanov. On Star Formation Rates and Star Formation Histories of Galaxies Out to z ˜ 3. ApJ, 738:106, September 2011. doi: 10.1088/0004-637X/738/1/106.

S. Wuyts, N. M. Förster Schreiber, R. Genzel, Y. Guo, G. Barro, E. F. Bell, A. Dekel, S. M. Faber, H. C. Ferguson, M. Giavalisco, N. A. Grogin, N. P. Hathi, K.-H. Huang, D. D. Kocevski, A. M. Koekemoer, D. C. Koo, J. Lotz, D. Lutz, E. McGrath, J. A. Newman, D. Rosario, A. Saintonge, L. J. Tacconi, B. J. Weiner, and A. van der Wel. Smooth(er) Stellar Mass Maps in CANDELS: Constraints on the Longevity of Clumps in High-redshift Star-forming Galaxies. ApJ, 753:114, July 2012. doi: 10.1088/0004-637X/753/2/114.